



UNIVERSITÀ DEGLI STUDI DI MILANO

Scuola di Dottorato in Fisica, Astrofisica e Fisica Applicata
Dipartimento di Fisica

Corso di Dottorato in Fisica, Astrofisica e Fisica Applicata
Ciclo XXXIV

**Higgs boson production at the Large Hadron Collider:
accurate theoretical predictions at higher orders in QCD**

Settore Scientifico Disciplinare FIS/02

Supervisore: Prof. Giancarlo Ferrera

Coordinatore: Prof. Matteo Paris

Tesi di Dottorato di: Dr. Jesús Urtasun Elizari

Anno Accademico 2021-2022

Commission of external referees:

External Referee:

Dott. German Sborlini

External Referee:

Dott. Gennaro Corcella

Commission of the final examination:

President:

Prof. Carlo Oleari

1st commissioner:

Prof. Alessandro Bacchetta

2nd commissioner:

Prof. Giancarlo Ferrera

Final examination:

Friday 25th, February 2022

Università degli Studi di Milano, Dipartimento di Fisica, Milano, Italy

Cover illustration:

...

Internal illustrations:

...

Design:

...

MIUR subjects:

FIS/02

Theoretical Physics

To my parents

Contents

Introduction	vi
Part I : Quantum Chromodynamics	1
1 Quantum Chromodynamics	3
1.1 The colour quantum number	4
1.2 The Lagrangian of QCD	5
1.3 The strong coupling	9
2 Hadronic processes and factorization	15
2.1 Parton Model and factorization	15
2.2 Parton densities	18
2.3 Fixed-Order QCD	20
2.4 Exclusive final states - the subtraction idea	25
2.5 IR safety	26
3 Phenomenology at the LHC	29
3.1 Deep Inelastic Scattering	32
3.2 The Drell-Yan process	35
3.3 SM Higgs boson production	38
Part II : Transverse momentum resummation	42
4 Transverse momentum resummation	45
4.1 The resummation formalism	46
4.2 The resummed component	49
4.3 The finite component	53
5 The resummed Higgs q_T distribution	59

Part III : HTurbo numerical implementation	63
6 HTurbo numerical implementation	67
6.1 Introduction	67
6.2 Predictions with HTurbo	69
6.3 Tests of numerical precision	82
6.4 HTurbo N ³ LL implementation	89
Conclusions	91
List of Publications	95
Appendices	95
A Integral transformations	99
A.1 Fourier-Bessel transformation	99
A.2 Laplace transformation	100
A.3 Mellin transformation	101
B Special functions	103
B.1 Euler Gamma and related functions	103
B.2 Riemann zeta function	105
B.3 Bessel function	106
B.4 Plus distribution	107
C HTurbo architecture and usage	109
C.1 The structure of HTurbo	109
C.2 Benchmark results	111
List of Figures	113
Bibliography	119
Acknowledgments	128

Motivation

As wonderfully phrased by Feynman in his famous essay *The Value of Science* back in 1955, “*the same drill, the same mystery, comes again and again when we look at any problem deeply enough. With more knowledge comes deeper, more wonderful the mystery, luring one to penetrate deeper still*”. Indeed, the attempt of modeling nature and the physical laws that seem to describe it, often raises questions of deep complexity. For the last decades, those questions have headed the limits of direct observation and produced such complex formalisms when aiming to describe the atomic and nuclear phenomena. Heading now towards the precision era of the Large Hadron Collider (LHC) at CERN, and involved in an unprecedented computational revolution, the description of nature at its fundamental scales and the predictions built have reached an accuracy that exceeds even the most optimistic aspirations. But there is, though, and phrasing Feynman again, plenty of room at the bottom...

The main goal of theoretical high energy physics could just be phrased as trying to accurately describe what are often referred to as the *fundamental interactions*. In words of Guido Altarelli, an attempt to reduce all natural phenomena to a set of basic rules and laws which, at least in principle, can quantitatively reproduce and predict experimental observations. It is important to remind the reader, regardless of its previous experience with the physical sciences, that beyond the microscopic level, all the phenomenology of matter and radiation, including molecular, atomic, nuclear and sub-nuclear phenomena, can be understood and accurately described in terms of three classes of fundamental interactions: the so-called electromagnetic, strong, and weak interactions. A fourth interaction, the gravitational one, plays a dominant role when addressing much more macroscopic scales, from all material bodies on earth to the vast astrophysical and cosmic objects, while remaining negligible in atomic and nuclear physics.

All these interactions, with the current exception of gravity, are described within the framework of quantum mechanics and special relativity, or more precisely, by a set or relativistic Quantum Field Theories (QFTs). By quantum *field* theory, we mean that fundamental objects of nature will not be understood as point-like, following the classical intuition that small objects are localized in a well defined position. They will, instead, be described by homogeneous fields with quantum mechanical behavior, in such a way that particles are understood as localized excitations of the field. For a more detailed description of this formalism see [1]. Our current understanding of nature at the most fundamental scales, aiming to describe physical phenomena at the TeV scale - meaning length

scales of order $\lesssim 10^{-20}$ m - is summarized in a set of Quantum Field Theories known as the Standard Model of particle physics [2]. Those fields belong to different classes of matter such as fermions, composing matter itself, gauge bosons acting as the mediators of the interactions, and a scalar Higgs boson, responsible for the process through which all particles acquire mass. Without going into much detail, those different species of matter will be described by quantum fields fulfilling different representations of the Lorentz group, generating the vast amount of phenomenology encountered in nature from a very fundamental set of rules.

This thesis is devoted to Quantum Chromodynamics (QCD) [3], the sector of the Standard Model describing the strong interactions, meaning the interactions between quarks and gluons. A full chapter of this thesis is devoted to a proper introduction on QCD and its basic components. Finally heading towards the precision era of the LHC, as already mentioned, building fast and accurate predictions at the TeV scale and beyond has become the main task for theoreticians. Indeed, being the LHC a hadron collider, all the interesting reactions originate from a hadronic scattering, mediated by the strong interactions and described by QCD. LHC and related experiments finally started in 2010, being one of its original goals the detection of the Higgs boson, already predicted by Higgs and Englert [4, 5, 6], among others, back in the mid 1960s. The first collision at center-of-mass energy of 7 TeV took place in March of 2010, exceeding the previous world record set by the US Fermi National Accelerator Laboratory's Tevatron collider in 2010, and setting the beginning of a new era for particle physics, which marked an important milestone in LHC commissioning. A second milestone, and such a famous one, was the detection of a resonance compatible with the Higgs boson predicted by the Standard Model [7, 8].

Along the LHC ring, we find four main experiments worth mentioning: ATLAS (A Toroidal LHC Apparatus), CMS (Compact Muon Solenoid), ALICE (A Large Ion Collider Experiment) and LHCb (LHC beauty). The last two are devoted to the study of high-density hadron matter, such as quark-gluon plasma, and the so-called *flavour* physics through the study of b-hadrons and the phenomenon of CP-violation, respectively. ATLAS and CMS, conversely, are general purpose experiments, and their main goals were originally searching for the Higgs boson - at that time, the last missing particle to make the Standard Model consistent - and for any kind of signals of new physics beyond the Standard Model (Supersymmetry (SUSY), extra-dimensions, dark matter signatures, ...). To be able to see such hints of new physics beyond the Standard Model, it is crucial to have very accurate theoretical predictions of what is expected by the Standard Model, at least as accurate as precise the detection and measurement techniques, in order to be able to distinguish deviation from the expectations with the maximal significance.

Our current understanding of particle physics depends crucially on the breaking of the electroweak symmetry (EWSB) to give mass to the W and Z bosons, as well as to all fermions composing matter. As we just mentioned, the Standard Model involves in its description a neutral scalar, the Higgs boson, whose dominant production mechanism at the LHC is the gluon-gluon fusion process. Through parts I and II of this manuscript we will go through the basics of QCD, perturbation theory and some of the most important process addressed in collider experiments, such as Deep Inelastic Scattering (DIS), the Drell-Yan lepton pair production, and the Higgs boson production.

The observable quantities that are measured in LHC and related experiments are mainly *cross sections*, both total (inclusive) and differential (exclusive) in the various kinematic variables. Cross-sections in particle physics processes are typically computed

using perturbation theory, which provides a very powerful set of tools to predict observable quantities from a Quantum Field Theory. It is based on the assumption that a given observable can be defined by a power series in the coupling constant of the theory: then, if such coupling is small enough to be considered a *perturbative* parameter, the computation of the first few orders of the power series is sufficiently accurate to describe the observable. However, this assumption needs some care, since perturbative series can indeed be divergent. It is possible to interpret the perturbative expansion in the sense of an asymptotic series, where the inclusion of higher orders improves the estimate of the physical quantity under study, up to some finite order, thereby saving perturbation theory from a dramatic failure. However, there are situations in which the growth of the series already starts at the level of the first terms; in these cases, a truncation of the series is of no meaning and only a *resummed* result is reliable. This is a situation that quite often appears in QCD, and hence one of the main problems addressed in this thesis. A cross-section generically depends on many energy scales, and the dependence is typically in the form of logarithmic ratios of energies. In some kinematical regimes, when two of such scales become very different to each other these logs become large and the coefficients of the perturbative series are significantly enhanced, making the standard perturbative approach unreliable. Then, the entire series of these enhanced terms has to be resummed in order to have an accurate prediction for the observable.

Finally heading to the actual purpose of this thesis, we face here the problem of resummation of perturbation series in QCD. The processes that will be discussed are the production of high invariant mass systems at hadron colliders, such as the Drell-Yan pair production or the Higgs boson production. Since at hadron colliders the initial state particles are hadrons, the cross-sections are typically computed using the Parton Model, which describes the interaction of the hadron via its partons (quarks and gluons): the parton-level cross-section is then computed in QCD using perturbation theory, and the hadronic cross-section is predicted by performing a convolution with the parton distribution functions, which are non-perturbative objects encoding the information about how those partons are distributed inside the hadron. Chapter 2 of this thesis is devoted to the introduction of the Parton Model and the parton densities, and Chapter 4 to the transverse momentum resummation formalism.

The production of colourless particles (Drell-Yan lepton pairs, Higgs boson, etc) are extremely important for Standard Model precision tests and for beyond the Standard Model (BSM) searches at hadron colliders. Fast and accurate predictions are essential to enable the best use of the precision measurements for these processes; they are used for parton density fits, for the extraction of fundamental parameters of the SM, and for the estimation of background processes in various searches. This thesis describes at its end a new numerical program, **HTurbo**, producing fast and accurate predictions for the QCD transverse-momentum resummation of Higgs cross sections up to next-to-next-to-next-to-leading logarithmic (N^3LL) accuracy, combined with the fixed-order results at next-to-next-to-leading order, including the full kinematical dependence of the decaying lepton pair with the corresponding spin correlations and the finite-width effects. The **HTurbo** program is an improved reimplementations of the **HqT**, **HRes** and **HNNLO** programs, which provides fast and numerically precise predictions through the factorization of the cross section into production and decay variables, and the usage of quadrature rules based on interpolating functions, together with the Vegas Monte Carlo algorithm, for the integration over kinematic variables. We show below a brief outline of this thesis, for the reader to have an overall sight of its contents, to be used as a roadmap.

Thesis overview

Outline

The present thesis consists in three parts, with a total of six chapters, followed by an Appendix section and the bibliographic note. Each part is devoted to the study of the internal dynamics of the proton and the computational tools used for its description. Part I describes the basics of Quantum Chromodynamics, the part of the Standard Model addressing the strong interactions. It also briefly presents the main physical processes addressed by the experiments within the LHC, meaning the production of colourless particles such as the Drell-Yan process (via the intermediate production of electroweak bosons Z and W), and the Higgs boson. Part II describes with some detail the resummation formalism, that is, the mathematical framework used to address the logarithmic enhancements that appear in the perturbative series when computing the cross sections. Finally, in Part III we present the implementation of this formalism in the numerical code named **HTurbo**, producing fast and precise predictions for the resummed transverse momentum distribution of the Higgs boson at the LHC.

Introduction

Motivation

Thesis overview

Main results

Part I: Quantum Chromodynamics.

Chapter 1 - Quantum Chromodynamics

Chapter 2 - Hadronic Processes and factorization

Chapter 3 - Phenomenology at the LHC

Part II: Transverse momentum resummation

Chapter 4 - Transverse momentum resummation

Chapter 5 - The resummed Higgs q_T distribution

Part III: **HTurbo** numerical implementation

Chapter 6 - **HTurbo** numerical implementation

Appendices

Appendix A. Integral transformation

Appendix B. Special functions

Appendix C. **HTurbo** architecture and usage

Bibliography

Acknowledgments

Main results

As stated already, the production of fast and accurate predictions has become one of the main tasks among theoreticians, heading towards the high luminosity era of the LHC, and resummation in QCD is needed for the prediction of hadronic observables, and in particular of differential distributions. The **HTurbo** program provides fast and numerically precise predictions for Higgs boson production, through a new implementation of the **HqT**, **HRes** and **HNNLO** numerical codes. The cross-section predictions include the calculation of the QCD transverse-momentum resummation up to next-to-next-to-next-to-leading logarithmic (N^3LL) accuracy, combined with the fixed-order results at next-to-next-to-leading order. They also include the full kinematical dependence of the decaying photon pair. The enhancement in performance over previous programs is achieved by code optimization, by factorizing the cross section into production and decay variables, and with the usage of numerical integration based on interpolating functions. The resulting cross-section predictions are in agreement with the results of the original programs at the per mille level. The great reduction of computing time for performing cross-sections calculation opens new possibilities for Higgs processes at the LHC, and also opens the possibility of searches for physics beyond the Standard Model. A detailed description of the code performance and its results can be found at the very end of this thesis in Chapter 6, while the architecture and usage are discussed in Appendix C.

Part I

Quantum Chromodynamics

The strong interactions

This chapter aims to introduce Quantum Chromodynamics (QCD), the theory of the strong interactions. We would like to draw the reader's attention to this chapter in particular, since the basic concepts about colour quantum number, group representation and renormalization, among others, are the ingredients for the description of more complex phenomena that we will discuss later on throughout this thesis.

QCD is the sector of the so-called Standard Model of particle physics [2, 3], which describes the strong interactions and the phenomenology we encounter at the typical scales addressed by the LHC, which is, the TeV scale ($\lesssim 10^{-20}$ m). In particular, QCD is the theory of the interactions between quarks and gluons, which are the fundamental fields that form the hadronic matter. It is an unbroken gauge theory based on the color group SU(3) [9], where the eight massless gauge bosons are the so-called gluons g , and the matter fields are described by "colour triplet" fermions, named quarks. Therefore quarks and gluons are the only fundamental fields of the Standard Model (SM) feeling the strong interactions, in other words, the only ones that interact strongly. When probed at very short wavelengths, QCD is essentially a theory of weakly interacting "partons"¹ - quarks and gluons - which scatter off one another through relatively small quantum corrections. However, at longer wavelengths, of the order of the size of the proton ($\sim 1\text{fm} = 10^{-15}\text{m}$), or equivalently at energies of order MeV, we see large number of hadronic bound states emerging, with string-like, or *confining* potentials building up as we try to separate their partonic constituents. Given our inability to perform analytic calculations in strongly coupled field theories, QCD is therefore still only partially solved. Nevertheless, all its features across all length scales are believed to be encoded in a single one-line formula of alluring simplicity; the Lagrangian of QCD, which we describe in the sections below.

When describing collider physics, we encounter that some parts of QCD can be calculated in terms of the fundamental parameters of the Lagrangian, whereas others must be expressed through complex models lying on large sets of parameters which are not a priori computable, and which need to be constrained by fitting from data. However, even in the absence of a perturbative expansion, there are still theorems which can be used to give relations between seemingly different processes and that do come to aid. Thus, in the chapters dealing with phenomenological models we shall emphasize that

¹The origin of the term "parton" is due to Richard Feynman, who back in the 1960s realized that at high enough energies any hadron could be described as a composite object made of point-like things that he called "partons". Effectively, when we say partons we are typically referring to quarks and gluons inside the proton.

the loss of a factorized perturbative expansion is not equivalent to a total loss of predictivity, in the sense that QCD remains a perfectly self-consistent theory, whose predictions can be compared with data with large accurate agreement.

Moreover, QCD is one of the richest gauge theories we have so far encountered. Its emergent phenomena, unitarity properties, colour structure, non-perturbative dynamics, interplay between scale-invariant and scale-dependent properties, and its wide range of phenomenological applications, are still topics of active investigation. In addition, or perhaps as a consequence, the field of QCD is currently experiencing fast improvements in various areas. On the perturbative side, new methods to compute scattering amplitudes with very high particle multiplicities are being developed, together with advanced computational techniques for combining such amplitudes with all-orders resummation frameworks. On the non-perturbative side, data on soft-physics processes from the LHC is suggesting to reconsider the reliability of the standard fragmentation models, and heavy-ion collisions are providing new insights into the collective behavior of hadronic matter in QCD, that can be already studied from e^+e^- annihilation. We will now review some basics of QCD, introduce the Parton Model and describe in more details the parton densities and the DGLAP evolution equations. This chapter is by no means intended as a complete review; in particular we assume the reader knows the quantum theory of fields.

We shall focus on QCD for mainstream collider physics. This includes the basics of $SU(3)$, colour factors, the running of α_s , factorization, hard processes, infrared safety, with some notes on parton showers and matching. While not covering everything, hopefully these topics can also serve at least as stepping stones to more specialized issues that have been left out, such as event generators, heavy flavours, polarization, or to topics more tangential to other fields, such as axions, lattice QCD, or heavy-ion physics.

1.1 The colour quantum number

The overwhelming experimental evidence that the nucleons are made of quarks is reviewed in [9]. *Baryons* are bound states of three quarks, and the *mesons* are composed by a quark and an antiquark. An immediate success of the quark model, following the additive rules of angular momentum for building hadronic bound states, is not other than its astonishing simplicity. Protons and neutrons are relatively complicated objects, with a size and a rich internal quark structure. The structureless quarks, as dealt with in Quantum Field Theory, enable to explore other interactions with the same powerful theoretical techniques that were so successful in describing the electromagnetic interactions at the quantum level through Quantum Electrodynamics (QED).

As a chronological note for approaching the strong interactions, let us to consider the story of the discovery the *colour* degree of freedom, or colour quantum number. The first hint for a color quantum number, which was arguably the measurement of the Δ^{++} baryon state, discovered in 1951 [10], is described below. The title and part of the abstract from this historical paper are reproduced in Figure 1.1. In the context of the quark model, which first had to be developed, successively joining together notions of spin, isospin, strangeness, etc, the flavour and spin of the Δ^{++} baryon state is described by

$$|\Delta^{++}\rangle = |u_\uparrow u_\uparrow u_\uparrow\rangle, \quad (1.1)$$

clearly a symmetric configuration of three u quarks with spin "up". This correctly matches the properties of the doubly charged Δ^{++} baryon, however, since is a fermion,

Meson-Nucleon Scattering and Nucleon Isobars*

KEITH A. BRUECKNER
Department of Physics, Indiana University, Bloomington, Indiana
(Received December 17, 1951)

“[...] It is concluded that the apparently anomalous features of the scattering can be interpreted to be an indication of a resonant meson-nucleon interaction corresponding to a nucleon isobar with spin $\frac{3}{2}$, isotopic spin $\frac{3}{2}$, and with an excitation energy of 277 MeV.”

Figure 1.1: Title and part of the abstract of the 1951 paper [10] (published in 1952) in which the existence of the Δ^{++} baryon was deduced, based on data from Sachs and Steinberger at Columbia [11] and from Anderson, Fermi, Nagle et al. at Chicago [12, 13]. See also memoir by Nagle [14].

it must have an overall antisymmetric wave function. That is, the quark scheme forces us to combine three identical fermions u in a completely symmetric ground state uuu in order to accommodate the known properties of the Δ^{++} particle, but such a state is of course forbidden by Fermi statistics. In 1965, fourteen years after its discovery, this was finally understood by the introduction of colour as a new quantum number associated with the SU(3) group [15, 16]. The Δ^{++} wave function can now be made antisymmetric by arranging its three quarks antisymmetrically in this new degree of freedom,

$$|\Delta^{++}\rangle = \varepsilon^{ijk} |u_{i\uparrow}u_{j\uparrow}u_{k\uparrow}\rangle, \quad (1.2)$$

being now the color indices either red, green, or blue, and for antiquarks the complementary antired, antiblue, antigreen, and hence solving the mystery.

Here we encounter quite an immediate problem: if for instance $u_R u_G u_B$ is the Δ^{++} , then we appear to have, following the same reasoning, many candidate states for the proton: $u_R u_G d_B$, $u_R u_G d_G$, $u_R u_G d_R$, and so on. Yet only one proton state exists, and therefore we have to introduce our color quantum number in such a way that it does not affect the number of proton states, since it would drive us to a direct conflict with observation. The way this is done is to assert that all particle states observed in nature are *color singlets*, or *colorless*, or, to be more precise, unchanged by rotations in R, G, B color space). More direct experimental tests of the number of colours were provided first by measurements of the decay width of $\pi^0 \rightarrow \gamma\gamma$ decays, which turns out to be proportional to N_C^2 [3], and later by the famous R ratio in e^+e^- collisions, that we will discuss later on.

1.2 The Lagrangian of QCD

Quantum Chromodynamics, as already stated, is based on the SU(3) gauge group, that is, the 3-dimensional *special unitary* group. Since there are a total of 9 linearly independent unitary complex matrices, one of which has determinant -1, there are a total of 8 independent directions in this matrix space, corresponding to the 8 *generators* of the group, as compared with the single one for QED. In the context of QCD, we commonly represent this group using the so-called *fundamental* or *defining* representation, in which the generators of the group are written as traceless and hermitian matrices. From now on we will refer to the indices enumerating the the rows and columns of this matrices (from 1 to 3) as *fundamental* indices, and use the letters i, j, k, \dots , to denote them. Meanwhile,

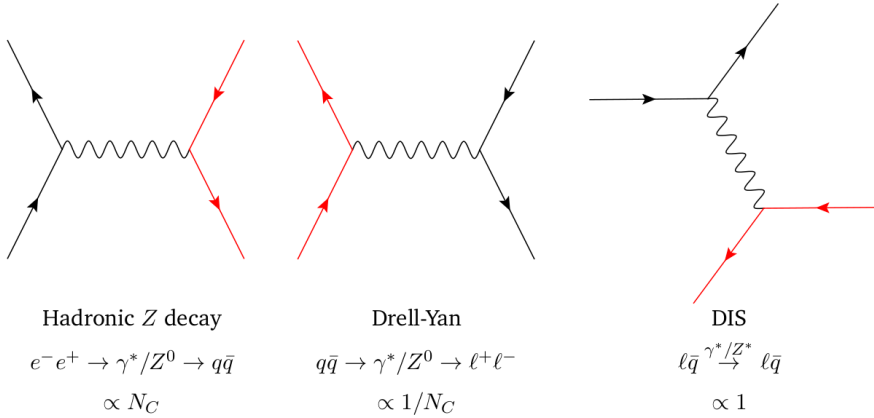


Figure 1.2: Illustration of the three crossings of the interaction of a lepton current (black) with a quark current (red) via an intermediate photon or Z boson, with the corresponding colour factors.

we will use the letters a, b, c, \dots , to refer the indices enumerating the generators (from 1 to 8), also called *adjoint* indices. A detailed derivation of the QCD Lagrangian from local gauge invariance under $SU(3)$, in analogous way to what it is done for building the QED Lagrangian from local $U(1)$ invariance, is shown in Chapter 14 of [9]. The classical Lagrangian for such a theory, involving only quarks and gluons, is written as

$$\mathcal{L} = \bar{\psi}_q^i (i\gamma^\mu) (D_\mu)_{ij} \psi_q^j - m_q \bar{\psi}_q^i \psi_{qi} - \frac{1}{4} F_{\mu\nu}^a F^{a\mu\nu}, \quad (1.3)$$

where ψ_q^i denotes a quark field with fundamental color index i , $\psi_q = (\psi_{qR}, \psi_{qB}, \psi_{qG})^T$, γ_μ is the Dirac matrix expressing the vector nature of the strong interaction, being μ the Lorentz vector index, and m_q represents the quark mass. $F_{\mu\nu}^a$ is the field strength tensor for a gluon with adjoint colour index a ,

$$F_{\mu\nu}^a = \partial_\mu A_\nu^a - \partial_\nu A_\mu^a + g_s f^{abc} A_\mu^b A_\nu^c, \quad (1.4)$$

being D_μ the QCD covariant derivative, whose elements are given by

$$(D_\mu)_{ij} = \delta_{ij} \partial_\mu - i g_s t_{ij}^a A_\mu^a, \quad (1.5)$$

with g_s the strong coupling, related to the usual α_s coupling by $\alpha_s = g_s^2/4\pi$. A_μ^a is the gluon field with colour index a , and t_{ij}^a proportional to the hermitian and traceless Gell-Mann matrices of $SU(3)$. These generators are the $SU(3)$ analogs to the Pauli matrices in $SU(2)$. By convention, the constant of proportionality is normally taken to be

$$t_{ij}^a = \frac{1}{2} \lambda_{ij}^a. \quad (1.6)$$

This choice in turn determines the normalization of the coupling g_s , via equation 1.5, and fixes the values of the $SU(3)$ Casimir operators and structure constants.

As already stated, the colour degree of freedom is introduced in a very specific way, since no coloured objects have been directly observed in nature. Given that we do not measure color in a final state, we average over all possible incoming colours and sum

over all possible outgoing ones, in such a way that a QCD scattering amplitude in practice always contains sums over quark field contracted with Gell-Mann matrices. These contractions in turn produce traces which yield the *colour factors* that are associated to each QCD process, and which basically count the number of "paths through colour space" that the process at hand can take.

A very simple example of a colour factor is given by the decay process $Z \rightarrow q\bar{q}$. This contains a simple δ_{ij} factor in colour space, since the outgoing quark and antiquark must have identical color and anti-color. Squaring the corresponding matrix element and summing over final state colours yields a colour factor of

$$\sum_{\text{colours}} |\mathcal{M}|^2 \sim \delta_{ij}\delta_{ji}^* = \text{Tr}\{\delta\} = N_C = 3. \quad (1.7)$$

A next-to-simplest example, that we will revisit in the following chapters, is the so-called lepton pair production, or Drell-Yan process, given by $q\bar{q} \rightarrow \gamma^*/Z \rightarrow e^+e^-$, which is just a crossing of the previous one. By crossing symmetry, the squared matrix element, including the colour factor, is exactly the same as before, but since the quarks are here incoming, we must *average* rather than sum over their colours, leading to

$$\sum_{\text{colours}} \frac{1}{9} |\mathcal{M}|^2 \sim \frac{1}{9} \delta_{ij}\delta_{ji}^* = \frac{1}{9} \text{Tr}\{\delta\} = \frac{1}{3}, \quad (1.8)$$

where the colour factor now expresses a *suppression* due to the fact that only quarks of matching colours are able to collide to produce a Z boson. The chance that a quark and antiquark picked at random from the initial state have matching colours is $1/N_C$.

Similarly, $l_q \rightarrow l_q$ via the t -channel photon exchange (usually called Deep Inelastic Scattering), constitutes yet another crossing of the same process, see figure 1.2. The color factor of this process comes out as unity.

We will not go with much detail into more complicated processes, such that the ones involving quark-gluon vertices, as the one depicted in figure 1.3. Just remark that the task of taking traces over t matrices can be greatly simplified by the use of the relations given in Figure 1.5. In the standard normalization convention for the SU(3) generators, given in equation 1.6, the Casimirs appearing in 1.5 are

$$T_R = \frac{1}{2}, \quad C_F = \frac{4}{3}, \quad C_A = 3. \quad (1.9)$$

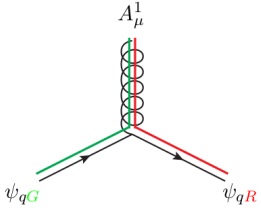
In addition, notice that the gluon self-coupling on the third line of Figure 1.5 involves a factor f^{abc} . These are called *structure constants* of QCD and they enter via the non-abelian term in the gluon field strength tensor $F_{\mu\nu}^a$ from equation 1.4. The structure constants of SU(3) are listed in Figure 1.6.

They define the *adjoint*, or *vector* representation of SU(3) and are related to the fundamental representation generators via the commutator relations

$$t^a t^b - t^b t^a = [t^a, t^b] = i f^{abc} t_c, \quad (1.10)$$

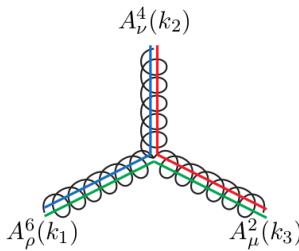
or equivalently

$$i f^{abc} t_c = 2 \text{Tr}\{t^c [t^a, t^b]\}. \quad (1.11)$$



$$\begin{aligned}
 &\propto -\frac{i}{2}g_s \quad \bar{\psi}_{qR} \quad \lambda^1 \quad \psi_{qG} \\
 &= -\frac{i}{2}g_s \quad (1 \ 0 \ 0) \quad \begin{pmatrix} 0 & 1 & 0 \\ 1 & 0 & 0 \\ 0 & 0 & 0 \end{pmatrix} \quad \begin{pmatrix} 0 \\ 1 \\ 0 \end{pmatrix}
 \end{aligned}$$

Figure 1.3: Illustration of a qqg vertex in QCD, before summing/averaging over colours: a gluon in a state represented by λ^1 interacts with quarks in the states ψ_{qR} and ψ_{qG} .



$$\begin{aligned}
 &\propto -g_s f^{246} [(k_3 - k_2)^\rho g^{\mu\nu} \\
 &\quad + (k_2 - k_1)^\mu g^{\nu\rho} \\
 &\quad + (k_1 - k_3)^\nu g^{\rho\mu}]
 \end{aligned}$$

Figure 1.4: Illustration of a ggg vertex in QCD, before summing/averaging over colours: interaction between gluons in states $\lambda^2, \lambda^4, \lambda^6$ represented by the structure constant f^{246} .

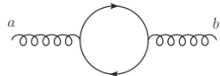

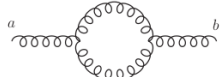
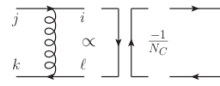
Trace Relation	Indices	Occurs in Diagram Squared
$\text{Tr}\{t^a t^b\} = T_R \delta^{ab}$	$a, b \in [1, \dots, 8]$	
$\sum_a t_{ij}^a t_{jk}^a = C_F \delta_{ik}$	$a \in [1, \dots, 8]$ $i, j, k \in [1, \dots, 3]$	
$\sum_{c,d} f^{acd} f^{bcd} = C_A \delta^{ab}$	$a, b, c, d \in [1, \dots, 8]$	
$t_{ij}^a t_{k\ell}^a = T_R \left(\delta_{jk} \delta_{i\ell} - \frac{1}{N_C} \delta_{ij} \delta_{k\ell} \right)$	$i, j, k, \ell \in [1, \dots, 3]$	 (Fierz)

Figure 1.5: Trace relations for t matrices (convention-independent). Other useful relations of the QCD generators and Casimir operators can be found in [1] [3]

Structure Constants of SU(3)

$$f_{123} = 1 \quad (14)$$

$$f_{147} = f_{246} = f_{257} = f_{345} = \frac{1}{2} \quad (15)$$

$$f_{156} = f_{367} = -\frac{1}{2} \quad (16)$$

$$f_{458} = f_{678} = \frac{\sqrt{3}}{2} \quad (17)$$

Antisymmetric in all indices

All other $f_{abc} = 0$

Figure 1.6: Structure constants of SU(3)

Thus, it is a matter of choice whether one prefers to express colour space on basis of fundamental-representation of t matrices, or via the structure constants f_{abc} . Expanding the $F_{\mu\nu}F^{\mu\nu}$ term in the Lagrangian using equation 1.4, we see that there is a 3-gluon and 4-gluon vertex that involve f^{abc} , the latter of which has two powers of f and two powers of the coupling. Finally, the last line of the table is not really a trace but instead a useful so-called Fierz transformation, which expresses products of t matrices in terms of Kronecker δ functions².

A gluon self-interaction vertex is illustrated in figure 1.4, compared with the quark-gluon one in Figure 1.3. We remind the reader that gauge boson self-interactions are a hallmark of non-abelian theories and that their presence leads to the main differences between QED and QCD.

1.3 The strong coupling

In this section we provide an introduction to the renormalization group formalism and the concept of running coupling, which will allow for the description of *confinement* of quarks, and will also lead to the result that QCD exhibits *asymptotic freedom*.

We start with a brief summary of how renormalization works. In the context of QED, we know how the electric charge is modified by the vacuum polarization loops in the photon propagator³. After a proper reparametrization, which takes us from the bare to the physical charge, loops lead to finite and measurable effects. We know that the loop will be repeated in higher orders as shown in 1.7, which can be also written as 1.8, and the geometric series can be summed to give 1.9. While a detailed description of the

²Fierz transformation is often used, for instance, in shower Monte Carlo applications, to assist in mapping between colour flows in $N_C = 3$ and the so called *large number of colors*, or *leading colour* approximation.

³The infinities appearing in loop diagrams are a consequence of a naive definition of the electric (or color) charge. After a proper reparametrization, which takes us from the bare to the physical charge, loops lead to finite and measurable effects. The calculations based on renormalization agree with experiment, for which the Lamb shift and the anomalous magnetic moment are dramatic illustrations. For a more detailed description see [1, 9].

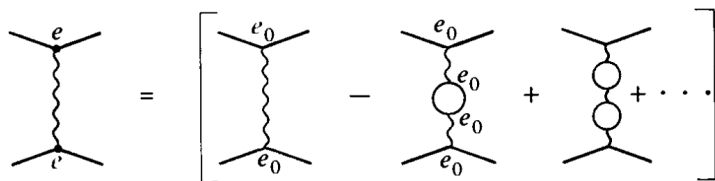


Figure 1.7: Vacuum polarization loops in photon propagator at higher orders.

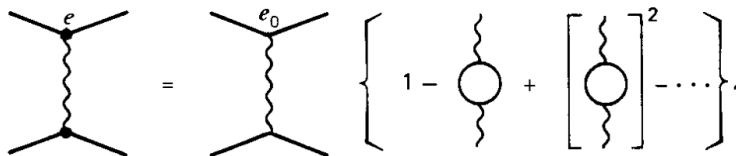


Figure 1.8: Vacuum polarization loops in photon propagator, expressed as geometric series.

renormalization procedure can be found in [1, 9], let us show here the solution found by redefining the coupling including all vacuum polarization loops as given by 1.9. This leads to the fact that the charge measured by an experiment depends on the momentum μ^2 of the experiment, and hence $\alpha(\mu^2)$ is referred to as the *running coupling*. The leading order behavior of $\alpha(\mu^2)$ is written in terms of a reference or *renormalization* scale μ_R as follows:

$$\alpha_s(\mu^2) = \frac{\alpha_s(\mu_R^2)}{1 - \frac{\alpha_s(\mu_R^2)}{3\pi} \log \frac{\mu^2}{\mu_R^2}} \quad (1.12)$$

The running coupling $\alpha(\mu^2)$ describes how the effective charge depends on the separation of the charged particles. As μ^2 increases, the photon sees more and more charge until, at some unphysically large but finite μ^2 , the coupling $\alpha(\mu^2)$ eventually diverges. We will return to this point when describing the running coupling in QCD.

Let us now deal with QCD, where crucial differences appear. One could try to proceed as it was done for renormalization in QED, replacing lepton fields by quarks and photon loops by gluons. But the cancellation in QCD is much more complicated, given the self-coupling among gluons - with origin in the SU(3) structure of QCD - and requires the introduction of a "ghost" field to cancel the unphysical polarizations. Another much more elegant way of describing the running of the coupling with the energy comes under the name of *renormalization group*.

In the limit of Bjorken scaling - first order approximation, or QCD at fixed coupling - properties of high-energy interactions are determined only by dimensionless kinematic quantities, such as rapidities in the scattering amplitudes and ratios of energy scales. Indeed, the observed approximate agreement was used as a powerful argument for the point-like structure of partons. Since measurements at different energies are sensitive to different resolution scales, independence of the absolute energy scale is indicative of the absence of other fundamental scales in the problem and hence of point-like constituents. The running is logarithmic with energy, and it is governed by the so-called *beta function*,

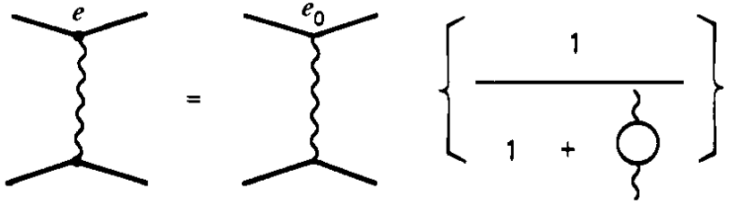


Figure 1.9: Result of the photon propagator after summing the geometric series.

as given in the so-called Callan-Symanzik equation, or *renormalization-group equation*

$$\frac{d\alpha_s}{d \ln \mu^2} = \mu^2 \frac{d\alpha_s}{d\mu^2} = \beta(\alpha_s(\mu^2)) \quad (1.13)$$

where the β function can be expanded as a perturbative series in α_s as

$$\beta(\alpha_s) = -\alpha_s^2 (\beta_0 + \beta_1 \alpha_s + \beta_2 \alpha_s^2 + \dots). \quad (1.14)$$

The β_i coefficients are known up to 5 loops ($i = 3$). More details on the analytic solutions on the equation can be found in [1, 3, 9]. The LO (1-loop) and NLO (2-loop), NNLO (3-loop) behavior are given by the LO, NLO, NNLO coefficients

$$\begin{aligned} \beta_0 &= \frac{1}{12\pi} (11C_A - 2n_f), \\ \beta_1 &= \frac{1}{24\pi} (17C_A^2 - 10T_R C_A n_f - 6T_R C_F C_F n_f) \\ \beta_2 &= \frac{1}{64} \left(\frac{2857}{54} C_A^3 + \frac{1415}{54} C_A^2 n_f - \frac{205}{18} C_A C_F n_f + C_F^2 n_f + \frac{79}{54} C_A n_f^2 + \frac{11}{9} C_F n_f^2 \right), \end{aligned} \quad (1.15)$$

and so on and so forth. Here n_f is the number of QCD massless flavours, and the $SU(N_C)$ colour factors are $C_A = N_C$ and $C_F = (N_C^2 - 1)/(2N_C)$.

In the β_0 coefficient, the first term is due to gluon loops while the second is due to quark ones. Similarly, the first term of the β_1 coefficient arises from double gluon loops, while the second and third represent mixed quark-gluon ones. At higher loop orders, the β_i coefficients depend explicitly on the regularization and renormalization scheme that is used ⁴. A brief discussion can be found in the PDG review on QCD [17].

Note that, if there are additional coloured particles beyond the Standard Model ones, loops involving those particles would affect the coefficients of the beta function at energy scales above the masses of the new particles, thus modifying the running of the coupling.

⁴A detailed description of the principles of dimensional regularization, together with the definition of the minimal subtraction (MS) and the modified minimal subtraction ($\overline{\text{MS}}$) scheme can be found in the notes by Guido Altarelli "Collider Physics within the Standard Model". The ($\overline{\text{MS}}$) definition of α_s is one of the most commonly adopted in literature, and values quoted for it normally refer to this definition.

What this year's Laureates discovered was something that, at first sight, seemed completely contradictory. The interpretation of their mathematical result was that the closer the quarks are to each other, the weaker is the "colour charge". When the quarks are really close to each other, the force is so weak that they behave almost as free particles^a. This phenomenon is called "asymptotic freedom". The converse is true when the quarks move apart: the force becomes stronger when the distance increases^b.

^aMore correctly, it is the coupling rather than the force which becomes weak as the distance decreases. The $1/r^2$ Coulomb singularity of the force is only dampened, not removed, by the diminishing coupling.

^bMore correctly, it is the potential which grows, linearly, while the force becomes constant.

Figure 1.10: Extract of the prize announcement for D.Gross, H.Politzer, F.Wilczek in 2004.

By solving the renormalization-group equation we find the behavior of the coupling in terms of the energy⁵. The LO behavior is showed below

$$\alpha_s(\mu^2) = \frac{\alpha_s(\mu_R^2)}{1 + b_0\alpha_s(\mu_R^2)\ln\frac{\mu^2}{\mu_R^2} + \mathcal{O}(\alpha_s^2)} \quad (1.16)$$

where, again, the numerical value of the strong coupling is usually specified by giving its value at some physical scale μ_R , referred to as renormalization scale. Typical values for this reference scale are $\mu_R = M_Z$, the mass of the Z boson around 90 GeV.

Contrary to the QED case, the negative overall sign of equation 1.14, combined with the fact that $\beta_0 > 0$ (which holds true for $n_f < 17$), leads to the famous result that the QCD *decreases* with energy, and hence QCD is what we call *asymptotically free*. A discovery for which the Nobel price in physics was awarded to D.Gross, H.Politzer, and F.Wilczek, in 2004. An extract of the price announcement is reported as follows in figure 1.10.

Note that this is quite a convenient result, since the energies we access with collider experiments like the LHC will be typically very large, and will allow the application of perturbation theory that is perfectly well-defined. On the other hand, this is the reason why QCD can *only* be solved analytically through a perturbative approach at very high energies. In other words, one of the main consequences of asymptotic freedom is that perturbation theory becomes better behaved at higher absolute energies, due to the efficiently decreasing coupling. Furthermore, since the running of α_s explicitly breaks Bjorken scaling, we also expect to see small changes in jet shapes and in jet production ratios as we vary energy. Our current understanding of the QCD running coupling is summarized by the plot in figure 1.11, taken from a recent comprehensive review by S.Bethke [18].

As a final remark on the asymptotic freedom, note that the decreasing value of the strong coupling with energy must eventually cause it to become comparable to the electromagnetic and weak ones, at some energy scale. Beyond that point, which may lie at energies of order $10^{15} - 10^{17}$ GeV, we do not know what the further evolution of the combined theory will actually look like, or whether it will continue to exhibit asymptotic

⁵Note that only at leading order, counting just with the β_0 coefficient, the equation can be solved by separation of variables. At higher orders, though, the equation needs to be solved applying a recursive procedure, inserting the LO solution for the computation of the NLO, and so on and so forth.

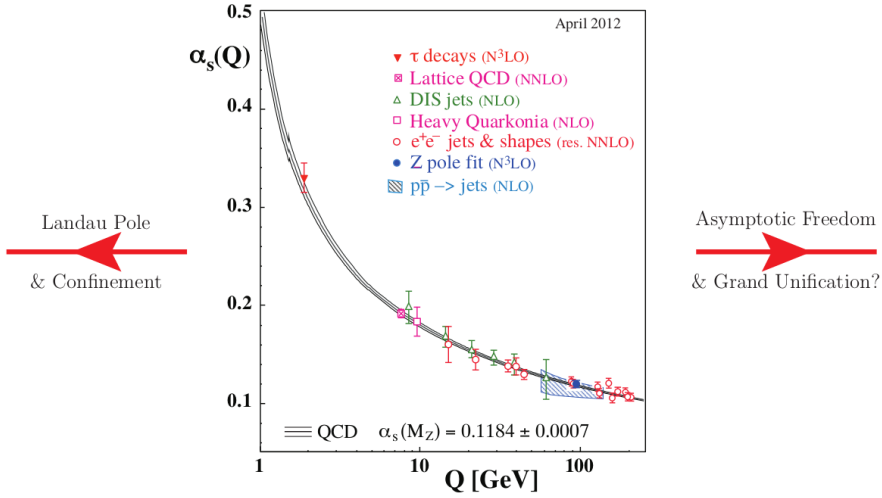


Figure 1.11: QCD running coupling at different energy scales, taken from [17, 18].

freedom. Now consider what happens when we run the coupling in the other direction, towards smaller energies. Taken at face value, the numerical value of the coupling diverges rapidly at scales below 1 GeV, as illustrated in by the curves disappearing off the left-hand edge of the plot in figure 1.11. To make the singularity explicit, we can write equation 1.16 in the following form ⁶.

$$\alpha_s(\mu^2) = \frac{1}{b_0 \ln \frac{\mu^2}{\Lambda^2}}, \quad (1.17)$$

where

$$\Lambda \sim 200 \text{ MeV} \quad (1.18)$$

specifies the energy scale at which the perturbative coupling would nominally become infinite, the so-called *Landau pole*, which indicates the energy scale where perturbation theory for QCD breaks down. Finally, one should be aware that there is a multitude of different ways of defining both Λ and $\alpha_s(\mu_R)$. At the very least, the numerical value one obtains depends both on the renormalization scheme used and on the perturbative order of the calculations used to extract them. Typically, fits to experimental data yield smaller values for $\alpha_s(M_Z)|_{\text{LO}} \gtrsim \alpha_s(M_Z)|_{\text{NLO}} \gtrsim \alpha_s(M_Z)|_{\text{NNLO}}$.

The behavior of α_s at low energy scales is compatible with confinement. In nature, as we already know, we don't ever see isolated quarks or gluons, but only hadrons, i.e. composite objects made of quarks and gluons which belong to the singlet representation of the gauge group SU(3). As a consequence of the running of α_s , we can not describe the strong interactions in the small energy regime by use of perturbative QCD (pQCD for short); Even counting on lattice simulations, which provide fine description of QCD at small energies and some evidence that quarks confine, a complete non-perturbative

⁶Note, however, that this only parametrizes the purely *perturbative* result, which is not reliable at strong coupling, so equation 1.17 should not be taken to imply that the physical behavior of full QCD should exhibit a divergence at $\mu \rightarrow \Lambda$.

explanation is still missing. We can conclude here that, being composite objects, the description of the interaction between hadrons and other particles is more complicated than for elementary particles. The renormalization group allows us to understand the asymptotically free behavior of QCD, and hence to safely apply perturbative QCD in this regime for producing accurate predictions.

Hadronic processes and factorization

2.1 Parton Model and factorization

We just discussed in Chapter 1 the perturbative approach to the strong interactions, and how pQCD is theoretically justified given the asymptotic freedom of QCD. At high energies, it becomes small enough to be considered a perturbative parameter, and we can study the interactions between the fundamental fields of the theory, i.e., quarks and gluons, as if they were weakly coupled. In other words, we can compute observables via the Feynman diagrams approach.

However, the short-distance (hard) scattering between particles of QCD can not be directly observed. Indeed, due to confinement, in any measurement we perform we are forced to also deal with long distance (soft) contributions, since the elementary objects going through the hard interaction will then hadronize to form the objects that are measured in a final state. Unfortunately, a perturbative approach can not be applied on such hadronization processes, and at first sight the application of pQCD on scattering experiments seems doomed to fail. The entire picture is encoded in the so-called *Parton Model*¹, that we described below:

- At high enough energies, a scattering within a hadron can be described by a scattering within the various constituents of the hadron - *partons* - which can be considered as point-like and freely moving.
- Any probe interacts with only one parton, with multiple scattering remaining negligible at all effects.

Under these assumptions, a scattering involving a hadron can be seen as the product between the probability to find a particular parton inside the hadron times the scattering involving the parton, summed over all the possible partons inside the hadron in the initial state. By identifying these partons with the fundamental quarks and gluons of QCD, we are able to separate the long and short-distance dynamics.

In other words, we face the complication that hadrons are composite, with a time-dependent structure illustrated in Figure 2.1; the internal dynamics of the hadron involves a complex structure of constantly interacting partons, being emitted and absorbed at very short time scales. Thus, before we can use perturbatively calculated scattering amplitudes, we must first address the partonic structure of the colliding hadrons.

¹First postulated by Bjorken [19] and Feynman [20].

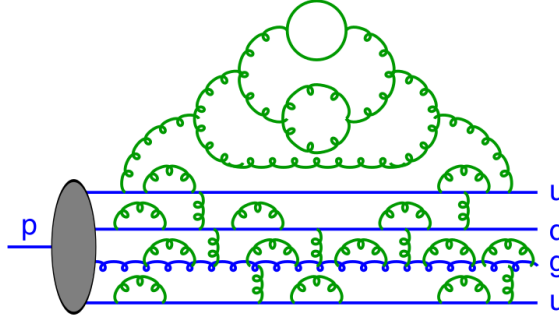


Figure 2.1: Representation of the partonic fluctuations inside a hadron.

For the hadron to remain intact, the fluctuations inside it must involve momentum transfers smaller than the confinement scale. Indeed, high-virtuality fluctuations are suppressed by powers of

$$\frac{\alpha_s \Lambda^2}{|k|^2}, \quad (2.1)$$

with the confinement scale ($\Lambda \sim 200$ MeV, see Chapter 1) and $|k|$ the virtuality of the fluctuation. Thus, most fluctuations take place over timescales of the order $1/\Lambda$. By looking at a DIS experiment as the one depicted in Figure 1.2, the scattered photon interacts over a much shorter time scale $1/Q \ll 1/\Lambda$, during which the partonic fluctuations inside the hadron appear almost frozen. The hard probe effectively takes an instantaneous snapshot of the hadron structure, at a characteristic resolution given by $1/Q$.

This is formalized by the *factorization theorem* [21], which expresses the independence of long-wavelength (soft) structure and the short-distance (hard) process. Originally formulated for DIS, the factorization theorem allows us to write the cross section for lepton-hadron scattering as a convolution of a non-perturbative but universal (i.e., process independent) parton density function (PDF) and a perturbatively calculable partonic scattering cross section. Denoting by x_i the fraction of the hadron momentum carried by a parton of flavour i ,

$$\mathbf{p}_i = x_i \mathbf{p}_h, \quad (2.2)$$

we can write the lepton-hadron cross section in factorized form

$$\sigma_{lh} = \sum_i \int_0^1 dx_i \int d\Phi_F f_{i/h}(x_i, \mu_F^2) \frac{d\hat{\sigma}_{li \rightarrow F}(x_i, \Phi_F, \mu_F^2)}{dx_i d\Phi_F}, \quad (2.3)$$

with the i index running over all possible parton types in the incoming hadron, F describing all possible partonic final states, and $d\Phi_F$ the Lorentz-invariant phase space volume element. Note that eq. 2.3 is valid only up to power corrections.

In this last expression two main quantities towards the computation of a hadronic observable are shown. The *parton densities*, also referred to as *parton distribution functions* are denoted by $f_{i/h}$, and they parametrize the distribution of partons inside the target hadron. They are not a priori calculable within a perturbative framework, and therefore

they must be constrained by fits to data, as it is discussed in section 2.2.

On the other hand, the *partonic cross section*, $d\hat{\sigma}$, describes the pure partonic interaction, meaning the short-distance dynamics in the hard scattering. It is calculable in perturbation theory, as it is discussed in section 2.3.

There are three main classes of hard processes, that we will describe with detail in the next chapters: those with no hadronic particles in the initial state, like e^+e^- annihilation, those initiated by a lepton and a hadron, like DIS, and those with two incoming hadrons, like $p\bar{p}$ (Tevatron) or pp (LHC). The parton densities, defined and measured in DIS, are instrumental to compute hard processes initiated by collisions of the form $h_1 + h_2 \rightarrow F + X$, where h_i are hadrons and F some triggered final state particle, or system of particles, or one or more jets which specify the large scale Q^2 relevant for the process. For example, F can be a W^\pm , or a Z , or a virtual photon with large Q^2 , (Drell-Yan process), or a jet with large transverse momentum q_T , or a heavy quark-antiquark pair. By X we mean totally inclusive collection of particles that can appear in our final state.

For the purpose of this thesis we deal with LHC physics, meaning processes with two hadrons in the initial state. The factorization theorem states that, for the total cross-section - or some other sufficiently inclusive distribution - we can write, apart from power suppressed corrections, the following expression

$$\sigma(s, \tau) = \sum_{AB} \int dx_1 dx_2 f_{1A}(x_1, Q^2) f_{2B}(x_2, Q^2) \hat{\sigma}_{AB}(x_1 x_2 s, \tau). \quad (2.4)$$

Here $\tau = Q^2/s$ is a scaling variable, f_{1A} and f_{2B} are the probability densities for a parton of type A or B inside the hadron h_i , and $\hat{\sigma}_{AB}$ is the partonic, or *hard* cross section for

$$\text{parton } A + \text{parton } B \rightarrow F + \hat{X}. \quad (2.5)$$

Here \hat{X} is the partonic version of X , i.e., an inclusive collection of quarks and gluons. This result is based on the fact that the mass singularities associated with initial legs are of universal nature, so that one can reproduce the same modified parton densities by absorbing these singularities into the bare parton densities, as in DIS. Once the parton densities and α_s are known from other measurements, the prediction of the rate for a given hard process is obtained within the corresponding theoretical ambiguity (e.g., from scale dependence or hadronization effects).

The residual scale and scheme dependence is often the most important source of theoretical error. Therefore one could ask to what extent the factorization theorem has been proven. In perturbation theory up to NNLO, it has been explicitly checked to hold for many processes: if corrections exist we already know that they must be small. The LHC experiments offer a wonderful opportunity for testing the factorization theorem by comparing precise theoretical predictions with accurate data on a wide variety of processes.

A great effort has been and is being devoted to the theoretical preparation and interpretation of the LHC experiments. For this purpose, very complex calculations are needed at NLO and beyond because the strong coupling, even at large Q^2 values involved, is not negligible and radiative corrections can be sizeable.

2.2 Parton densities

As we just discussed, in order to calculate hadronic cross sections one needs to factorize the short-distance (hard) and the long-distance (soft) physics. This is done by writing a hadronic observable as the convolution of some partonic object, describing the interaction between two partons in the initial state, and then convoluting it with the *parton densities*, or *parton distribution functions*, which encode the information about how those partons were distributed inside the hadron.

Strictly speaking, the parton density $f_{i/h}(x, \mu_F^2)$ represents the effective density of partons of flavour i as a function of the momentum fraction x , when a hadron of type h is probed at the factorization scale μ_F . The PDFs are non-perturbative functions which are not a priori calculable, but a perturbative differential equation governing their evolution can be obtained by requiring that physical scattering cross sections are independent of μ_F to a given perturbative orders. The resulting *renormalization group equation* is called DGLAP² equation, and it can be used to evolve the PDFs from one perturbative scale to another. This means that we only need to determine the form of the PDFs as a function of x at a single, arbitrary scale μ_0 . We can then get its form at any other scale μ_F by simple RGE evolution.

The derivation DGLAP from scale invariance can be somehow complex, involving general treatment of the Callan-Symanzik equation in the context of factorization and aspects about OPE expansion, which are beyond the scope of this thesis. Hence we limit ourselves to present final results, while the interested reader can see the refs [25, 26]. For a given physical observable \mathcal{O} , the scale-invariance condition

$$\mu_F^2 \frac{\partial \mathcal{O}}{\partial \mu_F^2} = 0 \quad (2.6)$$

can be fulfilled by requiring that the PDFs solve the following set of $n_f + 1$ equations, known in literature as DGLAP, or Altarelli-Parisi equations

$$\mu_F^2 \frac{\partial}{\partial \mu_F^2} \begin{pmatrix} q_i(x, \mu_F^2) \\ g(x, \mu_F^2) \end{pmatrix} = \int_0^1 \frac{dz}{z} \begin{pmatrix} P_{q_i, q_j} \left(\frac{x}{z}, \alpha_s(\mu_F^2) \right) & P_{q_i, g} \left(\frac{x}{z}, \alpha_s(\mu_F^2) \right) \\ P_{g, q_j} \left(\frac{x}{z}, \alpha_s(\mu_F^2) \right) & P_{g, g} \left(\frac{x}{z}, \alpha_s(\mu_F^2) \right) \end{pmatrix} \begin{pmatrix} q_i(z, \mu_F^2) \\ g(z, \mu_F^2) \end{pmatrix} \quad (2.7)$$

where the various P_{ij} are the Altarelli-Parisi splitting functions, controlling the universal collinear splitting of a parton i into a parton j . They admit a perturbative expansion in powers of α_s , leading to a perturbative solution for the DGLAP equation. Expansion of the splitting functions at first order leads to the dominant - or *leading* logarithm accuracy PDFs, while the introduction of further orders in the splitting functions permits to include subleading logarithmic contributions. The explicit perturbative solution of eq. 2.7, together with the expression for the leading order of the splitting kernels are collected in Appendix B.

Note that DGLAP equations are hence used to run the PDFs from one perturbative resolution to another. This means that whatever the initial scale μ_0 is, we can then get its form at any another scale μ_F , which we will use for applying the factorization theorem, by simple RGE evolution. This leads us to the next feature about PDF estimation: the

²DGLAP: Dokshitzer-Gribov-Lipatov-Altarelli-Parisi [22, 23, 24]

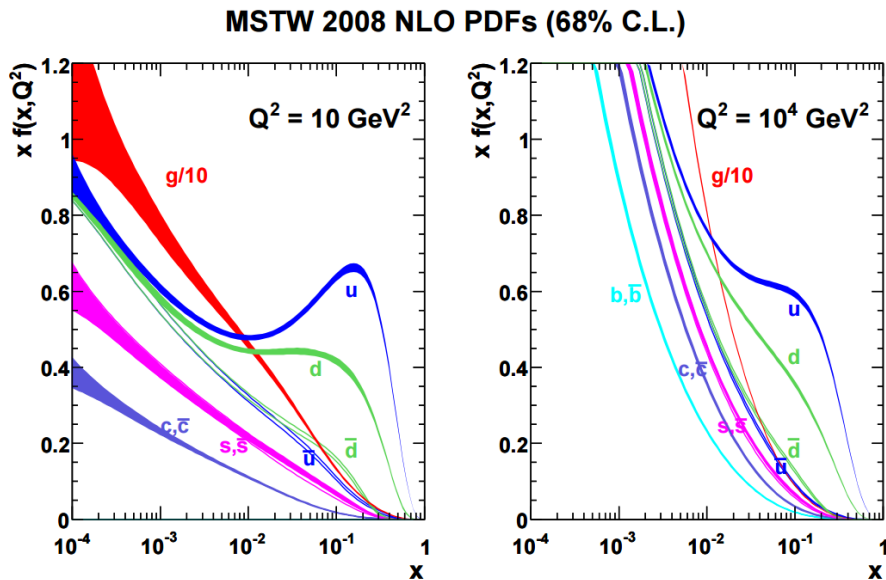


Figure 2.2: Representation of the parton distributions for the different quark flavours and the gluon, as a function of the momentum fraction x , probed at a given transfer momentum Q^2 . On the right-hand side, the PDFs are scaled at a higher value of $Q^2 = 10^4$ GeV, and hence the dependence with x differs from the one probed at $Q^2 = 10$ GeV. Extracted from and MSTW 2008 PDF dataset.

PDF fitting process.

Many collaborations, such as the CTEQ, MSTW, NNPDF, are devoted to PDF fitting, meaning the task of constraining the form of the PDF functions by fitting cross sections to experimental data, e.g. from DIS, Drell-Yan and $pp \rightarrow$ jets. For a deeper review see [27, 28, 29]. In the context of PDF fits, the reference scale μ_0 is usually taken to be relatively low, of order one or a few GeV. Note also that different collaborations apply different ansätze for the form of the $f(x, \mu_0)$, and also quite different models lying in large sets of parameters. They may also include different data in the fits, and also treat or weight the data differently. Hence, results from different groups may not always be mutually compatible. For the time being, it is recommended to try at least sets from two different groups, for a comprehensive uncertainty estimate.

Concerning terminology, the words *structure functions* and *parton densities* are commonly used interchangeably. However, there is an important distinction between the two, which we find often in (quantum) physics. The former is a physical observable used to parametrize cross section, while the latter is a “fundamental” quantity extracted from it. In particular, since the parton densities are not themselves a physically observable, they can only be defined within a specific factorization scheme³ order by order in perturbation theory. The only exception is at leading order, at which they have the simple physical interpretation of parton number densities. When going to higher orders,

³For all practical purposes, when focusing on LHC physics it is likely to encounter only one of such schemes, the modified minimal subtraction $\overline{\text{MS}}$, already mentioned in the discussion of the definition of the strong coupling in Section 1.3.

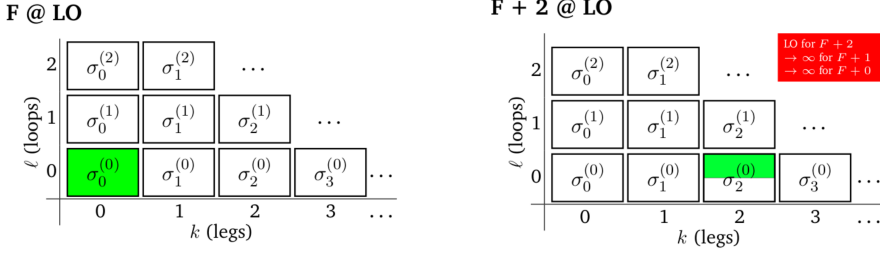


Figure 2.3: Coefficients of the perturbative series in LO calculations. On the left, F production at LO. On the right, $F + 2$ jet at LO, with half-shaded boxes illustrating the restriction to the region of phase space with exactly 2 resolved jets. The total power of α_s for each coefficient is given by $n = k + l$.

though, we tend to keep the simple intuitive picture from LO in mind, but one should be aware that the fundamental relationship between PDFs and measured quantities is actually more complicated. Due to the interplay between PDFs and the real and virtual corrections to the LO cross section, the parton densities no longer have a clear probabilistic interpretation starting from NLO, and their definition depends on the factorization scheme.

2.3 Fixed-Order QCD

Now we are ready for addressing the hard interactions, for which perturbation theory can be applied. Consider the production of an arbitrary final state, F (e.g. a Higgs boson, a $t\bar{t}$ pair, a Drell-Yan lepton pair, etc). We can expand the partonic differential cross section for an observable \mathcal{O} is

$$\frac{d\hat{\sigma}_F}{d\mathcal{O}} = \sum_{k=0}^{\infty} d\Phi_{F+k} \left| \sum_{l=0}^{\infty} \mathcal{M}_{F+k}^{(l)} \right|^2 \delta(\mathcal{O} - \mathcal{O}(\Phi_{F+k})) . \quad (2.8)$$

Here, $\mathcal{M}_{F+k}^{(l)}$ is the amplitude for producing the final state F in association with k additional final-state partons, also called "legs" in the diagrammatic sense, and with l additional loops. The sum starts at $k = 0$ and $l = 0$, corresponding to the leading order (LO) for producing F , while higher terms represent real and virtual contributions, respectively. The delta function determines the dependence on the phase space, since \mathcal{O} represent the full $d\Phi_{F+k}$ phase space, and $\mathcal{O}(\Phi_{F+k})$ is a function that defines \mathcal{O} evaluated at each specific momentum configuration. We obtain the various fixed-order truncations of perturbative QCD by limiting the nested sums in equation 2.8 to include some specific values of $k + l$. Thus,

$k = 0, l = 0 \implies$ Leading Order (tree-level) for F production

$k = n, l = 0 \implies$ Leading Order (tree-level) for F plus jets

$k + l \leq n \implies$ N^n LO for F (includes N^{n-1} LO for $F + 1$ jet, N^{n-2} LO for $F + 2$ jet, etc)

For $k \geq 1$ we are not considering inclusive F production; instead we are dealing with $F + k$ jets. If we simply integrate over momenta, as implied by the integration over

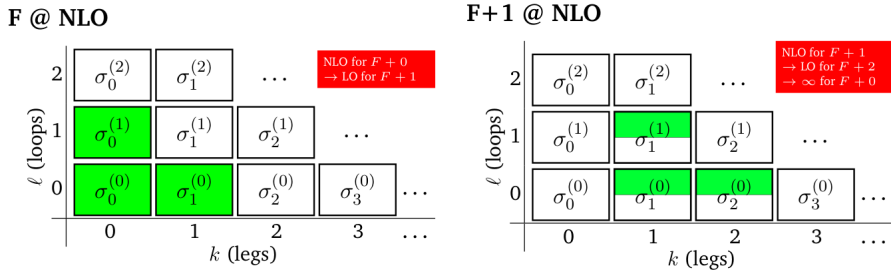


Figure 2.4: Coefficients of the perturbative series in NLO calculations. On the left, F production at NLO. On the right, $F + 1$ jet at NLO, with half-shaded boxes illustrating the restriction to the region of phase space with exactly 1 resolved jet. The total power of α_s for each coefficient is given by $n = k + l$.

the $d\Phi_{F+k}$ in equation 2.8, we would be including configurations in which one or more of the k partons can be soft and collinear. Such configurations lead to infrared divergences in QCD and hence must be regulated. Imposing cuts on angles, energies or other kinematic variables such as transverse momenta, we are able to cut away problematic regions of the phase space.

Recall that regularization cuts on a dimensional quantity, like energy or transverse momentum, should be formulated as a *ratio* of scales, rather than as an absolute number. For instance, a jet with $q_T = 50$ GeV would be considered hard and well-separated depending on the process, and in particular on the energy of the hard interaction. Such classification and labeling of the jet would drastically change if produced in association with an ordinary Z boson (with hard scale $M_Z = 90$ GeV), or with a highly virtual (900 GeV) Z' boson.

The main remark at this point, and directly related to the purpose of this thesis, is that, if the regularization scale is taken too low, logarithmic enhancements of the type

$$\alpha_s^n \ln^{m \leq 2n} \left(\frac{Q_F^2}{Q_k^2} \right) \quad (2.9)$$

will generate progressively large corrections order by order, which will spoil any fixed-order truncation of the perturbative series. Here, Q_F - F standing for "Final state" - is the hard scale associated with the process under consideration, and Q_k is the scale associated with an additional parton k , such a momentum fraction, transfer momentum, etc, which would become dangerous when it becomes much smaller than the hard scale Q_F .

One can state, as a rule of thumb, that if $\sigma_{k+1} \sim \sigma_k$, then the perturbative series is converging too slowly for a fixed-order truncation to be reliable. For fixed-order perturbation theory to be applicable, one must apply cuts on the hard process such that $\sigma_{k+1} \ll \sigma_k$. This way, the region where perturbation theory can be applied safely extended.

The virtual amplitudes, for $l \geq 1$, are divergent for any point in the phase space. However, as given by the KLN theorem [30, 31], unitarity puts a powerful constraint on

F @ NNLO

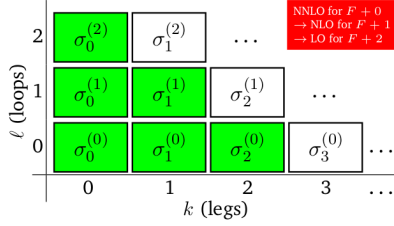


Figure 2.5: Coefficients of the perturbative series in NNLO calculations. The total power of α_s for each coefficient is given by $n = k + l$. Green shading represents the full perturbative coefficient at the respective $k + l$.

the IR divergences, forcing them to cancel exactly against those coming from the unresolved real emissions that we had to cut out above, order by order, making the complete answer for fixed $k + l = n$ finite⁴. It is important to remark that the KLN theorem is only valid for inclusive quantities, like a total cross section. Nevertheless, since this cancellation happens between contributions that formally live in different regions of the phase space, an important aspect of higher-order calculations is how to arrange for this cancellation in practice.

We illustrate in Figure 2.3 the terms of the perturbative series that are included in a given matrix-element-based calculation. In the left-hand side, the shaded box corresponds to the lowest-order “Born-level” matrix element squared. This coefficient is non singular and hence can be integrated over the whole phase space, which we illustrate by letting the shaded area fill all of the relevant box. A different kind of leading-order calculation is represented in the right-hand side of the figure, where the half-shaded box corresponds to the lowest-order matrix element squared for $F + 2$ jets. This coefficient diverges in the phase space region where one or both jets are unresolved (i.e., soft or collinear), and hence integrations can only recover part of the phase space, which we emphasize by only shading the upper half of the box.

Figure 2.4 illustrates the inclusion of NLO virtual contributions. To prevent confusion, let’s pause for a discussion on notation. By $\sigma_0^{(1)}$ we intend

$$\sigma_0^{(1)} = \int d\Phi_0 \, 2\text{Re}[\mathcal{M}_0^{(1)} \mathcal{M}_0^{(0)*}], \quad (2.10)$$

which comes from the Born-virtual interference term, and it is of one order α_s relative to the Born-level. Compare for instance with the expansion on equation 2.8 to $k + l = 1$. In particular, $\sigma_0^{(1)}$ should *not* be confused with the integral over the 1-loop matrix element squared, which would be of relative order α_s^2 and hence forms part of the NNLO coefficient $\sigma_0^{(2)}$. Back to Figure 2.4, the unitarity cancellations between real and virtual singularities imply that we can now extend the integration of the real correction in the

⁴Formally, the KLN theorem states that the sum over degenerate quantum states is finite. In the context of fixed-order perturbation theory, this is exemplified by states with infinitely soft and/or collinear radiation being degenerate with the corresponding states with loop corrections. They can not be told apart by any physical observable.

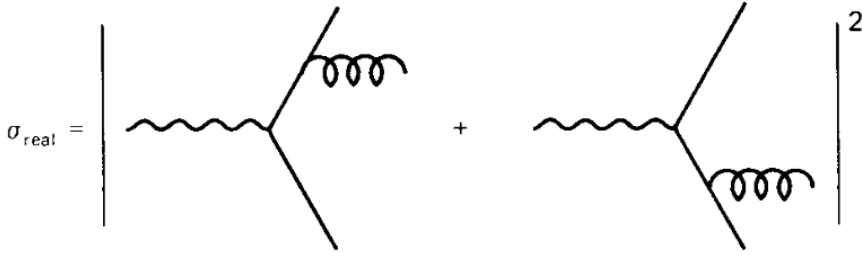


Figure 2.6: Representation of the first order real correction to the $\gamma \rightarrow q\bar{q}$. Now the phase space differs from the one in the process $\sigma(e^+e^- \rightarrow q\bar{q})$, due to the extra parton in the final state. This process $\sigma(e^+e^- \rightarrow q\bar{q}g)$ will reduce to the $\sigma(e^+e^- \rightarrow q\bar{q})$ in the IR limit, when the radiated gluon is either infinitely soft or collinear.

left-hand side over all of phase space, while retaining a finite total cross section,

$$\begin{aligned} \sigma_0^{\text{NLO}} &= \int d\Phi_0 |\mathcal{M}_0^{(0)}|^2 + \int d\Phi_1 |\mathcal{M}_1^{(0)}|^2 + \int d\Phi_0 2\text{Re}[\mathcal{M}_0^{(1)} \mathcal{M}_0^{(0)*}] \\ &= \sigma_0^{(0)} + \sigma_1^{(0)} + \sigma_0^{(1)}, \end{aligned} \quad (2.11)$$

with $\sigma_0^{(0)}$ the finite Born-level cross section, and the positive divergence caused by integrating the second term over all phase space is canceled by a negative one coming from the integration over loop momenta in the third term. One method for arranging the cancellation of singularities - the subtraction method - is discussed below.

As a particular example, we describe here the first order corrections to e^+e^- annihilation into hadrons. The Born level cross section for a process of the form $e^+e^- \rightarrow q^+q^-$ is given by

$$\sigma(e^+e^- \rightarrow q^+q^-) = 3 \sum_q e_q^2 \sigma(e^+e^- \rightarrow \mu^+\mu^-), \quad (2.12)$$

with the same structure than the cross section for a e^+e^- annihilation into a pair of leptons, with the difference over the fractional charges each pair of quarks could carry. Also, the factor 3 refers to the number of color, as described in Section 1.1, referring to how many quark pairs can we pick with colour-anticolour, to form a colour singlet. It is usually expressed directly in term of the R ration,

$$R = \frac{\sigma(e^+e^- \rightarrow \text{hadrons})}{\sigma(e^+e^- \rightarrow \mu^+\mu^-)} = 3 \sum_q e_q^2, \quad (2.13)$$

The order α_s corrections to R will come from the possibility of radiating a gluon from q or \bar{q} . The integrand we obtain is given by

$$\frac{1}{\sigma} \frac{d\sigma}{dx_q dx_{\bar{q}}} = \frac{2\alpha_s}{3\pi} \frac{x_q^2 + x_{\bar{q}}^2}{(1-x_q)(1-x_{\bar{q}})}, \quad (2.14)$$

We immediately notice that, when integrating over x_q and $x_{\bar{q}}$ from 0 to 1, we will find a divergence as x_q or $x_{\bar{q}}$ go to 1. To trace the origin of the problem, consider for instance

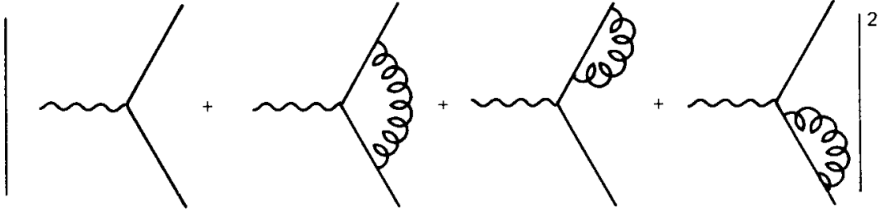


Figure 2.7: Representation of the first order virtual corrections to the $\gamma \rightarrow q\bar{q}$. The kinematics are the same than $\sigma(e^+e^- \rightarrow q\bar{q})$ Born level, given the loop nature of the radiated gluon.

the factor $1 - x_q$ in the denominator,

$$\begin{aligned} 1 - x_q &= \frac{s}{Q^2} = \frac{2\mathbf{p}_{\bar{q}} \cdot \mathbf{p}_g}{Q^2} \\ &= \frac{2}{Q^2} E_{\bar{q}} E_g (1 - \theta_{\bar{q}g}). \end{aligned} \quad (2.15)$$

We see that the factor $1 - x_q$ vanishes either when $E_g \rightarrow 0$, meaning the radiated gluon is *soft*, or when the angle $\theta_{\bar{q}g}$ goes to 0, i.e., \bar{q} and g become *collinear*. Now we must regularize these infrared singularities. One way to accomplish this is to give a fictitious mass m_g to the gluon and repeat the calculation from the Feynman diagrams. For the real radiation contribution depicted in Figure 2.6, we will have

$$\begin{aligned} \sigma^{\text{real}} &= \int dx_q dx_{\bar{q}} \frac{d\sigma}{dx_q dx_{\bar{q}}} \\ &= \sigma^{(0)} \frac{\alpha_s}{2\pi} \frac{4}{3} \left\{ \log^2 \left(\frac{m_q}{Q} \right) + 3 \log \left(\frac{m_q}{Q} \right) - \frac{\pi^2}{3} + 5 \right\}, \end{aligned} \quad (2.16)$$

which remains divergent when $m_g \rightarrow 0$. The key point is to realize that this can not be the final answer, since it depends on the fictitious mass m_q , or in the regulator ε if we had used dimensional regularization.

As we already know, there is *another* $\mathcal{O}(\alpha_s)$ contribution, coming from the Born-virtual interference term in Figure 2.7. The solution for this term, for which we are back to the Born kinematics, gives the solution

$$\sigma^{\text{virtual}} = \sigma^{(0)} \frac{\alpha_s}{2\pi} \frac{4}{3} \left\{ -\log^2 \left(\frac{m_q}{Q} \right) - 3 \log \left(\frac{m_q}{Q} \right) + \frac{\pi^2}{3} - 5 \right\}. \quad (2.17)$$

We can already see the perfect match between the two contributions, with opposite signs that will cancel the divergent and regulator-dependent terms. Although formally they live in different regions of the phase space, is precisely in the limit where the gluon in Figure 2.7 is soft or collinear when the phase space becomes also Born-like, and both contributions can be exactly canceled to give

$$\sigma = \sigma^{\text{real}} + \sigma^{\text{virtual}} = \sigma^{(0)} \frac{\alpha_s}{Q^2}, \quad (2.18)$$

which is finite and independent of regulator m_g , as indeed it must be. These particular case is a clear example of the general KLN theorem, and leads to the famous result for

the R ratio in e^+e^- annihilation at order α_s

$$R = 3 \sum_q e_q^2 \left\{ 1 + \frac{\alpha_s(Q^2)}{\pi} \right\}. \quad (2.19)$$

For a typical Q^2 where $\alpha_s \sim 0.2$, this correction is small and can not easily be distinguished and requires fine measurement techniques. This is indeed another example of a scaling parton model result being modified by $\log Q^2$ corrections arising from gluon radiation.

2.4 Exclusive final states - the subtraction idea

As stated by the KLN theorem, the IR singularities coming from integrating over soft and collinear real emission configurations should cancel order by order, against those coming from the IR divergent loop integrals. This implies that we should be able to rewrite a higher order cross section, e.g. an NLO cross section, as

$$\sigma^{\text{NLO}} = \sigma^{\text{Born}} + \text{Finite} \left\{ \int d\Phi_{F+1} |\mathcal{M}_{F+1}^{(0)}|^2 \right\} + \text{Finite} \left\{ \int d\Phi_F 2\text{Re}[\mathcal{M}_F^{(1)} \mathcal{M}_F^{(0)*}] \right\} \quad (2.20)$$

where the second and third terms have already gone through cancellation of their common - and opposite sign - singularities. Hence, the result that remains is perfectly finite.

The way this is achieved is by classifying the IR singularities, properly organized depending on how and in which order will they appear in the amplitudes, as we just discussed for the particular case of e^+e^- annihilation into $q\bar{q}$. We know that the IR limits are universal, hence they can be classified using a set of process-independent functions that only needs to be calculated once and for all. The commonly used in literature are the Catani-Seymour (CS) dipole ones [32, 33]. Here we will show as an example the antennae formalism [34, 35]. There are also other NLO techniques such as sector decomposition, hadroproduction of color states, etc, that are beyond the scope of this thesis. For more details see [36, 37].

For the case of NLO, the subtraction approach consists on rewriting the NLO cross section by adding and subtracting a simple function, $d\sigma_s$, that encapsulates all the IR singular limits.

$$\begin{aligned} \sigma^{\text{NLO}} = \sigma^{\text{Born}} &+ \int d\Phi_{F+1} (|\mathcal{M}_{F+1}^{(0)}|^2 - d\sigma_s^{\text{NLO}}) \\ &+ \int d\Phi_F 2\text{Re}[\mathcal{M}_F^{(1)} \mathcal{M}_F^{(0)*}] + \int d\Phi_{F+1} d\sigma_s^{\text{NLO}}. \end{aligned} \quad (2.21)$$

where the component $(|\mathcal{M}_{F+1}^{(0)}|^2 - d\sigma_s^{\text{NLO}})$ is finite by universality of the IR limit, and the sum of the second and third integrals is finite as stated by the KLN theorem. The task now is to construct a suitable form for $d\sigma_s$. A main requirement is that it should be sufficiently simple that the integral in the last term can be done analytically, in dimensional regularization, so that the IR poles it generates can be canceled against those from the loop.

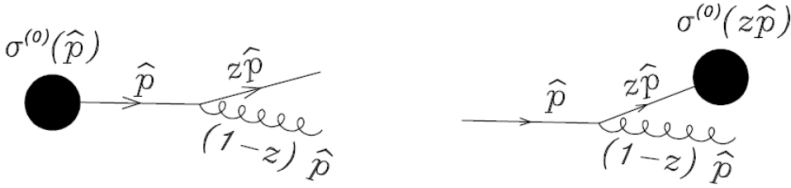


Figure 2.8: Single real gluon emission from a general process. A parton with momentum p splits into a gluon with fraction $(1 - z)p$, and the scaled parton remains with zp . On the left-hand side, radiation comes from the final state, as we dealt with in the example of α_s corrections to e^+e^- annihilation. On the right-hand side, the same radiation takes place before the hard interactions, and hence it will be described by initial state parton showers or directly by PDF evolution.

The way we proceed to parametrize the IR singularities on a given amplitude come from the observation that gauge theory amplitudes factorize in the soft limit as follows

$$|\mathcal{M}_{F+1}(\dots, i, j, k, \dots)|^2 \rightarrow g_s^2 N_C \left(\frac{2s_{ij}}{s_{ij}s_{jk}} + \frac{2m_i^2}{s_{ij}^2} - \frac{2m_k^2}{s_{ij}^2} \right) |\mathcal{M}_F(\dots, i, k, \dots)|^2 \quad (2.22)$$

where parton j is a soft gluon, partons i and k form a chain of color-space index contractions, g_s is the strong coupling, and the terms in parenthesis are called the *soft eikonal factor*. The mass corrections contribute only if i and k have non-zero rest masses, and the invariants s_{ab} are defined as

$$s_{ab} \equiv 2p_a \cdot 2p_b = (p_a + p_b)^2 - m_a^2 - m_b^2. \quad (2.23)$$

The color factor, N_C , is valid for the leading-color contribution, regardless of whether the i and k factors are quarks or gluons. Similarly, amplitudes also factorize in the *collinear limit*, with partons i and j parallel, so $s_{ij} \rightarrow 0$, in which the eikonal factor above is replaced by the DGLAP splitting kernels, which are already mentioned in the context of PDF evolution.

2.5 IR safety

An important requirement for perturbative QCD to be reliable is that the observable one aims to describe is *infrared safe*. By infrared, here we mean any limit that involves a small scale, i.e., any non-UV limit, without regard to whether it is collinear or soft. The property of infrared safety defines a special class of observables which have *minimal sensitivity* to long-distance physics, and which can be consistently computed in pQCD. An observable can be labeled as infrared safe if it does fulfill

- *Safety against soft radiation:* Adding any number of indefinitely soft particles should not change the value of the observable.
- *Safety against collinear radiation:* Splitting an existing particle up into two comoving particles, with arbitrary fractions z and $(1 - z)$ respectively of the original momentum, should not change the value of the observable.

Both cases can be seen in Figure 2.8, where the radiated gluon can be both soft and/or collinear. If both of these conditions are satisfied, any long-distance non-perturbative

corrections will be suppressed by the ratio of the long-distance scale to the short-distance to some power - process dependent - of the form

$$\text{IR safe observable} \implies \text{IR corrections} \propto \frac{Q_{IR}^2}{Q_{UV}^2} \quad (2.24)$$

where Q_{UV} denotes a generic hard scale, and $Q_{IR} \sim \Lambda_{QCD} \sim \mathcal{O}(1 \text{ GeV})$. Due to this power suppression, IR safe observables are not sensitive to our lack of ability to solve strongly coupled IR physics. Instead of the suppressed corrections above, the perturbative predictions for IR *sensitive* observables contain logarithms of the form already encountered in equation 2.9:

$$\text{IR sensitive observable} \implies \text{IR corrections} \propto \alpha_s^n \log^{m \leq 2n} \left(\frac{Q_{IR}^2}{Q_{UV}^2} \right), \quad (2.25)$$

which grow increasingly large as $Q_{IR}/Q_{UV} \rightarrow 0$. When dealing with exclusive final states, such as differential distributions with respect to some kinematic variables - and in particular with transverse momentum distributions - the logarithmic enhancements will require an all-order treatment, that we will describe in Chapter 4 introducing the resummation formalism.

Phenomenology at the LHC

This chapter is devoted to describe the phenomenology we encounter at the LHC and other collider experiments. First we will discuss some notations and nomenclature typically used in collider experiments, and then we will describe some of the most important processes used for studying the hadronic structure, such as the Deep Inelastic Scattering, the Drell-Yan lepton pair production, and finally the production of a Higgs boson at the LHC.

It is commonly stated that the Standard Model is extremely successful to date. Producing some of the most accurate predictions ever formulated by science, the Standard Model already contains in its description;

- Eight gluons and three generations of quarks, described by the $SU(3)$ gauge group, with their mixing angles described by the CKM matrix.
- Three generations of charged leptons and three generations of massive neutrinos¹ with their mixing angles described by the PMNS matrix².
- The photon and the massive W^\pm and Z bosons, described by the electroweak $SU(2)\times U(1)$ gauge group.
- A scalar Higgs boson, responsible for the breaking of the electroweak symmetry and hence for the generation of the mass hierarchies between the SM masses.

Along the LHC ring, we find four main experiments specialized in different kinds of processes and measurements: The ATLAS (A Toroidal LHC ApparatuS) and CMS (Compact Muon Solenoid) experiments, ALICE (A Large Ion Collider Experiment) and the LHCb (LHC beauty). The last two are devoted to the study of high-density hadron matter, such as quark-gluon plasma, and the so-called *flavour* physics through the study of B-hadrons and the phenomenon of CP-violation, respectively. ATLAS and CMS, conversely, are general purpose experiments, and their main goals were originally searching for the Higgs boson and for any kind of signals of new physics beyond the Standard

¹While the neutrinos were originally assumed to be massless, the measurement of flavour oscillation, analogous to the CKM mixing of quarks, requires neutrinos to have non-zero mass. Different models are still discussed to explain the nature of neutrinos masses, such as the Dirac and the Majorana mechanism, among others.

²Pontecorvo–Maki–Nakagawa–Sakata matrix (PMNS matrix), lepton mixing matrix, or neutrino mixing matrix is a unitary matrix describing the quantum states of neutrinos when they propagate freely and when they take part in the weak interactions. It states a model of neutrino oscillation, and it was introduced in 1962 by Ziro Maki, Masami Nakagawa and Shoichi Sakata to explain the neutrino oscillations predicted by Bruno Pontecorvo.

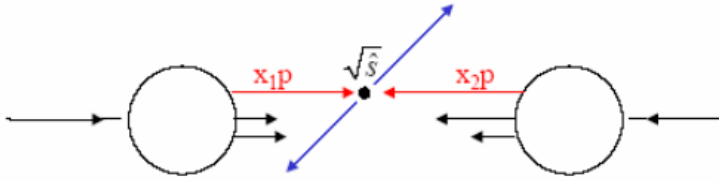


Figure 3.1: Representation of a collision at the LHC. From the two proton beams, partons with fraction of energy x_1 and x_2 interact at a partonic center of mass energy $\sqrt{\hat{s}} = (x_1 p_1 + x_2 p_2)^2$

Model (Supersymmetry (SUSY), extra-dimensions, dark matter signatures, etc). To be able to distinguish such hints of new physics beyond the Standard Model, it is crucial to have very accurate theoretical predictions of what is expected by the Standard Model, at least as accurate as precise the detection and measurement techniques, in order to be able to distinguish deviation from the expectations with the maximal significance.

When addressing scattering experiments, the most common quantity to measure is the so-called *cross section*, representing the likelihood for a particular process to take place. The cross section σ is a measurement of the probability that an event occurs. It is measured in barns $1b = 10^{-24}\text{cm}^2$. Then, the number of events for a particular process is given by

$$N_{\text{events/sec}} = \text{Luminosity} \cdot \text{cross section}$$

$$N_{\text{events/sec}} = \mathcal{L} \cdot \sigma_{\text{event}}$$

Those are the typical units used in phenomenology rather than seconds and square meters, since what we typically need is a few interesting events corresponding to a few femtobarns of data. So the typical signals usually have values of the cross sections and luminosity in the following orders of magnitude;

$$N_{\text{events}} = \mathcal{L} \cdot \sigma_{\text{tot}}$$

$$\mathcal{L} = 10 \dots 300 \text{ fb}^{-1}$$

$$\sigma_{\text{tot}} = 1 \dots 10^4 \text{ fb}$$

where fb stands for femto-barn ($1b^{-15}$). For instance, the total proton-proton cross section at 7 TeV is approximately 110 mbarns.

Let's see a couple of examples. The cross section for a hypothetical 350 GeV Higgs boson is 50 fb via the $qq \rightarrow ZH$ process. So we can easily see,

$$\sigma = 50 \cdot 10^{-15} \cdot 10^{-24} \text{cm}^2 \implies \sigma = 5 \cdot 10^{-38} \text{cm}^2$$

$$N_{\text{events/sec}} = \mathcal{L} \cdot \sigma_H = 10^{34} \text{cm}^{-2} \text{s}^{-1} \times 5 \cdot 10^{-38} \text{cm}^2 = 5 \cdot 10^{-4}$$

Therefore there are $5 \cdot 10^{-4}$ events per second in which this Higgs boson will be appearing (obviously, whether such a kind of Higgs boson exist). We can calculate the inverse of that quantity

$$t = 1/(5 \cdot 10^{-4}) = 2000 \text{ s} \implies t = 33 \text{ minutes}$$

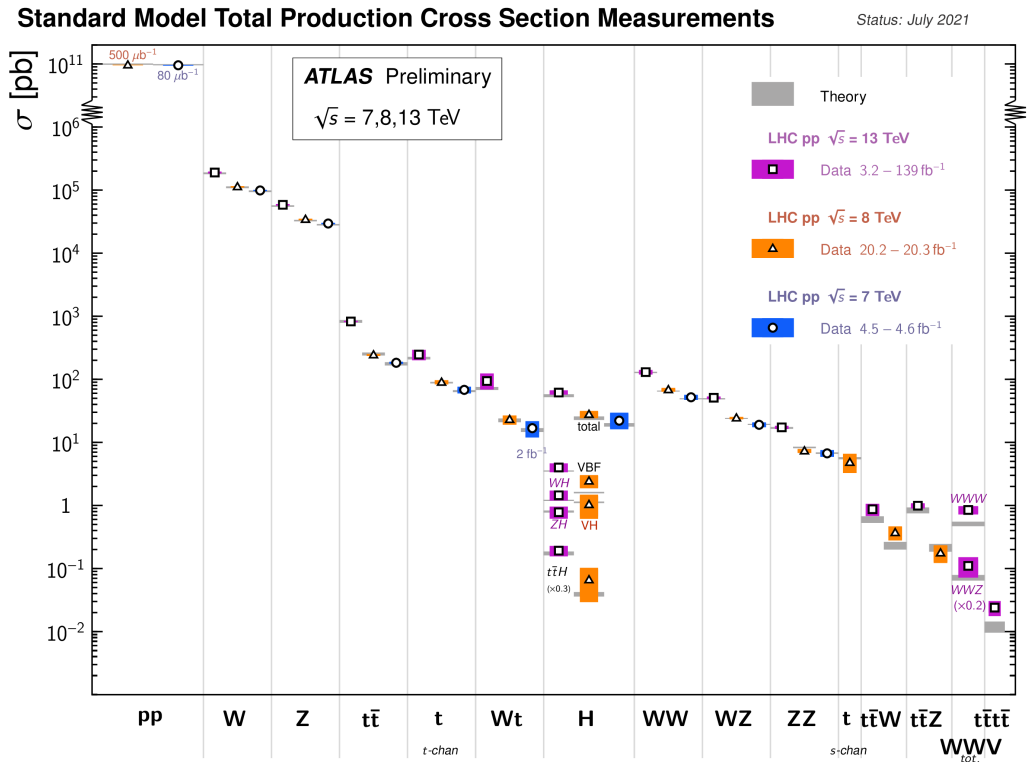


Figure 3.2: Cross sections for different processes at the LHC. As expected, processes for which more data is available have smaller statistical uncertainty, while the theory error remains even for such cases. Therefore, producing accurate predictions becomes a main task for theoreticians specially towards the high precision era of the LHC.

which means that every 33 minutes one Higgs boson excitation should be appearing. Therefore, in one day of work, around 50 Higgs particles should be detected. It could seem a lot, but thousands of billions of collisions will be produced in the detector in that time. That’s why the triggering and selection technologies are crucial for phenomenology analysis, to correctly discriminate between QCD background effects and the specific signal we are looking for. Again, the importance of precise predictions goes together with the fine measurement techniques.

Let’s see another example. The LHCb is the experiment dedicated to quark b physics at the LHC. Its primary goal is to look for indirect evidence of beyond the Standard Model physics in CP violation ³ and rare decays of hadrons which contains b and c quarks.

Compared to other existing accelerators that are in operation, the LHC is by far one

³The discovery of CP violation in the decays of neutral kaons resulted in the Nobel Prize in Physics in 1980 for its discoverers James Cronin and Val Fitch. Nowadays it plays an important role both in the attempts of cosmology to explain the dominance of matter over antimatter in the present universe, and in the study of weak interactions in particle physics.

of the most copious source of B mesons ⁴, due to the high $b\bar{b}$ cross section, which is of the order $\sigma \sim 500 \mu\text{b}$ at 14 TeV and Luminosity $2 \cdot 10^{32} \text{cm}^{-2} \text{s}^{-1}$, on average. So for the number of events we would have,

$$\begin{aligned} N_{\text{events/sec}} &= \mathcal{L} \cdot \sigma_{b\bar{b}} \\ &= 2 \cdot 10^{32} \text{cm}^{-2} \text{s}^{-1} \times 500 \cdot 10^{-6} \cdot 10^{-24} \text{cm}^2 = 10^5 \text{ } b\bar{b} \text{pairs/sec} , \end{aligned}$$

therefore in a canonical year data taking corresponds to 280 hours ($\sim 10^7$)s

$$10^5 \text{pairs/sec} \cdot 10^7 \text{sec/year} = 10^{12} \text{pairs/year} \quad (3.1)$$

An important thing to remark when dealing with collider physics, is that usually signals are much more rare than background events, therefore we have to extract and look for the signal events out a much larger number of background events. For instance, the production cross section of two bottom quarks at the LHC is larger than 10^5 nb or 10^{11} fb , while the typical production cross section for W and Z boson ranges around 200 nb or $2 \cdot 10^8 \text{ fm}$. Looking at more signals, the production cross sections for a pair of 500 GeV gluinos is $4 \cdot 10^4 \text{ fb}$ and the Higgs production cross section lies around the 10^5 fb .

Therefore, if we want to extract such signals out of comparably huge backgrounds we need to describe these backgrounds with incredible precision. Strictly speaking, this holds at least for those background events which populate the signal region in phase space. Such background event will always exist, so any LHC measurement will always be a statistics exercise. The high energy community has therefore agreed that we call a five sigma excess over the known backgrounds a *signal* or *discovery*, while a three sigma excess can only mean an *evidence*.

$$\frac{S}{\sqrt{B}} = N_\sigma > 5 \quad \text{Discovery - Gaussian limit} \quad (3.2)$$

Hence, it is commonly said that three sigma is an evidence, but we need five sigma to say discovery. This brings us to the importance of precise predictions and measurements when searching for new physics. Since both signal and background events are mainly described by QCD, we need to understand where our predictions come from and what they assume.

3.1 Deep Inelastic Scattering

In order to explore the internal structure of the hadrons, one of the first processes that were studied, and indeed one for which the parton model was originally formulated, is the lepton-hadron scattering, through the so-called Deep Inelastic Scattering (DIS).

Given the simple kinematics they involve, DIS processes have played, and still play, a very important role in our understanding of both QCD and the nucleon structure. We will concentrate on the case of a charged lepton, as the one depicted in Figure 3.3. The process is called inelastic because the energy of the interaction is such that it breaks the

⁴There exist also collider experiments known as B-factories, such as SuperB (Rome, Italy), BaBar (Stanford, USA), and Belle II (Tsukuba, Japan), are specialized in B-meson physics.

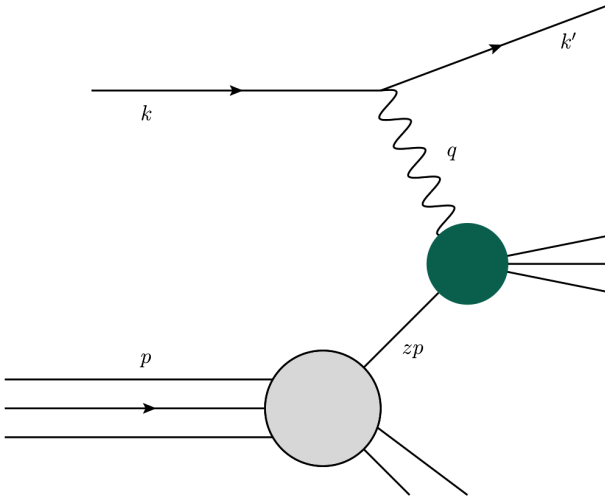


Figure 3.3: Representation of a Deep Inelastic Scattering (DIS) process, where a lepton with momentum k scatters with a hadron of momentum p . The hard interaction, represented by the green blob, takes place between a highly virtual photon of momentum q , and the partons inside the hadron. Perturbative QCD is here applied to calculate higher corrections such as virtual and real emissions.

proton structure, leading to an arbitrary number of particles - such as other hadrons - in the final state. We can write the amplitude for the process as

$$\mathcal{M} = e \bar{u}(k') \gamma^\mu u(k) \mathcal{P}_\mu(p, q), \quad (3.3)$$

where $\mathcal{P}_\mu(p, q)$ includes the information about the hard part of the process, including the photon propagator. The amplitude squared, after sum over final states and averaged over the initial ones, can be written as

$$\frac{1}{N} \sum_{i,j} |\mathcal{M}|^2 = L_{\mu\nu} W^{\mu\nu}, \quad (3.4)$$

where $L_{\mu\nu}$ and $W^{\mu\nu}$ are tensors containing the leptonic and hadronic part of the interaction, respectively. They are usually directly referred to as leptonic and hadronic tensors. The former one can be simply written as

$$L_{\mu\nu} = e^2 \text{Tr}\{k' \gamma_\mu k \gamma_\nu\}, \quad (3.5)$$

while the $W^{\mu\nu}$ contains all the information about the hadronic process. We will now skip some part of the computations, presenting directly some results for fixing notations that will be useful later in the thesis, while a complete review can be found in [3].

The final result for the cross section can be written as

$$\frac{d\sigma}{dx dQ^2} = \frac{4\pi\alpha_s}{Q^2} \left\{ (1 + (1-y)^2) F_1(x, Q^2) + \frac{1-y}{x} (F_2(x, Q^2) - 2xF_1(x, Q^2)) \right\}, \quad (3.6)$$

where we have defined the kinematic invariants

$$x = \frac{Q^2}{2pq}, \quad y = \frac{qp}{kp}, \quad Q^2 = -q^2 \quad (3.7)$$

with $Q^2 = -q^2$ defined such that we have a positive virtuality, and we have introduced the so-called *structure functions* F_1 and F_2 . After reading Chapter 1 one can already relate those functions with the parton densities, but here we will try to give an intuition of the information they encode simply from the kinematic of the DIS.

Note that this results is much older than QCD, at least much older than the time at which it was completely formulated. Indeed, we have not stated anything so far about the structure of the hadronic interaction, absorbing any hadronic information inside the structure functions, which should be measured experimentally. It is sometimes useful to introduce the longitudinal structure function

$$F_L(x, Q^2) = F_2(x, Q^2) - 2xF_1(x, Q^2) . \quad (3.8)$$

The intuition behind this function, as we can inherit from 3.6 is that it corresponds to the absorption of a longitudinally polarized virtual photon, while the $F_1(x, Q^2)$ corresponds to the absorption of a transversely polarize photon. Since the quarks have fractional spin 1/2, they can not absorb longitudinal photons, and they would lead to a vanishing F_L (Callan-Gross relation, [38]). Indeed, this is observed in the limit of an infinitely virtual photon, with $Q^2 \rightarrow \infty$ at fixed x , the so-called Bjorken limit[19, 39], and hence confirming the spin 1/2 nature of quarks.

The structure functions follow from the hadronic tensor, that can be computed within the Parton Model framework. We can write

$$F_i(x, Q^2) = x \sum_j \int_x^1 \frac{dz}{z} f_j(z) C_{ij}^{(0)}\left(\frac{x}{z}\right) , \quad (3.9)$$

where the function $C_{ij}^{(0)}$ are called the *coefficient functions*. The superscript (0) indicates that we strictly remain in the Parton Model, and do not add higher order QCD corrections. Therefore, in the "naive" Parton Model, choosing F_2 and F_L as the two independent structure functions, we have

$$\begin{aligned} C_{2q}^{(0)}(z) &= e_q^2 \delta(1-z) & C_{2g}^{(0)}(z) &= 0 \\ C_{Lq}^{(0)}(z) &= 0 & C_{Lg}^{(0)}(z) &= 0 \end{aligned} \quad (3.10)$$

where e_q is the quark fractional charge. Then the structure functions are

$$F_2(x, Q^2) = x \sum_q e_q^2 f_q(x), \quad F_L(x, Q^2) = 0 , \quad (3.11)$$

where we see no dependence on Q^2 . This is known as *Bjorken scaling*, and we already know that it will be violated when adding higher order QCD corrections, as the ones coming from gluon emission. There are several structure functions $F_i(x, Q^2)$ that can be studied, each function of two variables. Depending on the charges of l and l' , the pair of particles going through the hard interaction, we can have neutral currents, such as γ, Z , or charged currents such as W^\pm . In the past years, DIS processes have been crucial for establishing QCD as theory of strong interactions and quarks and gluons as QCD partons.

As a final note, let us introduce one of the key mathematical tools used in pQCD. One should recall that equation 3.9 has the form of a Mellin convolution

$$(g * h)(x) = \int_z^1 \frac{dz}{z} g(z) h\left(\frac{x}{z}\right), \quad (3.12)$$

which is symmetric under the interchange of arguments $z \rightarrow x/z$. The Mellin convolution diagonalizes under a Mellin transform

$$\mathbb{M}[g(z)] = \tilde{g}(N) = \int_0^1 dz z^{N-1} g(z), \quad (3.13)$$

meaning that a convolution in direct space becomes a simple product in Mellin space, leading to much simpler expressions to manipulate. These convolutions will drastically simplify as

$$\mathbb{M}[g * h](N) = \tilde{g}(N) \tilde{h}(N). \quad (3.14)$$

The inverse Mellin transform is given by

$$\mathbb{M}^{-1}[\tilde{g}(N)] = \frac{1}{2\pi i} \int_{c-i\infty}^{c+i\infty} dN x^{N-1} g(z), \quad (3.15)$$

where c has to be to the right of the rightmost singularity of $\tilde{g}(N)$, which always exists since a Mellin (Laplace) transformation has always a convergent abscissa. The Mellin transformation is related to the Laplace transformation by a simple change of variables. Details on integral transforms and special functions can be found at the end of this thesis in Appendix A.

At present DIS remains very important for quantitative studies and tests of QCD. The theory of scaling violations for totally inclusive DIS structure functions, based on operator expansion or diagrammatic techniques and renormalization group methods, was able to predict the Q^2 dependence that was later on measured at each value of x . The measurement of quark and gluon parton densities in the nucleon, as functions of x at some reference value Q^2 , which is an essential starting point for the calculation of all relevant hadronic processes, was first performed in DIS processes. At the same time one measures $\alpha_s(Q^2)$, and the DIS values of the running coupling can be compared with those obtained from other processes.

3.2 The Drell-Yan process

In this section we describe a next-to-simplest example of a hadronic interaction with respect to the DIS, involving now two hadrons in the initial state. The Drell-Yan lepton pair production, or Drell-Yan for short, is theoretically computable and experimentally measurable with the highest accuracy at hadron colliders, in particular at the LHC. As it is shown in Figure 3.4, it consists in the production of a neutral or charged lepton pair, such as $l\bar{l}$ or $l\bar{\nu}$, arising from the collision of two initial hadrons h_1 and h_2

$$h_1(p_1) + h_2(p_2) \rightarrow l(k_1) + \bar{l}(k_2) + X \quad (3.16)$$

in the case of neutral current, and

$$h_1(p_1) + h_2(p_2) \rightarrow l(k_1) + \bar{\nu}(k_2) + X \quad (3.17)$$

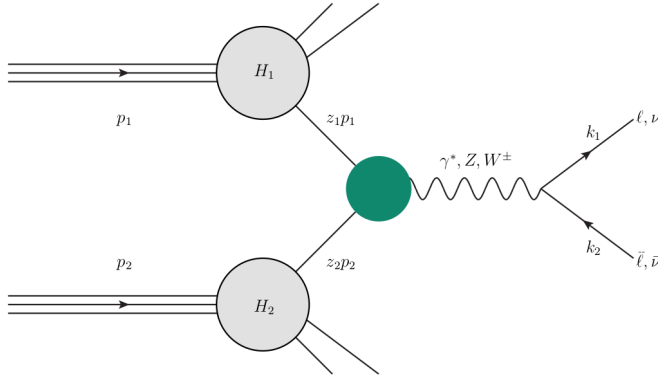


Figure 3.4: Representation of a Drell-Yan lepton pair production process. Two partons scatter from the hadrons h_1 and h_2 with respective momenta $z_1 p_1$ and $z_2 p_2$, and undergo the hard interaction to produce a virtual vector boson. The product of the interaction will eventually decay in a lepton pair with energies k_1 and k_2 , that will be measured in the detector.

for a charged one. In both cases the kinematics are the same, and X is the entire set of other particles produced in the event. The large set of events collected at the LHC, combined with a very precise theoretical determination of the process, can build a very powerful test for perturbative QCD. Indeed, the high precision era of the LHC will allow for detailed measurements at previously unexplored kinematic domains, significantly improving the precision on, for instance, the determination of the PDFs.

The cross section can be computed at leading order, both in the electroweak and QCD coupling, as the cross section for quark-antiquark annihilation into a virtual photon or a virtual vector boson Z, W^\pm , which subsequently decays into the lepton pair. Hence the partonic centre-of-mass energy is given by

$$\hat{s} = x_1 x_2 s \quad s = (p_1 + p_2)^2, \quad (3.18)$$

where x_1 and x_2 are the momentum fractions of the two incoming partons. The available energy is encoded in the lepton pair invariant mass M

$$M^2 = (k_1 + k_2)^2, \quad (3.19)$$

and the inclusive cross section is characterized by the variable

$$\tau = \frac{M^2}{s}, \quad (3.20)$$

which describes the amount of initial hadronic energy going into the relevant final state, actually the lepton pair. Again, if we start from the naive Parton Model and we include higher order QCD corrections, real emission of gluons and quarks must be taken under consideration, in order to cancel the infrared divergences coming from virtual emission. In this case, the available partonic centre-of-mass energy is no longer equal to the mass of the final state. It will be instead given by the variable

$$z = \frac{M^2}{\hat{s}} = \frac{\tau}{z_1 z_2}, \quad (3.21)$$

which is the partonic analogous to τ , and it is indeed common to find it as $\hat{\tau}$ in the literature. The Born amplitude and its virtual corrections select $z \rightarrow 1$, while in the case of real emissions we have $0 \leq z \leq 1$. As discussed in section 2.3, in such exclusive cases the coefficient function comes enhanced by logarithmic terms of the form $\log(1-z)$, which in the soft limit $z \rightarrow 1$ require all-orders threshold resummation to have reliable predictions⁵.

NNLO inclusive cross sections and rapidity distributions have already been computed long ago. Results for both the integrated cross section can be found in [40], and for rapidity distributions in [41]. Also, small effects such as those related to the coupling of the gauge boson to final-state leptons have been studied recently [42]. There are already some results for N³LO distributions, but we will introduce them after discussing the resummation formalism, in the context of N³LL predictions.

We briefly describe here the LO and NLO expressions for rapidity distributions and inclusive cross sections. The rapidity distribution is written as

$$\frac{1}{\tau} \frac{d\sigma}{dM^2 dy} = \sum_{i,j} \int_{\tau}^1 \frac{dz}{z} \int_0^1 du \mathcal{L}_{ij}(z, u, \mu_F^2) \bar{C}_{ij} \left(z, u, \alpha_s(\mu_R^2), \frac{M^2}{\mu_F^2}, \frac{M^2}{\mu_R^2} \right), \quad (3.22)$$

where y is the hadronic rapidity, \mathcal{L}_{ij} is the parton luminosity and \bar{C}_{ij} is a coefficient function representing the partonic channels. At NLO, the rapidity distribution receives contributions from quark-antiquark and quark-gluon subprocesses

$$\frac{d\sigma^{\text{NLO}}}{dM^2 dy} = \frac{d\sigma_{q\bar{q}}^{\text{NLO}}}{dM^2 dy} + \frac{d\sigma_{qg+gq}^{\text{NLO}}}{dM^2 dy}, \quad (3.23)$$

The $q\bar{q}$ contribution is given by

$$\bar{C}_{q\bar{q}} \left(z, u, \alpha_s(\mu_R^2), \frac{M^2}{\mu_F^2}, \frac{M^2}{\mu_R^2} \right) = \delta(1-z) + \frac{\alpha_s}{\pi} C_F F_q \left(z, u, \frac{M^2}{\mu_F^2} \right) + \mathcal{O}(\alpha_s^2) \quad (3.24)$$

where the structure function F_q is given by

$$\begin{aligned} F_q \left(z, u, \frac{M^2}{\mu_F^2} \right) &= \frac{\delta(u) + \delta(1-u)}{2} \left[\delta(1-z) \left(\frac{\pi^2}{3} - 4 \right) + 2(1+z^2) \left(\frac{\log(1-z)}{1-z} \right)_+ \right. \\ &\quad \left. + \log \frac{M^2}{\mu_F^2} \left(\frac{1+z^2}{1-z} \right)_+ - \frac{1+z^2}{1-z} \log z + 1 - z \right] \\ &\quad + \frac{1}{2} \frac{1+z^2}{1-z} \left[\left(\frac{1}{u} \right)_+ + \left(\frac{1}{1-u} \right)_+ \right] - (1-z). \end{aligned} \quad (3.25)$$

The qg and gq contributions are given by

$$\bar{C}_{qg} \left(z, u, \alpha_s(\mu_R^2), \frac{M^2}{\mu_F^2}, \frac{M^2}{\mu_R^2} \right) = \frac{\alpha_s}{2\pi} T_F F_g \left(z, u, \frac{M^2}{\mu_F^2} \right) + \mathcal{O}(\alpha_s^2) \quad (3.26)$$

$$\bar{C}_{gq} \left(z, u, \alpha_s(\mu_R^2), \frac{M^2}{\mu_F^2}, \frac{M^2}{\mu_R^2} \right) = \frac{\alpha_s}{2\pi} T_F F_g \left(z, 1-u, \frac{M^2}{\mu_F^2} \right) + \mathcal{O}(\alpha_s^2) \quad (3.27)$$

⁵Note that in Chapter 2 we described another kind of logarithmic corrections, of the form $\log(M^2/q_T^2)$. Hence, it is referred to talk about *transverse momentum resummation*. There exist also high energy resummation, or *BFKL resummation*, which is beyond the scope of this thesis and that we will not discuss.

where the F_g is now given by

$$F_g\left(z, u, \frac{M^2}{\mu_F^2}\right) = \delta(u) \left[(z^2 + (1-z)^2) \left(\log \frac{(1-z)^2}{z} + \log \frac{M^2}{\mu_F^2} \right) + 2z(1-z) \right] \\ + (z^2 + (1-z)^2) \left(\frac{1}{u} \right)_+ - 2z(1-z) + (1-z)^2 u. \quad (3.28)$$

Now we see how the differential distribution can be written in terms of the \bar{C}_{ij} coefficients, which is computable in perturbation theory. The structure functions F_q and F_g contain the singularities that appear in the form of plus distributions⁶. This process, among those quadratic in parton densities with a totally inclusive final state, is perhaps the simplest one from a theoretical point of view. The large scale is specified and measured by the invariant mass squared M^2 of the lepton pair, which is not itself strongly interacting, so there are no hadronization effects.

Over the years the QCD predictions for W and Z production, a better testing ground than the older fixed-target-DIS experiments, have been compared with experiments at CERN $Spp\bar{S}$ and Tevatron energies and now at the LHC. $M \sim M_{W,Z}$ is large enough to make the prediction reliable (with a not too large K-factor) and the ratio $\sqrt{\tau} = M/\sqrt{s}$ is not too small. Results of current experiments are in fair agreement with the SM predictions (see summary in [GA285] and references therein), and typical precision is comparable to or better than the size of NLO corrections.

The calculation of the W/Z q_T distribution is a classic challenge in QCD. For large q_T , for instance $q_T \sim O(M_W)$, the q_T distribution can be reliably computed in perturbation theory. This was done up to NLO in the late 1970s and early 1980s [GA183]. As we will discuss in next chapter, a problem arises in the intermediate range $\Lambda_{QCD} \ll q_T \ll M_W$, where the bulk of data is concentrated, because terms of order

$$\alpha_s(q_T^2) \log \left(\frac{M_W^2}{q_T^2} \right) \quad (3.29)$$

become of order 1 and should be resummed to all orders, within the formalism of transverse momentum resummation.

3.3 SM Higgs boson production

Higgs boson production is nowadays a topic of central importance in hadron collider physics [43, 44, 45]. The main production mechanism at hadron colliders is the gluon fusion process, an essentially strong-interaction process, which has attracted a great amount of theoretical work in recent years [46, 47, 48].

Again, we will present some results that should serve as a summary and to fix notations, without digging in to the formalism with much detail. For a proper review on the Higgs boson production at the LHC one can check [44], among others in literature, or see Appendix B. If we consider the scalar part of the Standard Model Lagrangian

$$\mathcal{L}_H = (D^\mu \Phi)^\dagger (D_\mu \Phi) - \mu^2 \Phi^\dagger \Phi - \lambda (\Phi^\dagger \Phi)^2 \quad (3.30)$$

⁶The plus distributions are described in detail, both mathematical and the intuition in appendix A

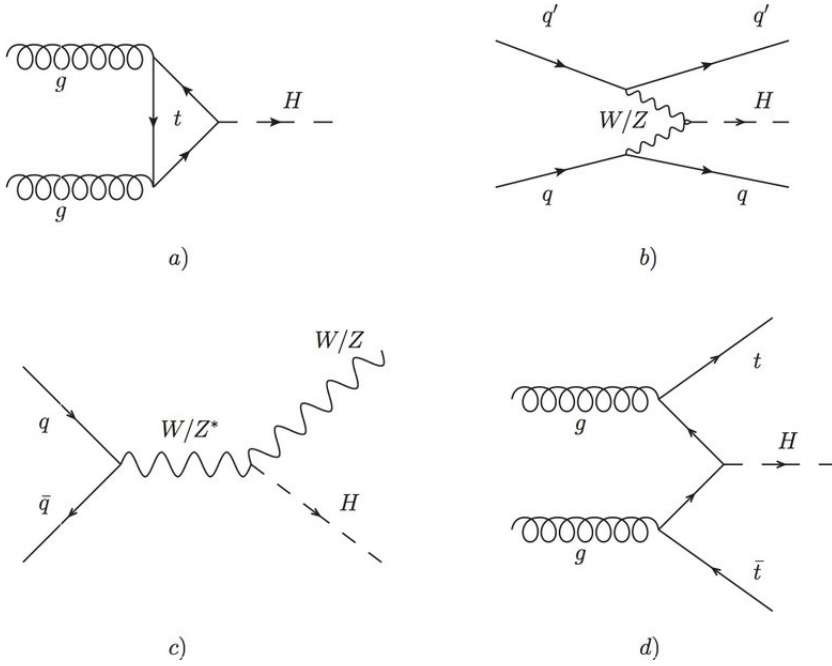


Figure 3.5: Feynman diagram representation of the dominant production channels for the Higgs boson at the LHC. The kinematics are the same as in the Drell-Yan process depicted in Figure 3.4.

we see that the kinetic term for the Higgs field $\frac{1}{2}(\partial_\mu H)^2$ comes from the term involving the covariant derivative $|D_\mu \Phi|^2$, while the mass and self-interacting parts arise from the scalar potential

$$V(\Phi) = \mu^2 \Phi^\dagger \Phi + \lambda (\Phi^\dagger \Phi)^2. \quad (3.31)$$

The electroweak symmetry is broken by an SU(2)-doublet scalar field

$$\Phi = \begin{pmatrix} G^+ \\ (H + v)/\sqrt{2} + iG^0/\sqrt{2} \end{pmatrix}, \quad (3.32)$$

where G^+ and G^0 are the Goldstone bosons that eventually become the longitudinal degrees of freedom of the W^+ and the Z . The quantity v is the Higgs vacuum expectation value (vev), and H is the physical SM Higgs boson. When the electroweak symmetry is broken, meaning the neutral component of Φ takes the expectation value

$$\langle 0 | \Phi | 0 \rangle = \begin{pmatrix} 0 \\ \frac{v}{\sqrt{2}} \end{pmatrix} \text{ being } v = \left(-\frac{\mu^2}{\lambda} \right)^{1/2} \quad (3.33)$$

we can make a gauge transformation

$$\Phi(x) \rightarrow \frac{1}{\sqrt{2}} \begin{pmatrix} 0 \\ v + H(x) \end{pmatrix} \quad (3.34)$$

so the potential takes the form

$$V = \frac{\mu^2}{2} (0, v + H) \begin{pmatrix} 0 \\ (v + H) \end{pmatrix} + \frac{\lambda}{4} \left| (0, v + H) \begin{pmatrix} 0 \\ (v + H) \end{pmatrix} \right|^2, \quad (3.35)$$

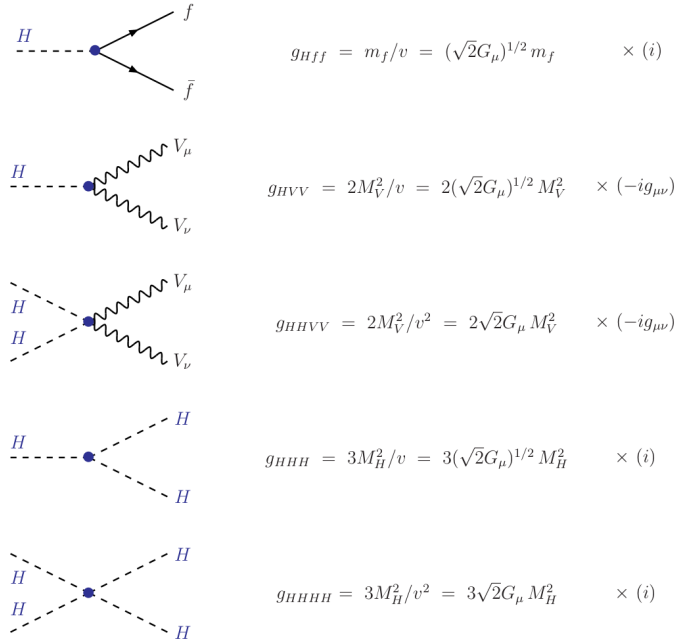


Figure 3.6: Higgs boson couplings to fermions and gauge bosons and the Higgs self-couplings in the Standard Model. The normalization factors of the Feynman rules are also displayed.

where we can use the relation $v = -\mu^2/\lambda$ to write

$$V = -\frac{1}{2}\lambda v^2(v + H)^2 + \frac{1}{4}\lambda(v + H)^4 \quad (3.36)$$

and find that the Lagrangian containing the Higgs field H is given by

$$\begin{aligned} \mathcal{L}_H &= \frac{1}{2}(\partial_\mu H)(\partial^\mu H) - V \\ &= \frac{1}{2}(\partial_\mu H)^2 - \lambda v^2 H^2 - \lambda v H^3 - \frac{\lambda}{4}H^4. \end{aligned} \quad (3.37)$$

From this Lagrangian one can see that the Higgs boson mass directly reads

$$M_H^2 = 2\lambda v^2 = -2\mu^2. \quad (3.38)$$

The Feynman rules for Higgs self-interaction and for the coupling to fermions can be found in Appendix B. The numerical value of the Higgs vev is fixed in terms of the W mass and the Fermi constant

$$v = 2M_W/g \simeq 246 \text{ GeV}, \quad (3.39)$$

such that the couplings of the physical Higgs boson to other SM particles are predicted entirely in terms of v and the known particles masses via the usual SM Higgs mass generation mechanism.

The total cross section for the Higgs boson production in gluon fusion has been computed in QCD perturbation theory at leading order (LO), $\mathcal{O}(\alpha_s)$, next-to-leading order (NLO), next-to-next-to-leading order (NNLO) and next-to-next-to-next ($\mathbb{N}^3\text{LO}$) in the QCD coupling α_s . The origin of the dominant perturbative contributions to the total cross section comes from radiative corrections due to virtual and soft gluons.

The $\mathcal{O}(\alpha_s)$ corrections to the Higgs boson cross section

As previously mentioned, the dominant production channel for the Higgs boson at the LHC is through a top quark loop arising from gluon fusion, as shown in Figure 3.5. In the large M_t limit, the top quark can be replaced by a point-like vertex, leaving an effective Higgs-gluon coupling in terms of the Lagrangian of the effective theory

$$\mathcal{L}_{\text{eff}} = -\frac{1}{4} \left[1 - \frac{\alpha_s}{3\pi} \frac{H}{v} \left(1 + \frac{\alpha_s}{4\pi} \Delta \right) \right] G_{\mu\nu}^a G_a^{\mu\nu}, \quad (3.40)$$

where the finite $\mathcal{O}(\alpha_s)$ order correction to the effective Hgg operator Δ is

$$\Delta = 5N_c - 3C_F = 11, \quad (3.41)$$

being $N_c = 3$ and $C_F = (N_c^2 - 1)/(2N_c) = 4/3$. For the $\mathcal{O}(\alpha_s^2)$ corrections to this effective operator see [49]. The general form of the Higgs self-coupling and the coupling to fermions is depicted in Figure 3.6.

We consider the scattering of two hadrons, with exact same kinematics as in the Drell-Yan case depicted in Figure 3.4, now producing a neutral Higgs boson $h_1 + h_2 \rightarrow H + X$. Following the factorization formula we discussed in Chapter 2, the differential cross section for this process via gluon-gluon fusion in perturbative QCD can be written

$$\frac{d\sigma}{dq_T^2 dy_H} = \sum_{i,j} \int_0^1 dx_a dx_b f_{i/h_1}(x_a, \mu_F^2) f_{j/h_2}(x_b, \mu_F^2) \frac{d\hat{\sigma}_{ij}}{dq_T^2 dy_H}, \quad (3.42)$$

being i and j the labels for the massless partons which scatter from the hadrons h_1 and h_2 . The partonic subprocess can be expanded as a power series of the strong coupling $\alpha_s(\mu_R^2)$ as

$$\frac{d\hat{\sigma}_{ij}}{dq_T^2 dy_H} = \frac{\sigma^{(0)}}{\hat{s}} \left[\frac{\alpha_s(\mu_R^2)}{2\pi} G_{ij}^{(1)} + \left(\frac{\alpha_s(\mu_R^2)}{2\pi} G_{ij}^{(2)} \right)^2 + \dots \right], \quad (3.43)$$

with $\sigma^{(0)}$ the Born-level cross section

$$\sigma^{(0)} = \frac{\pi}{64} \left(\frac{\alpha_s(\mu_R^2)}{3\pi v} \right)^2, \quad (3.44)$$

where the Higgs vacuum expectation value v is related to the Fermi constant $G_F = 1.16639 \cdot 10^{-5} \text{ GeV}^{-2}$ by $1/v^2 = \sqrt{2}G_F$. The functions $G_{ij}^{(k)}$ depend on μ_R and μ_F , the Higgs mass M_H and the partonic Mandelstam invariants, defined by

$$\begin{aligned} \hat{s} &= (p_a + p_b)^2 = (p_H + Q)^2 = x_a x_b s \\ \hat{t} &= (p_a - Q)^2 = (p_b + p_H)^2 = M_H^2 - \sqrt{s} x_b m_T e^{y_H} \\ \hat{u} &= (p_b + Q)^2 = (p_a - p_H)^2 = M_H^2 - \sqrt{s} x_a m_T e^{-y_H}, \end{aligned} \quad (3.45)$$

where $p_a = x_a p_1$ and $p_b = x_b p_2$ are the initial-state parton momenta, Q is the momentum of the final-state partons balancing the Higgs boson, and m_T^2 the transverse mass $m_T^2 = M_H^2 + q_T^2$. These invariants are related by

$$Q^2 = \hat{s} + \hat{t} + \hat{u} - M_H^2. \quad (3.46)$$

At leading order the contributions arising from the different subprocesses are given by $G_{ij}^{(1)} = g_{ij} \delta(Q^2)$ with

$$\begin{aligned} g_{gg} &= N_c \left(\frac{M_H^8 + \hat{s}^4 + \hat{t}^4 + \hat{u}^4}{\hat{s}\hat{t}\hat{u}} \right) \\ g_{gq} &= N_c \left(\frac{\hat{t}^2 + \hat{u}^2}{-\hat{u}} \right) \\ g_{qg} &= N_c \left(\frac{\hat{t}^2 + \hat{u}^2}{\hat{s}} \right) \end{aligned} \quad (3.47)$$

being g_{gq} obtained from g_{qg} via the exchange $\hat{t} \rightarrow \hat{u}$. Note that, since the final state is colourless, the lowest-order partonic subprocess, $c + \bar{c} \rightarrow F$, is either $q\bar{q}$ annihilation ($c = q$), as in the case of γ^* , W and Z production in Drell-Yan processes, or gg fusion ($c = g$) in the case of the Higgs boson H .

For the computation of the order $\mathcal{O}(\alpha_s)$ corrections, one must consider three different sources. The virtual corrections (V) to Higgs plus one parton production, arising from the interference term between the Born and the one-loop amplitudes; the real corrections (R) from Higgs plus two partons; and finally the Altarelli-Parisi corrections (AP) arising from the definition of the $\overline{\text{MS}}$ parton densities at NLO.

Note that for the computation of the different V, R and AP contributions one must use some dimensional regularization procedure. As standard in perturbative QCD we use conventional dimensional regularization (CDR) with dimension $d = 4 - 2\varepsilon$, so that the collinear and soft singularities appear as ε -poles in the separate contributions, leading to a well-defined total contribution

$$G_{ij}^{(2)} = \lim_{\varepsilon \rightarrow 0} (G_{ij}^{(2R)}(\varepsilon) + G_{ij}^{(2V)}(\varepsilon) + G_{ij}^{(2AP)}(\varepsilon)). \quad (3.48)$$

For details about the explicit computation see [46].

As already mentioned, at small transverse momenta of the Higgs boson the perturbation series for the q_T spectrum becomes unstable, containing logarithmic enhancements of the type

$$\frac{\alpha_s^2}{q_\perp^2} \alpha_s^n \ln^{2n} \left(\frac{M_H^2}{q_T^2} \right), \quad (3.49)$$

with the leading logarithm occurring for $m = 2n - 1$. This logarithmic series has to be resummed, using the techniques developed by Collins, Soper, and Serman [50], among others, at various levels of approximation [51]. In the next chapter we discuss the resummation formalism, used to build a reliable prediction for the transverse momentum distribution in the whole q_T range.

Part II

Transverse momentum resummation

Transverse momentum resummation

In this chapter we describe the behavior of the q_T distribution of high-mass systems produced by hard-scattering of partons in hadron-hadron collisions. In ref [43, 48] some quantitative results on the q_T spectrum of the Standard Model Higgs boson are presented, produced via the gluon fusion mechanism at high energies - ranging from 8 TeV to 13 TeV - which are the typical energy scales addressed by the LHC. The formalism used in [43, 48] is quite general and applies to the transverse momentum distribution of generic high-mass systems, such as lepton pairs, vector bosons, Higgs particles, etc. In the following chapter we aim to describe first with some details this formalism, and then consider the explicit case of the Higgs boson transverse momentum distribution.

Since we aim to describe a wide range of q_T values, from the region $q_T \rightarrow 0$ to several hundreds of GeV, it is useful to separately consider the large- q_T and small- q_T regions. The large- q_T region will be described by the condition $q_T \gtrsim M$, such that the perturbative series is controlled by a small expansion parameter $\alpha_s(M^2)$, and the computation based on the truncation of the series at fixed order in α_s is theoretically justified. The SM Higgs boson production via gluon-gluon fusion at large- q_T requires an associated radiation of at least one recoiling parton, so the LO term for this observable is $\mathcal{O}(\alpha_s^3)$. The LO calculation is shown in ref [52]; it shows that the large- M_t approximation works well as long as $M_H \lesssim 2M_t$, and $q_T \lesssim M_t$. In the framework of the large- M_t approximation, the NLO QCD corrections to the transverse momentum distribution of the SM Higgs boson were computed in refs [46, 53, 54]. Corrections to the large- M_t approximation are shown in ref [55]. The theoretical calculations are implemented in the numerical programs of refs. [46, 53, 54].

In the small- q_T region, ($q_T \ll M$), where the bulk of events is produced, the convergence of the fixed order expansion is spoiled, since the coefficients of the perturbative series in $\alpha_s(M^2)$ are enhanced by powers of large logarithmic terms of the form $\ln^m(M^2/q_T^2)$. Therefore to obtain reliable perturbative predictions, these terms have to be resummed to all orders in α_s . The method to systematically perform all-order resummation of logarithmically enhanced terms at small q_T is described with detail in [56, 57, 50, 58]. In the case of the SM Higgs boson, references are given in the next chapter, where resummation has been explicitly computed at leading-logarithmic (LL), next-to-leading logarithmic (NLL), and next-to-next-to-leading (NNLL) accuracy.

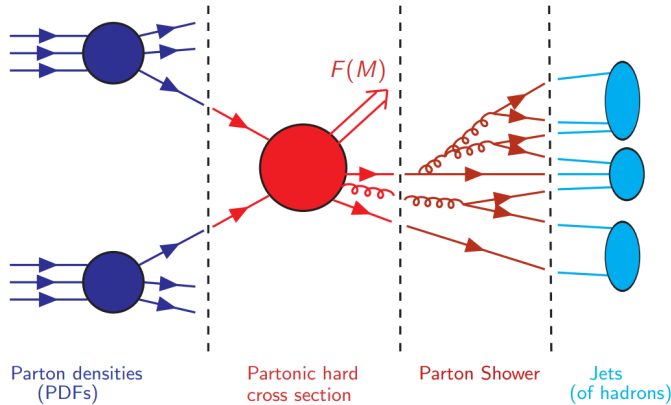


Figure 4.1: Representation of a hadronic collision as the one described by formula 4.1. Two hadrons h_1 and h_2 with momenta p_1 and p_2 produce some final-state system F , accompanied by an arbitrary and undetected final state X .

4.1 The resummation formalism

The resummation formalism is used in order to build reliable predictions where the truncation of the perturbation theory is not justified. As already mentioned, it is needed to account for the logarithmic enhancements that appear in the small q_T region, due to the unbalanced cancellation of divergences in exclusive final states. We consider the hard-scattering process depicted in Figure 4.1,

$$h_1(p_1) + h_2(p_2) \longrightarrow F(M, q_T) + X \quad (4.1)$$

where the collision of two hadrons h_1 and h_2 with momenta p_1 and p_2 produces some final-state system F , accompanied by an arbitrary and undetected final state X . We denote by \sqrt{s} the centre-of-mass energy of the colliding hadrons, given by

$$s = (p_1 + p_2)^2 \simeq 2p_1 p_2 . \quad (4.2)$$

The observed final state F is a generic system of non-QCD partons such as one or more vector bosons (γ, W, Z, \dots), Higgs particles, Drell-Yan (DY) lepton pairs and so on.

Through this manuscript we consider the case in which the total invariant mass M and transverse momentum q_T of the system F are measured. According to the QCD factorization theorem, already discussed in Chapter 2, the corresponding transverse momentum differential cross section¹ can be written as

$$\frac{d\sigma_F}{dq_T^2}(q_T, M, s) = \sum_{a,b} \int_0^1 dx_1 \int_0^1 dx_2 f_{a/h_1}(x_1, \mu_F^2) f_{b/h_2}(x_2, \mu_F^2) \frac{d\hat{\sigma}_F^{ab}}{dq_T^2}(q_T, M, \hat{s}; \alpha_s(\mu_R^2), \mu_R^2, \mu_F^2) , \quad (4.3)$$

¹To be precise, when the final state F is not a single on-shell particle of mass M , but some intermediate state that will produce some decay products, what we denote by $d\hat{\sigma}/dq_T^2$ is actually the differential cross section $M^2 d\hat{\sigma}/dM^2 dq_T^2$. In the case of the Higgs boson the invariant mass distribution can - sometimes - reasonably be considered a delta distribution, given the small value of its decay width. This is called the Narrow Width Approximation (NWA).

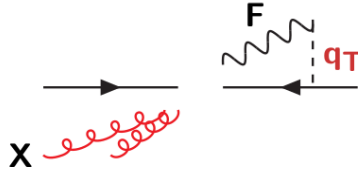


Figure 4.2: Representation of a hard interaction where the final state F is produced with some transverse momentum with respect to the beam axis. Unbalanced cancellation when dealing with such exclusive final states will lead to logarithmic enhancements dominating the cross section.

where $f_{a/h}(x, \mu_F^2)$ and $f_{b/h}(x, \mu_F^2)$ are the parton densities of the colliding hadrons at the factorization scale μ_F , $d\hat{\sigma}_{F ab}/dq_T^2$ is the partonic cross section, $\hat{s} = x_1 x_2 s$ the partonic center of mass energy, and μ_R the renormalization scale. For the whole discussion we use parton densities as defined in the $\overline{\text{MS}}$ factorization scheme, and $\alpha_s(q^2)$ is the QCD running coupling in the $\overline{\text{MS}}$ renormalization scheme.

The partonic cross section is computable in QCD perturbation theory, that is, it can be written as a power series expansion in α_s . We assume that at the parton level the system F is produced with vanishing q_T , meaning with no accompanying final state radiation in the lowest order approximation, in such a way that the corresponding cross section would behave as $d\hat{\sigma}_{F ab}/dq_T^2 \propto \delta(q_T^2)$. Since F is colourless, the lowest-order partonic subprocess, $c + \bar{c} \rightarrow F$, is either $q\bar{q}$ annihilation ($c = q$), as in the case of γ^* , W and Z production in Drell-Yan processes, or gg fusion ($c = g$) in the case of the Higgs boson H .

Since we are dealing with an semi-inclusive final state, the cancellation of infrared singularities comes unbalanced, as recalled in Chapter 2, and higher-order perturbative contributions to the partonic cross section $d\hat{\sigma}_{F ab}/dq_T^2$ contain logarithmic terms of the type $\ln^m(M^2/q_T^2)$ that become large in the small q_T region ($q_T \ll M$). Therefore, we introduce in eq. 4.3 the following decomposition of the partonic cross section

$$\frac{d\hat{\sigma}_{F ab}}{dq_T^2} = \frac{d\hat{\sigma}_{F ab}^{(\text{res.})}}{dq_T^2} + \frac{d\hat{\sigma}_{F ab}^{(\text{fin.})}}{dq_T^2}. \quad (4.4)$$

Note that this distinction between the two terms on the right-hand side is purely theoretical. It is done in such a way that the $d\hat{\sigma}_{F ab}^{(\text{res.})}$ contains all the logarithmically-enhanced contributions

$$\frac{\alpha_s^n}{q_T^2} \ln^m \left(\frac{M^2}{q_T^2} \right),$$

and has to be evaluated by resumming them to all orders in α_s . The second term, $d\hat{\sigma}_{F ab}^{(\text{fin.})}$, is free of such contributions, and can be computed by fixed-order truncation of the perturbative series. Indeed, when we define the so-called "finite" component $d\hat{\sigma}_{F ab}^{(\text{fin.})}$ we do impose

$$\lim_{Q_T \rightarrow 0} \int_0^{Q_T^2} dq_T^2 \left[\frac{d\hat{\sigma}_{F ab}^{(\text{fin.})}}{dq_T^2} \right]_{\text{F.O.}} = 0, \quad (4.5)$$

where the right-hand side must vanish order by order in perturbation theory. In particular, this implies that any perturbative contributions proportional to $\delta(q_T^2)$ have been

$\alpha_S L^2$	$\alpha_S L$	\dots	$\mathcal{O}(\alpha_S)$
$\alpha_S^2 L^4$	$\alpha_S^2 L^3$	\dots	$\mathcal{O}(\alpha_S^2)$
\dots	\dots	\dots	\dots
$\alpha_S^n L^{2n}$	$\alpha_S^n L^{2n-1}$	\dots	$\mathcal{O}(\alpha_S^n)$
dominant logs	\dots	\dots	\dots

Figure 4.3: Table representing logarithmic enhancements of the type $L = \ln M^2 b^2$ appearing at different orders. All these contributions will be absorbed inside the Sudakov form factor $\exp\{\mathcal{G}\}$.

removed from $d\hat{\sigma}_{F ab}^{(\text{fin.})}$ and absorbed in $d\hat{\sigma}_{F ab}^{(\text{res.})}$.

To sum up, we will evaluate the q_T distribution in eq. 4.3 by replacing the cross section on the right-hand side in the following way

$$\frac{d\hat{\sigma}_{F ab}}{dq_T^2} \longrightarrow \left[\frac{d\hat{\sigma}_{F ab}^{(\text{res.})}}{dq_T^2} \right]_{\text{L.A.}} + \left[\frac{d\hat{\sigma}_{F ab}^{(\text{fin.})}}{dq_T^2} \right]_{\text{F.O.}} \quad (4.6)$$

where the logarithmically enhanced terms inside the resummed component $d\hat{\sigma}_{F ab}^{(\text{res.})}$ can be organized as LL, NLL, NNLL, ..., and then it is *this* logarithmic expansion that can be truncated at some logarithmic accuracy (L.A.). In a similar way, the finite component is truncated at some fixed order (F.O.) of the perturbative series. The distinction is done such that the resummed component describes the behavior in the small- q_T region, while the finite component dominates at large values of q_T .

Note that the resummed contributions inside $[d\hat{\sigma}_{F ab}^{(\text{res.})}]_{\text{L.A.}}$ are necessary and fully justified at small q_T . Although, they can lead to sizeable higher-order effects also at large q_T , where the resummed expansion is not supposed to be valid. To reduce the impact of these unjustified higher-order terms, a unitarity constraint is applied, requiring that they give no contributions to the total cross section. This is implemented by imposing the following condition

$$\int_0^\infty dq_T^2 \left[\frac{d\hat{\sigma}_{F ab}^{(\text{res.})}}{dq_T^2} \right]_{\text{L.A.}} = \int_0^\infty dq_T^2 \left[\frac{d\hat{\sigma}_{F ab}^{(\text{res.})}}{dq_T^2} \right]_{\text{F.O.}}, \quad (4.7)$$

which means, that the total cross section remains unaffected by small- q_T logarithmic terms. As a matter of fact, the logarithmic contributions contained in $d\hat{\sigma}_{F ab}^{(\text{res.})}$ are plus distributions of the type

$$\left[\frac{\alpha_s^n}{q_T^2} \ln^m \left(\frac{M^2}{q_T^2} \right) \right]_+, \quad (4.8)$$

therefore it is natural to require that these resummed terms give a vanishing contribution to the total cross section. A detailed description of the plus distributions and how to address them in the context of resummation can be found in Appendix A. As a final note before discussing the details of the resummed and finite components, note that this formalism implements the QCD resummation at the level of the partonic cross section. In the factorization formula 4.3, the parton densities are evaluated at the factorization scale μ_F . The theoretical uncertainty of the resummed calculation can be investigated as in customary fixed-order calculations, by varying μ_F and μ_R around this central value.

4.2 The resummed component

The resummation method for the logarithmically-enhanced contributions at small q_T was set up [50, 56, 58] shortly after the first resummed calculation of the DY transverse momentum spectrum to double logarithmic accuracy. The resummation procedure has to be carried out in the impact parameter space, to correctly take into account the kinematic constraints from transverse momentum conservation.

The resummed component $d\hat{\sigma}_{F,ab}^{(\text{res.})}$ of the partonic cross section in eq. 4.4 is then obtained by performing the inverse Fourier-Bessel transformation with respect to the impact parameter b .

$$\begin{aligned} \frac{d\hat{\sigma}_{F,ab}^{(\text{res.})}}{dq_T^2}(q_T, M, \hat{s}; \alpha_s(\mu_R^2), \mu_R^2, \mu_F^2) &= \frac{M^2}{\hat{s}} \int \frac{d^2\mathbf{b}}{4\pi} e^{i\mathbf{b}\cdot\mathbf{q}_T} \mathcal{W}_{ab}^F(b, M, \hat{s}; \alpha_s(\mu_R^2), \mu_R^2, \mu_F^2) \\ &= \frac{M^2}{\hat{s}} \int_0^\infty db \frac{b}{2} J_0(bq_T) \mathcal{W}_{ab}^F(b, M, \hat{s}; \alpha_s(\mu_R^2), \mu_R^2, \mu_F^2), \end{aligned} \quad (4.9)$$

where the 0th-order Bessel function $J_0(x)$ arises from the 2-dimensional Fourier transformation, also referred to as Hankel transformation.

The process dependent factor \mathcal{W}_{ab}^F embodies the all-order dependence on the large logarithms $L = \ln M^2 b^2$ at large b , which corresponds to the q_T -space terms $\ln M^2/q_T^2$ that are logarithmically enhanced at small q_T . Note that the small- q_T limit $q_T \ll M$ we have been referring to now corresponds to $Mb \gg 1$, since b and q_T are conjugated variables. Resummation of these large logarithms is better expressed by defining the N -moments $\mathcal{W}_{ab,N}^F$ of the resummed cross section \mathcal{W}_{ab}^F with respect to $z = M^2/\hat{s}$ at fixed M ,

$$\mathcal{W}_{ab,N}^F(b, M; \alpha_s(\mu_R^2), \mu_F^2) \equiv \int_0^1 dz z^{N-1} \mathcal{W}_{ab}^F(b, M, \hat{s} = M^2/z; \alpha_s(\mu_R^2), \mu_F^2). \quad (4.10)$$

The logarithmic terms included in $\mathcal{W}_{ab,N}^F$ are due to final-state radiation of soft and/or collinear partons with respect to the incoming ones. Their all-order resummation can be organized in close analogy to the threshold contributions to hadronic cross sections [32], and for the cases of soft-gluon resummation in hard scattering processes [59, 60]. The structure of $\mathcal{W}_{ab,N}^F$ can indeed be factorized in exponential form as follows

$$\begin{aligned} \mathcal{W}_{ab,N}^F(b, M; \alpha_s(\mu_R^2), \mu_F^2) &= \mathcal{H}_N^F(M, \alpha_s(\mu_R^2); M^2/\mu_R^2, M^2/\mu_F^2, M^2/Q^2) \\ &\quad \times \exp \{ \mathcal{G}_N(\alpha_s(\mu_R^2), L; M^2/\mu_R^2, M^2/Q^2) \}, \end{aligned} \quad (4.11)$$

where, for simplicity, the subscripts denoting the flavour indices are implicit². The function \mathcal{H}_N^F is process dependent, and it does not depend on q_T and hence on the impact parameter b . Therefore it contains all the contributions that behave as constants in the limit $b \rightarrow \infty$. The function \mathcal{G} is process independent and includes the complete dependence

²More precisely, we are writing here the resummation formulae in a simplified form which is valid when there is a single species of partons. In the general case, the exponential is replaced by an exponential matrix with respect to the flavour indices of the partons.

on b . In particular, it contains all the terms that order by order in α_s are logarithmically divergent when $b \rightarrow \infty$. The specific form of those large logarithmic terms is given by

$$\alpha_s^n L^m = \alpha_s^n \ln^m \frac{M^2 b^2}{b_0^2}, \quad (4.12)$$

where $b_0 = 2e^{-\gamma_E}$ and $\gamma_E = 0.5772\dots$ is the Euler-Mascheroni constant. All terms with $1 \leq m \leq 2n$ are included in the form factor $\exp\{\mathcal{G}\}$. Indeed, all logarithmic contributions to \mathcal{G} with $n+2 \leq m \leq 2n$ are vanishing. The \mathcal{G} factor is commonly referred to as the *Sudakov form factor*, and it can be systematically expanded as

$$\begin{aligned} \mathcal{G}_N(\alpha_s, L; M^2/\mu_R^2, M^2/Q^2) &= Lg_N^{(1)}(\alpha_s L) + g_N^{(2)}(\alpha_s L; M^2/\mu_R^2, M^2/Q^2) \\ &+ \frac{\alpha_s}{\pi} g_N^{(3)}(\alpha_s L; M^2/\mu_R^2, M^2/Q^2) \\ &+ \sum_{n=4}^{\infty} \left(\frac{\alpha_s}{\pi}\right)^{n-2} g_N^{(n)}(\alpha_s L; M^2/\mu_R^2, M^2/Q^2), \end{aligned} \quad (4.13)$$

property that is referred to as exponentiation. The functions $g^{(n)}$ are defined such that $g^{(n)} = 0$ when $\alpha_s L = 0$. Thus the term $Lg^{(1)}$ collects all the LL contributions $\alpha_s^n L^{n+1}$, the function $g^{(2)}$ contains the NLL contributions $\alpha_s^n L^n$, $g^{(3)}$ the NNLL $\alpha_s^n L^{n-1}$, and so on and so forth.

The functions $g_N^{(n)}(\alpha_s L)$ inside the Sudakov form factor can be expressed in terms of the perturbative coefficients known as $A^{(n)}, B^{(n)}$ [43, 48]. Here we show the explicit form of the first $g_N^{(n)}(\alpha_s L)$ factors, which is written as follows:

$$g^{(1)}(\alpha_s L) = \frac{A^{(1)} \lambda + \ln(1-\lambda)}{\beta_0 \lambda} \quad (4.14)$$

$$\begin{aligned} g^{(2)}\left(\alpha_s L; \frac{M_H}{\mu_R^2}, \frac{M_H^2}{Q^2}\right) &= \frac{\overline{B}_N^{(1)}}{\beta_0} \ln(1-\lambda) \frac{A^{(2)}}{\beta_0^2} \left(\frac{\lambda}{1-\lambda} + \ln(1-\lambda)\right) \\ &+ \frac{A^{(1)}}{\beta_0} \left(\frac{\lambda}{1-\lambda} + \ln(1-\lambda)\right) \ln \frac{Q^2}{\mu_R^2} \\ &+ \frac{A^{(1)}\beta_1}{\beta_0^3} \left(\frac{1}{2} \ln^2(1-\lambda) + \frac{\ln(1-\lambda)}{1-\lambda} + \frac{\lambda}{1-\lambda}\right), \end{aligned} \quad (4.15)$$

$$\begin{aligned} g^{(3)}\left(\alpha_s L; \frac{M_H}{\mu_R^2}, \frac{M_H^2}{Q^2}\right) &= -\frac{A^{(3)}}{2\beta_0^2} \frac{\lambda^2}{(1-\lambda)^2} - \frac{\overline{B}_N^{(1)}}{\beta_0} \frac{\lambda}{1-\lambda} \\ &+ \frac{A^{(2)}\beta_1}{\beta_0^3} \left(\frac{\lambda(3\lambda-2)}{2(1-\lambda)^2} - \frac{(1-2\lambda)\ln(1-\lambda)}{(1-2\lambda)^2}\right) \\ &+ \frac{\overline{B}_N^{(1)}\beta_1}{\beta_0^2} \left(\frac{\lambda}{1-\lambda} + \frac{\ln(1-\lambda)}{1-\lambda}\right) - \frac{A^{(1)}}{2} \frac{\lambda^2}{(1-\lambda)^2} \ln \frac{Q^2}{\mu_R^2} \\ &+ \frac{Q^2}{\mu_R^2} \left(\overline{B}^{(1)N} \frac{\lambda}{1-\lambda} + \frac{A^{(2)}}{\beta_0} \frac{\lambda^2}{(1-\lambda)^2} + A^{(1)} \frac{\beta_1}{\beta_0^2} \left(\frac{\lambda}{1-\lambda} + \frac{1-2\lambda}{(1-\lambda)^2} \ln(1-\lambda)\right)\right) \\ &+ A^{(1)} \left(\frac{\beta_1^2}{2\beta_0^4} \frac{1-2\lambda}{(1-\lambda)^2} \ln^2(1-\lambda) + \ln(1-\lambda) \left[\frac{\beta_0\beta_2 - \beta_1^2}{\beta_0^4} + \frac{\beta_1^2}{\beta_0^4(1-\lambda)}\right]\right) \\ &+ \frac{\lambda}{2\beta_0^4(1-\lambda)^2} (\beta_0\beta_2(2-3\lambda) + \beta_1^2\lambda), \end{aligned} \quad (4.16)$$

being λ and $\overline{B}_N^{(n)}$ given by

$$\lambda = \frac{1}{\pi} \beta_0 \alpha_s(\mu_R^2) L, \quad (4.17)$$

$$\overline{B}_N^{(n)} = \tilde{B}_N^{(n)} + A^{(n)} \ln \frac{M}{Q^2}, \quad (4.18)$$

and β_n are the coefficients of the QCD β function we already discussed in Chapter 1,

$$\frac{d \ln \alpha_s(\mu^2)}{d \ln \mu^2} = \beta(\alpha_s(\mu^2)) = - \sum_{n=0}^{\infty} \beta_n \left(\frac{\alpha_s}{\pi} \right)^{n+1}. \quad (4.19)$$

Note that $g_N^{(1)}$ depends only on $A^{(1)}$, $g_N^{(2)}$ also depends on $B^{(1)}$ and $A^{(2)}$, $g_N^{(3)}$ also depends on $B^{(2)}$ and $A^{(3)}$ and so on and so forth. We also observe that the functions $g_N^{(2)}$ and $g_N^{(3)}$ receive additional contributions from the LO and NLO anomalous dimensions that control the evolution of the parton densities.

Also, the functions $g_N^{(n)}(\alpha_s L)$ are singular when $\lambda = \beta_0 \alpha_s L \rightarrow 1$. This singular behaviour is related to the presence of the Landau pole in the perturbative running of the QCD coupling. To properly define the b integration in equation 4.9, a prescription to deal with these singularities must be introduced. Here we follow ref [61] and deform the integration contour in the complex b -space, as an extension of the minimal prescription of ref. [32].

The function \mathcal{H}_N^F on equation 4.9 does not depend on b and, hence, its evaluation does not require resummation of large logarithmic terms. It can also be expanded in series of α_s as

$$\begin{aligned} \mathcal{H}_N^F(M, \alpha_s(\mu_R^2); M^2/\mu_R^2, M^2/\mu_F^2, M^2/Q^2) = & \sigma^{(0)}(\alpha_s, M) \left[1 + \frac{\alpha_s}{\pi} \mathcal{H}_N^{(1)}(M^2/\mu_R^2, M^2/\mu_F^2, M^2/Q^2) \right. \\ & + \left(\frac{\alpha_s}{\pi} \right)^2 \mathcal{H}_N^{(2)}(M^2/\mu_R^2, M^2/\mu_F^2, M^2/Q^2) \\ & \left. + \sum_{n=3}^{\infty} \left(\frac{\alpha_s}{\pi} \right)^n \mathcal{H}_N^{(n)}(M^2/\mu_R^2, M^2/\mu_F^2, M^2/Q^2) \right], \end{aligned}$$

where $\sigma^{(0)} = \alpha_s^p \sigma^{\text{LO}}$ is the lowest order (Born-level) cross section for the hard scattering process in eq. 4.3. The explicit form of the first $\mathcal{H}_N^{(n)}$ coefficients is shown in the next section, together with the description of the finite component.

As a final comment, one must note that the expansion of eq. 4.13 is built such that the parameter $\alpha_s L$ is formally considered to be of order unity. Also, to reduce the impact of unjustified resummed logarithms in the large- q_T region, where resummation is not supposed to play a dominant role, we can use a procedure inspired by [59], and perform in the expansion 4.13, the following replacement;

$$\mathcal{G}(\alpha_s L) \longrightarrow \mathcal{G}(\alpha_s \tilde{L}), \quad (4.20)$$

where the logarithmic variable L has been replaced by

$$\tilde{L} = \ln \left(\frac{M^2 b^2}{b_0^2} + 1 \right). \quad (4.21)$$

The reason for using \tilde{L} rather than L is the following. We clearly see that the use of one or another is equivalent in the small- q_T region, where $Mb \rightarrow \infty$, since there $\tilde{L} \sim L$. On the other hand, when $Mb \ll 1$, $\tilde{L} \rightarrow 0$ and $\exp\{\mathcal{G}\} \rightarrow 1$. Therefore, using the definition in eq. 4.21 we avoid the introduction of all-order contributions in the small- b region, where the use of the large- b resummation formalism is not justified. In particular, $\exp\{\mathcal{G}\} = 1$ at $b = 0$. This implies that the integral over q_T of $d\sigma/dq_T$ exactly reproduces the fixed-order calculation of the total cross section. Since resummed and fixed-order perturbation theory control the small- q_T and large- q_T regions respectively, the total cross section constraint mainly acts on the size of the higher order contributions introduced in the intermediate- q_T region by the matching procedure [43, 48]

4.3 The finite component

The finite component $d\hat{\sigma}_{ab}^{(\text{fin.})}$ of the partonic cross section is computed at a given order in α_s , according to eq. 4.4. It does not contain any contribution proportional to $\delta(q_T^2)$, and it can be written as

$$\frac{d\hat{\sigma}_{F ab}^{(\text{fin.})}}{dq_T^2} = \left[\frac{d\hat{\sigma}_{F ab}}{dq_T^2} \right]_{\text{F.O.}} - \left[\frac{d\hat{\sigma}_{F ab}^{(\text{res.})}}{dq_T^2} \right]_{\text{F.O.}}. \quad (4.22)$$

The first term is the usual perturbative series for the partonic cross section truncated at a fixed order in α_s . The second one is obtained by truncating the resummed component at the *same* fixed order in α_s . The small- q_T (resummed) and large- q_T (fixed-order) approaches are thus consistently matched by avoiding double-counting in the intermediate q_T region. This procedure guarantees that the right-hand side of eq. 4.4 contains full information of the perturbative calculation up to the fixed order specified, plus resummation of the logarithmically-enhanced contributions from higher orders.

Moreover, we impose the condition

$$\left[\left[\frac{d\hat{\sigma}_{F ab}^{(\text{res.})}}{dq_T^2} \right]_{\text{L.A.}} \right]_{\text{F.O.}} = \left[\frac{d\hat{\sigma}_{F ab}^{(\text{res.})}}{dq_T^2} \right]_{\text{F.O.}}, \quad (4.23)$$

which implies that the replacement retains the full information of the perturbative calculation up to the specified order plus resummation of logarithmically enhanced contributions from higher orders. Equations 4.22 and 4.23 indeed imply that the matching is perturbatively exact, in the sense that the fixed-order truncation in the right-hand side of 4.22 exactly reproduces the customary fixed-order truncation of the partonic cross section in 4.3.

The fixed order truncation of the resummed component, $[d\hat{\sigma}_{F ab}^{(\text{res.})}]_{\text{F.O.}}$, is obtained by perturbatively expanding $d\hat{\sigma}_{F ab}^{(\text{res.})}$ in terms of the $\tilde{\Sigma}^{(n)}$ coefficients as follows:

$$\begin{aligned} \mathcal{W}_{ab}^F(b, M, \hat{s}, \alpha_s; \mu_R^2, \mu_F^2, Q^2) &= \sum_c \sigma_{c\bar{c}}^{(0)}(\alpha_s, M) \left\{ \delta_{ca} \delta_{\bar{c}b} \delta(1-z) \right. \\ &+ \sum_{n=1}^{\infty} \left(\frac{\alpha_s}{\pi} \right)^n \left[\tilde{\Sigma}_{c\bar{c}\leftarrow ab}^{(n)} \left(z, \tilde{L}; \frac{M^2}{\mu_R^2}, \frac{M^2}{\mu_F^2}, \frac{M^2}{Q^2} \right) \right. \\ &\left. \left. + \mathcal{H}_{c\bar{c}\leftarrow ab}^{F(n)} \left(z; \frac{M^2}{\mu_R^2}, \frac{M^2}{\mu_F^2}, \frac{M^2}{Q^2} \right) \right] \right\} \end{aligned} \quad (4.24)$$

where $z = M^2/\hat{s}$, and the power p_{cF} inside the $\tilde{\Sigma}_{ab}$ and $\mathcal{H}_{c\bar{c}\leftarrow ab}^{F(n)}$ depends on lowest order partonic subprocesses $c + \bar{c} \rightarrow F$. Note, however, that equation 4.24 depends on the resummation scale Q^2 . This dependence has been introduced in eq. 4.11 through the replacement in 4.21. The perturbative coefficient $\tilde{\Sigma}_{(n)}$ on the right-hand side is a polynomial of degree $2n$ in the logarithmic variable \tilde{L} . The coefficients $\tilde{\Sigma}_{(n)}$ vanish by definition when $\tilde{L} = 0$, (i.e. when $b = 0$), and the b -independent part of $\mathcal{W}_{ab,N}^F(b, M)$ is embodied in the hard factors $\mathcal{H}^{(n)}$.

For computing the coefficients needed in the finite cross section, the perturbative expansion in 4.11, and specifically 4.24 gives

$$\tilde{\Sigma}_{c\bar{c}\leftarrow ab}^{F(1)}(z, \tilde{L}) = \Sigma_{c\bar{c}\leftarrow ab}^{F(1;2)}(z) \tilde{L}^2 + \Sigma_{c\bar{c}\leftarrow ab}^{F(1;1)}(z) \tilde{L} \quad (4.25)$$

$$\tilde{\Sigma}_{c\bar{c}\leftarrow ab}^{F(2)}(z, \tilde{L}) = \Sigma_{c\bar{c}\leftarrow ab}^{F(2;4)}(z) \tilde{L}^4 + \Sigma_{c\bar{c}\leftarrow ab}^{F(2;3)}(z) \tilde{L}^3 + \Sigma_{c\bar{c}\leftarrow ab}^{F(2;2)}(z) \tilde{L}^2 + \Sigma_{c\bar{c}\leftarrow ab}^{F(2;1)}(z) \tilde{L}, \quad (4.26)$$

where the dependence on the ratios M^2/μ_R^2 , M^2/μ_F^2 , M^2/Q^2 is again understood. It is straightforward to extend the expansion in 4.26 to higher orders with $n \geq 3$. The b -independent coefficients $\Sigma_{c\bar{c}\leftarrow ab}^{F(1;k)}(z)$, $\mathcal{H}_{ab}^{F(1)}(z)$, $\Sigma_{c\bar{c}\leftarrow ab}^{F(2;k)}(z)$, $\mathcal{H}_{ab}^{F(2)}(z)$ are more easily presented by considering their N -moments with respect to the variable z . These hard coefficients can be expanded as a perturbative series in α_s , being the first contributions written as follows (Bozzi et al., [43, 48])

$$\begin{aligned} \mathcal{H}_{ab,N}^{F(1)}\left(\frac{M^2}{\mu_R^2}, \frac{M^2}{\mu_F^2}, \frac{M^2}{Q^2}\right) &= \delta_{ca}\delta_{\bar{c}b}\left[H_c^{(1)} - \left(B_c^{(1)} + \frac{1}{2}A_c^{(1)}l_Q\right)l_Q - p_{cF}\beta_0l_R\right] \\ &+ \delta_{ca}C_{\bar{c}b,N}^{(1)} + \delta_{\bar{c}b}C_{ca,N}^{(1)} + \left(\delta_{ca}\gamma_{\bar{c}b,N}^{(1)} + \delta_{\bar{c}b}\gamma_{ca,N}^{(1)}\right)(l_F - l_Q), \end{aligned} \quad (4.27)$$

$$\begin{aligned} \mathcal{H}_{ab,N}^{F(2)}\left(\frac{M^2}{\mu_R^2}, \frac{M^2}{\mu_F^2}, \frac{M^2}{Q^2}\right) &= \delta_{ca}\delta_{\bar{c}b}\left[H_c^{(2)} - \delta_{ca}C_{\bar{c}b,N}^{(2)} + \delta_{\bar{c}b}C_{ca,N}^{(2)} + C_{ca,N}^{(1)}C_{\bar{c}b,N}^{(1)}\right. \\ &+ H_c^{(1)}\left(\delta_{ca}C_{\bar{c}b,N}^{(1)} + \delta_{\bar{c}b}C_{ca,N}^{(1)}\right) + \frac{1}{6}A_c^{(1)}\beta_0l_Q^3\delta_{ca}\delta_{\bar{c}b} + \frac{1}{2}\left[A_c^{(2)}\delta_{ca}\delta_{\bar{c}b}\beta_0\Sigma_N^{(1;1)}\left(M_H^2/Q^2\right)\right]l_Q \\ &- \left[\delta_{ca}\delta_{\bar{c}b}\left(B_c^{(2)} + A_c^{(2)}l_Q\right) - \beta_0\left(\delta_{ca}C_{\bar{c}b,N}^{(1)} + \delta_{\bar{c}b}C_{ca,N}^{(1)}\right) + \delta_{ca}\gamma_{\bar{c}b,N}^{(2)} + \delta_{\bar{c}b}\gamma_{ca,N}^{(2)}\right]l_Q \\ &+ \frac{1}{2}\beta_0\left(\delta_{ca}\gamma_{\bar{c}b,N}^{(1)} + \delta_{\bar{c}b}\gamma_{ca,N}^{(1)}\right)l_F^2 + \left(\delta_{ca}\gamma_{\bar{c}b,N}^{(2)} + \delta_{\bar{c}b}\gamma_{ca,N}^{(2)}\right)l_F - \mathcal{H}_N^{(1)}\left(\frac{M^2}{\mu_F^2}, \frac{M^2}{\mu_F^2}, \frac{M^2}{Q^2}\right)\beta_0l_R \\ &+ \frac{1}{2}\sum_{a_1,b_1}\left[\mathcal{H}_{a_1b_1}^{(1)}\left(\frac{M^2}{\mu_F^2}, \frac{M^2}{\mu_F^2}, \frac{M^2}{Q^2}\right) + \delta_{ca_1}\delta_{\bar{c}b_1}H_C^{(1)} + \delta_{ca_1}C_{\bar{c}b_1,N}^{(1)} + \delta_{\bar{c}b_1}C_{ca_1,N}^{(1)}\right] \\ &\times \left[\left(\delta_{a_1a}\gamma_{b_1b,N}^{(1)} + \delta_{b_1b}\gamma_{a_1a,N}^{(2)}\right)(l_F - l_Q) - \delta_{a_1a}\delta_{b_1b}\left(\left(B_c^{(1)} + \frac{1}{2}A_c^{(1)}l_Q\right)l_Q - p_{cF}\beta_0l_R\right)\right] \\ &- \delta_{ca}\delta_{\bar{c}b}p_{cF}\left(\frac{1}{2}\beta_0^2l_R^2 + \beta_1l_R\right). \end{aligned} \quad (4.28)$$

Note that, as it happens with the $g_N^{(n)}$ coefficients, $\mathcal{H}_N^{(1)}$ depends on $H^{(1)}$ and $C^{(1)}$, $\mathcal{H}_N^{(2)}$ also depends on $H^{(2)}$ and $C^{(2)}$, and so on and so forth. The terms l_R , l_F and l_Q are defined as

$$l_R = \ln \frac{M^2}{\mu_R^2}, \quad l_F = \ln \frac{M^2}{\mu_F^2}, \quad l_Q = \ln \frac{M^2}{Q^2}, \quad (4.29)$$

referring to the ratios of the hard scale with respect to the renormalization, factorization and resummation scale, respectively. Ideally, those scales are usually set to the order of the hard scale, $\mu_R \sim \mu_F \sim Q \sim M$, such that those logarithms give zero contribution. One can, hence, slightly change the values of those scales around their central value to obtain an estimation of the perturbative uncertainty from unbalanced higher order corrections.

Similarly, the first $\Sigma_{ab,N}^{(n)}$ components have the following structure (Bozzi et al.)

$$\Sigma_{ab,N}^{(1;2)} = -\frac{1}{2}A_c^{(1)}\delta_{ca}\delta_{\bar{c}b}, \quad (4.30)$$

$$\Sigma_{ab,N}^{(1;1)}(M^2/Q^2) = -\left[\delta_{ca}\delta_{\bar{c}b}\left(B_c^{(1)} + A_c^{(1)}l_Q\right) + \delta_{ca}\gamma_{\bar{c}b,N}^{(1)} + \delta_{\bar{c}b}\gamma_{ca,N}^{(1)}\right], \quad (4.31)$$

$$\Sigma_{ab,N}^{(2;4)} = \frac{1}{8}(A_c^{(1)})^{(1)}\delta_{ca}\delta_{\bar{c}b}, \quad (4.32)$$

$$\Sigma_{ab,N}^{(2;3)}(M^2/Q^2) = -A_c^{(1)}\left[\frac{1}{3}\beta_0\delta_{ca}\delta_{\bar{c}b} + \frac{1}{2}\Sigma_{ab,N}^{(1;1)}(M^2/Q^2)\right], \quad (4.33)$$

$$\begin{aligned} \Sigma_{ab,N}^{(2;2)}\left(\frac{M^2}{\mu_R^2}, \frac{M^2}{\mu_F^2}, \frac{M^2}{Q^2}\right) &= -\frac{1}{2}A_c^{(1)}\left[\mathcal{H}_{ab,N}^{(1)}\left(\frac{M^2}{\mu_R^2}, \frac{M^2}{\mu_F^2}, \frac{M^2}{Q^2}\right) - \beta_0\delta_{ca}\delta_{\bar{c}b}(l_R - l_Q)\right] \\ &\quad - \frac{1}{2}\sum_{a_1,b_1}\Sigma_{a_1b_1,N}^{(1;1)}(M^2/Q^2)\left[\delta_{a_1a}\gamma_{b_1b,N}^{(1)} + \delta_{b_1b}\gamma_{a_1a,N}^{(1)}\right] \\ &\quad - \frac{1}{2}\left[A_c^{(2)}\delta_{ca}\delta_{\bar{c}b}(B_c^{(1)} + A_c^{(1)}l_Q - \beta_0)\Sigma_{a_1b_1,N}^{(1;1)}(M^2/Q^2)\right], \end{aligned} \quad (4.34)$$

$$\begin{aligned} \Sigma_{ab,N}^{(2;1)}\left(\frac{M^2}{\mu_R^2}, \frac{M^2}{\mu_F^2}, \frac{M^2}{Q^2}\right) &= \Sigma_{ab,N}^{(1;1)}(M^2/Q^2)\beta_0(l_Q - l_R) \\ &\quad - \sum_{a_1,b_1}\mathcal{H}_{a_1b_1,N}^{(1)}\left(\frac{M^2}{\mu_R^2}, \frac{M^2}{\mu_F^2}, \frac{M^2}{Q^2}\right)\left[\delta_{a_1a}\delta_{b_1b}\left(B_c^{(1)} + A_c^{(1)}l_Q\right) + \delta_{a_1a}\gamma_{b_1b,N}^{(1)} + \delta_{b_1b}\gamma_{a_1a,N}^{(1)}\right] \\ &\quad - \left[\delta_{ca}\delta_{\bar{c}b}(B_c^{(2)} + A_c^{(2)}l_Q) - \beta_0\left(\delta_{ca}C_{\bar{c}b,N}^{(1)} + \delta_{\bar{c}b}C_{ca,N}^{(1)}\right) + \delta_{ca}\gamma_{\bar{c}b,N}^{(2)} + \delta_{\bar{c}b}\gamma_{ca,N}^{(2)}\right], \end{aligned} \quad (4.35)$$

This way we can write the fixed-order expansion of the resummed cross section as follows. For the leading order we have

$$\begin{aligned} \left[\frac{d\hat{\sigma}_{F,ab}^{(\text{res.})}}{dq_T^2}(q_T, M, \hat{s} = \frac{M^2}{z}; \alpha_s(\mu_R^2), \mu_R^2, \mu_F^2, Q^2)\right]_{\text{LO}} &= \frac{\alpha_s(\mu_R^2)}{\pi} \frac{z}{Q^2} \sum_c \sigma_{c\bar{c},F}^{(0)}(\alpha_s(\mu_R^2), M) \\ &\quad \times \left[\tilde{\Sigma}_{c\bar{c}\leftarrow ab}^{F(1;2)}(z) \tilde{I}_2(q_T/Q) + \tilde{\Sigma}_{c\bar{c}\leftarrow ab}^{F(1;1)}\left(z, \frac{M^2}{Q^2}\right) \tilde{I}_1(q_T/Q)\right]. \end{aligned} \quad (4.36)$$

And for the next-to-leading

$$\begin{aligned} \left[\frac{d\hat{\sigma}_{F,ab}^{(\text{res.})}}{dq_T^2}(q_T, M, \hat{s} = \frac{M^2}{z}; \alpha_s(\mu_R^2), \mu_R^2, \mu_F^2, Q^2)\right]_{\text{NLO}} &= \left[\frac{d\hat{\sigma}_{F,ab}^{(\text{res.})}}{dq_T^2}(q_T, M, \hat{s} = \frac{M^2}{z}; \alpha_s(\mu_R^2), \mu_R^2, \mu_F^2, Q^2)\right]_{\text{LO}} \\ &\quad \left(\frac{\alpha_s(\mu_R^2)}{\pi}\right)^2 \frac{z}{Q^2} \sum_c \sigma_{c\bar{c},F}^{(0)}(\alpha_s(\mu_R^2), M) \sum_{k=1}^4 \tilde{\Sigma}_{c\bar{c}\leftarrow ab}^{F(2;k)}\left(z, \frac{M^2}{\mu_R^2}, \frac{M^2}{\mu_F^2}, \frac{M^2}{Q^2}\right) \tilde{I}_k(q_T/Q) \end{aligned} \quad (4.37)$$

where the q_T dependence is fully embodied in the $\tilde{I}_n(q_T/Q)$ functions, which are obtained by the following Bessel transformation

$$\tilde{I}(q_T/Q) = Q^2 \int_0^\infty db \frac{b}{2} J_0(bq_T) \ln^2\left(\frac{Q^2 b^2}{b_0^2} + 1\right). \quad (4.38)$$

The term $\ln(Q^2 b^2/b_0 + 1) = \tilde{L}$ in the integrand comes from the replacement $L \rightarrow \tilde{L}$. In customary implementations of b -space resummation, one has to consider the Bessel transformation of powers of $\ln^n(Q^2 b^2/b_0) = L^n$, which can be expressed in terms of powers of $\ln^n(Q^2/q_T)$. The functions $\tilde{I}_n(q_T/Q)$ have instead a more involved functional dependence on q_T . As shown in Appendix B of [48], this functional dependence can be expressed in terms of $K_\nu(q_T/Q)$, the modified Bessel function with imaginary argument that is defined by the following integral representation.

$$K_\nu(q_T/Q) = \int_0^\infty dt e^{-x \cosh t} \cosh(\nu t). \quad (4.39)$$

Then the total cross section can finally be written as

$$\hat{\sigma}_{F ab}^{(\text{tot})}(M, \hat{s}; \alpha_s(\mu_R^2), \mu_R^2, \mu_F^2) = \int_0^\infty dq_T^2 \frac{d\hat{\sigma}_{F ab}}{dq_T^2}(q_T, M\hat{s}; \alpha_s(\mu_R^2), \mu_R^2, \mu_F^2) \quad (4.40)$$

and evaluate the q_T spectrum in the right-hand side according to the decomposition in terms of "resummed" and "finite". Then we can write

$$\hat{\sigma}_{F ab}^{(\text{tot})} = \frac{M^2}{\hat{s}} \mathcal{H}_{ab}^F + \int_0^\infty dq_T^2 \frac{\sigma_{F ab}^{(\text{fin.})}}{dq_T^2}. \quad (4.41)$$

This expression is valid order by order in QCD perturbation theory.

Note that the b -space resummation approach was formalized by Collins, Soper and Sterman (CSS) [50, 62] in terms of perturbative coefficients. It is written by the CSS formalism as

$$\frac{d\sigma}{dq_T^2}(q_T, M, s) = \frac{M^2}{s} \int_0^\infty db \frac{b}{2} J_0(bq_T) W^F(b, M, s) + \dots, \quad (4.42)$$

where the dots on the right-hand side stand for terms that are not logarithmically enhanced at small q_T (large b). One could notice already that eq. 4.42 regards the hadronic cross section rather than the partonic one, as in 4.9. Therefore, the b -space function $W^F(b, M, s)$ which embodies the logarithmically enhanced terms, depends on the parton densities of the colliding hadrons. The all-order resummation of the large logarithms $\ln(M^2 b^2)$ in the region $Mb \gg 1$ is accomplished by computing the N -moments $W_N^F(b, M)$ of $W(b, M, s)$ with respect to $z = M^2/s$ at fixed M , which can be written in the following form

$$\begin{aligned} W_N^F(b, M) &= \sum_c \sigma_{c\bar{c}, F}^{(0)}(\alpha_s(M^2), M) H_c^F(\alpha_s(M^2)) S_c(M, b) \\ &\times \sum_{a,b} C_{ca, N}(\alpha_s(b_0^2/b^2)) C_{\bar{c}b, N}(\alpha_s(b_0^2/b^2)) f_{a/h_1, N}(b_0^2/b^2) f_{b/h_2, N}(b_0^2/b^2). \end{aligned} \quad (4.43)$$

Here the Sudakov form factor has the following integral representation

$$S_c(M, b) = \exp \left\{ - \int_{b_0^2/b^2}^{M^2} \frac{dq^2}{q^2} \left[A_c(\alpha_s(q^2)) \ln \frac{M^2}{q^2} + B_c(\alpha_s(q^2)) \right] \right\}, \quad (4.44)$$

where this formula is invariant under resummation scheme transformations [48]. Comparing the partonic and hadronic cross sections in equations 4.9 and 4.43, we can see that $W^F(b, M)$ and \mathcal{W}_{ab}^F are related by

$$W^F(b, M) = \sum_{ab, N}^F \mathcal{W}_{ab}^F(b, M; \alpha_s(\mu_R^2), \mu_R^2, \mu_F^2) f_{a/h_1, N}(\mu_F^2) f_{b/h_2, N}(\mu_F^2), \quad (4.45)$$

where we can finally relate the resummed partonic cross section \mathcal{W}_{ab}^F in terms of the perturbative coefficients used for W^F , which at the end of the day will be written in terms of the N -moments of the Altarelli-Parisi splitting functions.

It is interesting feature, also from the pedagogical side, to consider the integral representation of the Sudakov form factor as defined in eq. 4.11, where the resummation is carried out at the partonic level,

$$\mathcal{G}_N(\alpha_s(\mu_R^2), L; M^2/\mu_R^2, M^2/Q^2) = - \int_{b_0^2/b^2}^{Q^2} \frac{dq^2}{q^2} \left[A(\alpha_s(q^2)) \ln \frac{M}{q^2} + \tilde{B}_N(\alpha_s(q^2)) \right], \quad (4.46)$$

and where we see that the perturbative coefficients $A(\alpha_s)$ and $B_N(\alpha_s)$ can be written as

$$A(\alpha_s) = \frac{\alpha_s}{\pi} A^{(1)} + \left(\frac{\alpha_s}{\pi} \right)^2 A^{(2)} + \sum_{n=3}^{\infty} \left(\frac{\alpha_s}{\pi} \right)^n A^{(n)}, \quad (4.47)$$

$$\tilde{B}_N(\alpha_s) = \frac{\alpha_s}{\pi} \tilde{B}_N^{(1)} + \left(\frac{\alpha_s}{\pi} \right)^2 \tilde{B}_N^{(2)} + \sum_{n=3}^{\infty} \left(\frac{\alpha_s}{\pi} \right)^n \tilde{B}_N^{(n)}. \quad (4.48)$$

The coefficients $A^{(n)}$ and $B^{(n)}$ are related to the customary coefficients of the Sudakov form factors and of the parton anomalous dimensions, as it is discussed in [48].

The resummed Higgs q_T distribution

To conclude this part of the thesis we apply the resummation formalism described in the previous chapter to the specific case of the Higgs boson production at the LHC. The case of the Higgs boson has been explicitly worked out at LL, NLL, and NNLL level. In the next chapter we will finally present the numerical code **HTurbo**, producing fast and accurate descriptions for the resummed and fixed-order q_T distributions, and we will also discuss the N³LO implementation.

The formalism used to compute the q_T distribution of the Higgs boson at the LHC is done by combining NNLL resummation at small q_T and NNLO perturbation theory at large- q_T . The fixed-order and resummed approaches at small and large values of q_T can then be matched at intermediate values, to obtain QCD predictions to the entire range of transverse momenta. Phenomenological studies of the transverse momentum distribution of the SM Higgs boson have been performed in refs [51, 63, 64, 65, 66], by combining resummed and fixed-order perturbation theory at different orders of theoretical accuracy.

We consider the gluon fusion production mechanism $gg \rightarrow H$, whose Born level cross section is given by

$$\sigma_{\bar{c}c,H}^{(0)}(\alpha_s, M_H) = \delta_{cg} \delta_{\bar{c}g} \alpha_s^2 \sigma^{(0)}(M_H; M_t, M_b), \quad (5.1)$$

where M_t and M_b are the masses of the top and bottom quarks, which circulate in the heavy-quark loop that couples to the Higgs boson. The Born-level cross section is written

$$\sigma^{(0)} = \frac{G_F}{288\pi\sqrt{2}} \left| \sum_Q A_Q \left(\frac{4M_Q^2}{M_H^2} \right) \right| \quad (5.2)$$

where G_F is the Fermi constant, and $M_Q = M_t, M_b$ denotes the on-shell pole mass of the top and bottom masses. For our numerical study they are set to the values $M_b = 4.75$ GeV and $M_t = 175$ GeV. Though the Born cross section is evaluated exactly, meaning including its dependence on the top and bottom quark masses, the computation of higher order QCD corrections is performed in the framework of the large- M_t approximation [67]

At small values of the transverse momentum, $q_T \ll M_H$, the q_T spectrum becomes unstable at any fixed-order, due to the large logarithms $\ln(M^2 b^2)$ coming from unbalanced cancellations of the IR singularities, which take the form that appears in Figure 4.3. At LO it diverges to positive infinity as $q_T \rightarrow 0$, as seen in Figure 1 of [43], while at

NLO it diverges to negative infinity, as seen in Figure 2 of [43]. These logarithmic corrections can be resummed, however, resulting in a well-behaved physical q_T spectrum, even in the small- q_T limit.

Following the techniques of Collins, Soper and Sterman ¹ and Bozzi et al. [43, 48], we can write the resummed Higgs q_T spectrum as an integral over the impact parameter [68, 69, 70]

$$\frac{d\sigma_F}{dq_T^2}(q_T, M_H, s) = \frac{M_H^2}{s} \int_0^\infty db b J_0(bq_T) W(b, M_H, s) + \dots, \quad (5.3)$$

where the dots on the right-hand side stand for terms that are logarithmically enhanced at small q_T (large b). Now, since the 5.3 regards the hadronic cross section, the b -space function $W(b, M_H, s)$, which embodies the logarithmically enhanced terms, depends on the parton densities of the colliding hadrons. For writing the all-order resummation of the large logarithms $\ln(M_H^2 b^2)$ in the region $M_s^2 b^2 \gg 1$ we compute the N -moments

$$W_N^F(b, M_H) = \sum_c \sigma_{c\bar{c},F}^{(0)}(\alpha_s(M_H^2), M_H) H_c^F S_c(M, b) \\ \times \sum_{a,b} C_{ca,N}(\alpha_s(b_0^2/b^2)) C_{c\bar{b},N}(\alpha_s(b_0^2/b^2)) f_{a/h_1,N}(b_0^2/b^2) f_{b/h_2,N}(b_0^2/b^2) \quad (5.4)$$

where $f_{a/h_1,N}(b_0^2/b^2)$ and $f_{b/h_2,N}(b_0^2/b^2)$ are the N -moments of the parton densities, $\sigma_{c\bar{c},F}^{(0)}$ the lowest-order cross section for the partonic subprocess $c + \bar{c} \rightarrow F$, and now the Sudakov form factor is given by the function S_c , which has the integral representation

$$S_c = \exp \left\{ - \int_{b_0^2/b^2}^{M_H^2} \frac{dq^2}{q^2} \left[A_c(\alpha_s(q)) \ln \frac{M_H^2}{q^2} + B_c(\alpha_s(q)) \right] \right\}. \quad (5.5)$$

By comparing eq. 5.4 and eq. 4.9 from last chapter we can see that resummed cross sections \mathcal{W}_{ab} and $W^F(b, M)$ are related by

$$W_N^F(b, M_H) = \sum_{a,b} \mathcal{W}_{ab,N}^F(b, M; \alpha_s(\mu_R^2), \mu_R^2, \mu_F^2) f_{a/h_1,N}(b_0^2/b^2) f_{b/h_2,N}(b_0^2/b^2). \quad (5.6)$$

To express the resummed partonic cross section \mathcal{W}_{ab} in terms of the perturbative coefficients A_c, B_c, C_{ab} , one must evaluate the parton densities at some factorization scale μ_F , which can be done by applying a QCD evolution operator which at the end of the day is related to the Altarelli-Parisi splitting functions [43, 48].

The known coefficients and functions in the power series relevant for Higgs production take the following values

$$A_c^{(1)} = C_c, \quad (5.7)$$

$$A_c^{(2)} = \frac{1}{2} C_c \left[\left(\frac{67}{18} - \frac{\pi^2}{6} \right) - \frac{5}{9} n_f \right], \quad (5.8)$$

¹The formalism used by Collin, Soper and Sterman is equivalent to the one discussed in Chapter 4, with some differences worth mentioning. The main one, is that the perturbative approach of CSS is applied directly for hadronic cross sections rather than the one used by Bozzi et al., which performs resummation at the level of partonic observables.

where $C_c = C_F$ if $c = q, \bar{q}$ and $C_c = C_A$ if $c = g$. The first orders of the B_c coefficients are given by

$$\tilde{B}_{c,N}^{(1)} = B_c^{(1)} + 2\gamma_{cc,N}, \quad (5.9)$$

with $\gamma_{cc,N}$ the parton anomalous dimension² and

$$B_q^{(1)} = B_{\bar{q}}^{(1)} = -\frac{3}{2}C_F, \quad B_g^{(1)} = -\frac{1}{6}(11C_A - 2n_f) \quad (5.10)$$

$$\tilde{B}_{c,N}^{(2)} = B_c^{(2)} - 2\beta_0 C_{cc,N}^{(1)} + 2\gamma_{cc,N}. \quad (5.11)$$

Equivalently, we can perform an inverse Mellin transformation and write the $\tilde{B}_c^{(2)}$ coefficient in z -space

$$\tilde{B}_c^{(2)}(z) = \delta(1-z)B_c^{(2)} - 2\beta_0 C_{cc}^{(1)}(z) + 2P_{cc}^{(2)}(z), \quad (5.12)$$

where $P_{cc}^{(2)}(z)$ is the second-order term of the Altarelli-Parisi splitting function $P_{cc}(z)(\alpha_s, z)$. The first orders of the C_{ab} coefficients are given by

$$C_{qg}^{(1)} = C_{\bar{q}g}^{(1)} = \frac{1}{2}z(1-z), \quad (5.13)$$

$$C_{gq}^{(1)} = C_{g\bar{q}}^{(1)} = \frac{1}{2}C_F z, \quad (5.14)$$

also expressed in z -space.

Here we discuss some existing results at NLL+LO and NNLL+NLO accuracy, for the reader to have an overall view of the behavior of the Higgs q_T distribution. By implementing equation 4.4 and 4.9 of Chapter 4, one can compute the differential cross section $d\sigma/dq_T$ at the LHC (pp collisions at $\sqrt{s} = 13$ TeV). As discussed in previous chapter, at NLL+NLO accuracy we compute $d\hat{\sigma}_{F,ab}^{(\text{res.})}$ at NLL accuracy, meaning we include the hard coefficient $\mathcal{H}_N^{(1)}$ and the functions $g_N^{(1)}$ and $g_N^{(2)}$, and then the resummed calculation is matched with $[d\sigma]_{\text{F.O.}}$ evaluated at NLO ($\mathcal{O}(\alpha_s^3)$) in the large- q_T region. The functions $g^{(1)}$ and $g^{(2)}$ of the Sudakov form factor are process independent and written in terms of the universal coefficients $A^{(1)}, A^{(2)}, \tilde{B}^{(1)}$. The flavour off-diagonal part of $\mathcal{H}_{gg \leftarrow ab,N}^{H(1)}$ is also process independent and given by

$$\mathcal{H}_{gg \leftarrow gq,N}^{H(1)} = \mathcal{H}_{gg \leftarrow qg,N}^{H(1)} = C_{gq,N}^{(1)} = \frac{1}{2(N+1)}C_F, \quad (5.15)$$

where the auxiliary scales μ_R, μ_F and the resummation scale Q are set to $\mu_R = \mu_F = Q = M_H$, and the perturbative coefficients $C_{ab,N}^{(n)}$ are exact, meaning they are not affected by the large- M_t approximation. The flavour diagonal $\mathcal{H}_{gg \leftarrow gg,N}^{H(1)}$ is instead process dependent, therefore it depends on M_t . In the large- M_t approximation it is written as

$$\mathcal{H}_{gg \leftarrow gg,N}^{H(1)} = H_g^{H(1)} + 2C_{gg,N}^{(1)} = \frac{1}{2}[(5 + \pi^2)C_A - 3C_F] = \frac{1}{2}(11 + 3\pi^2), \quad (5.16)$$

²More precisely, $\gamma_{cc,N}$ represent the N -moments of the Altarelli-Parisi splitting function.

At NNLL+NNLO, we also include the hard coefficient $\mathcal{H}_N^{(2)}$ and the function $g_N^{(3)}$ in the resummed component, and then this is matched with $[d\sigma]_{\text{F.O.}}$ evaluated at NNLO ($\mathcal{O}(\alpha_s^4)$) in the large- q_T region. The process independent function $g^{(3)}$ depends on the universal coefficients $A^{(3)}$, $\tilde{B}^{(2)}$. The scale-independent part of $\mathcal{H}_N^{H(2)}$ is not known in analytic form, yet it can be obtained by exploiting the perturbative unitarity, to extract the numerical value from the knowledge of the NNLO total cross section [71]. The scale-independent part of $\mathcal{H}_{gg\leftarrow gg,N}^{H(2)}$

$$\begin{aligned} \mathcal{H}_{gg\leftarrow gg,N}^{H(2)} \Big|_{\mu_R=\mu_F=Q=M_H} &= H_g^{H(2)} + 2C_{gg,N}^{(2)} + (C_{gg,N}^{(1)})^2 + 2H_g^{H(1)}C_{gg,N}^{(1)} \\ &= \left(\frac{19}{16} + \frac{1}{3}n_f \right) \ln \frac{M_H^2}{M_t^2} + c_N; \end{aligned} \quad (5.17)$$

where the M_t -dependent contribution on the right-hand side is obtained from the results in refs [49, 72], and c_N does not depend on M_t since the calculation is done in the large M_t approximation. We recall that the functions $g_N^{(k)}(\lambda)$ are singular when $\lambda \rightarrow 1$, a singular behavior which is related to the presence of the Landau pole in the perturbative running of $\alpha_s(q^2)$. A practical implementation of the resummation procedure requires a prescription to deal with these singularities. In our numerical study we follow the **HRes** and **HqT** codes and deform the integration contour in the complex b -space. In particular we choose the integration branches

$$b = (\cos \phi \pm i \sin \phi)t, \quad t \in \{0, \infty\} \quad (5.18)$$

In the figures 1 and 2 of [43], an example the q_T distribution of the Higgs boson is depicted, computed using the **HqT** code at NLL+NLO and NNLL+NNLO, respectively.

The q_T spectrum of the Higgs boson at NLL+NLO accuracy is shown in figure 1 of [43]. In the left-hand side, the full NLL+NLO (solid line) is compared with the LO (dashed line) at the scales $\mu_F = \mu_R = M_H$. We see that the NLO calculation, as expected, diverges at $q_T \rightarrow 0$, and the effects of the resummation are relevant below $q_T \sim 100$ GeV. In the right-hand side we show the NLL+LO band which is obtained by performing scale variations around the central value.

The q_T spectrum of the Higgs boson at NNLL+NNLO accuracy is shown in figure 2 of [43]. Again, in the left-hand side the full NNLL-NNLO (solid line) is compared with the NNLO (dashed line) at the scales $\mu_F = \mu_R = M_H$. We see that the NNLO calculation diverges now to $-\infty$ at $q_T \rightarrow 0$, with an unphysical peak which is produced by the numerical compensation of negative leading logarithmic and positive subleading logarithmic contributions. In the right-hand side we show the NLL+LO band which is obtained by performing scale variations around the central value. It is interesting to compare figures 1 and 2 of ref. [43], since the NNLL+NNLO band is smaller than the NLL+NLO one, suggesting a good convergence of the resummed expansion.

See figure 5.1 for a representation of the q_T distribution of the Higgs boson produced with **HTurbo**, where we plot the resummed and the fixed order prediction to see the behavior in the low q_T range.

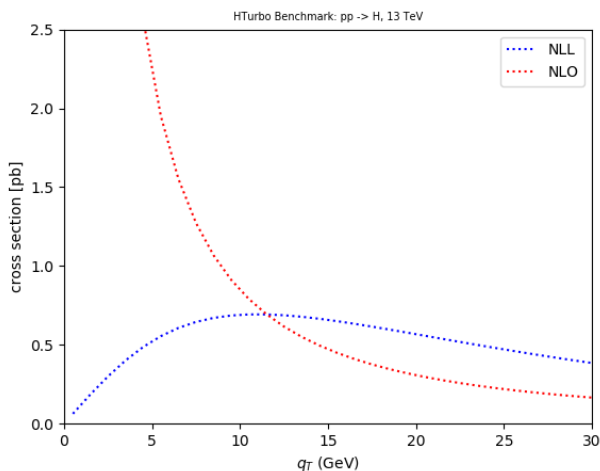


Figure 5.1: Higgs boson q_T distribution computed at NLL+NLO accuracy, together with the fixed order prediction at NLO. Both curves are computed with **HTurbo**, with full phase for a 125 Higgs boson and in the NWA approximation. By looking at this comparison we can observe how the fixed order prediction diverges at $q_T \rightarrow 0$, reason for which only a resummed result is physically reliable in the low q_T regime.

Our complete calculation of the q_T spectrum of the Higgs boson at the LHC is implemented in the numerical code **HTurbo**, which can be downloaded from

github.com/JesusUrtasun/HTurbo3,

together with some accompanying notes, and it is described with detail through the next chapter. The details about its architecture and usage are discussed in Appendix C

Part III

HTurbo numerical implementation

HTurbo numerical implementation

In this chapter we present the numerical code **HTurbo**, which provides fast and numerically precise higher order QCD predictions for Higgs boson production through gluon fusion. Arbitrary kinematical cuts can be applied in order to obtain fiducial cross sections and associated kinematical distributions. The present version of the code, available at

github.com/JesusUrtasun/HTurbo3,

reproduces the perturbative QCD expansion up to next-to-next-to-leading order combined with resummation of the large logarithmic corrections at small transverse momenta up to next-to-next-to logarithmic accuracy, and it includes the decay of the Higgs boson in a photon pair with full dependence on the final-state kinematics. Benchmark comparison with other public numerical codes is presented. Furthermore, next-to-next-to-next-to-leading logarithmic (N^3LL) resummation is implemented and discussed further on. Our results represent the first implementation of the resummation of refs [73, 74] at N^3LL for Higgs boson production.

HTurbo is written following the structure of the code **DYTurbo** [75], for the calculation of the QCD transverse-momentum resummation of Higgs cross sections up to next-to-next-to-leading logarithmic accuracy combined with the fixed-order results at next-to-next-to-leading order. We present a benchmark comparison with the predictions obtained by the numerical programs **HqT** [48], **HRes** [36], and **HNNLO** [76], all of them available at [77], for which **HTurbo** represents an improved and optimized implementation. A detailed description of the architecture and usage of **HTurbo** can be found in Appendix C

6.1 Introduction

After the discovery of the Higgs boson back in 2012, one of the main goals of the physics program at the LHC has become direct research of the electroweak symmetry breaking mechanism. Both precision measurements of the QCD and electroweak (EW) parameters, together with searches for possible deviations from the SM predictions on the Higgs sector are still under continuous discussion, specially towards the high luminosity era of the LHC [78].

Through this manuscript we focus on the production of a SM Higgs boson through the gluon fusion mechanism and its decay to a photon pair $\gamma\gamma$. The gluon fusion process $gg \rightarrow H$ is the dominant production channel at the LHC and its dynamics are driven

by the strong interactions, as already discussed during the previous chapters, and it is therefore essential to perform perturbative QCD calculations at higher orders for Higgs cross sections and associated distributions. Such task that can indeed be extremely demanding from the computational side.

The QCD radiative corrections to the total cross section have been computed up to next-to-next-to-next-to-leading order N^3LO , as we discuss further on in this chapter. Fully exclusive parton-level NNLO calculations, which include the decay of the Higgs boson, have been already implemented in the public Monte Carlo codes **HqT** [48], **HRes** [36], and **HNNLO** [76]. The cross section for H +jet boson production in gluon fusion has been computed in QCD perturbation theory at leading order $\mathcal{O}(\alpha_s^3)$, [79, 80], and at NLO in refs. [54, 55, 81]. The combination of the resummation formalism for logarithmically enhanced contributions at small q_T with fixed-order perturbative results at different levels of theoretical accuracy have been obtained following the techniques from refs. [48, 56, 62, 82]. Analogous resummed calculations have been performed by applying Soft Collinear Effective Theory methods and transverse-momentum dependent factorization [83, 84, 85]. Precise theoretical predictions with a reliable estimate of the associated uncertainties depend on several parameters and various theoretical assumptions. It is thus extremely important to develop numerical codes which allow for fast computations with small numerical uncertainties. As we discuss here, such codes already exist but they require larger and larger computation times when producing higher order predictions.

The **HTurbo** program presented in this chapter aims to provide fast and numerically precise predictions for the Higgs boson production cross sections, to be used for phenomenological applications towards the precision era of the LHC. The architecture is done by following the structure of the **DYTurbo** code, developed for the Drell-Yan lepton pair production. The enhancements in performance over the original programs are achieved by over-hauling pre-existing codes and introducing one-dimensional and multi-dimensional numerical integration techniques. The **HTurbo** program is a reimplementation of **HqT** and **HRes** programs for q_T resummation, and of the **HNNLO** program for finite-order perturbative calculations up to NNLO, which aims to facilitate the inclusion of N^3LO corrections, as we will discuss in the next chapter. The **HqT** and **HRes** programs encode the q_T resummed cross sections up to next-to-next-to-leading logarithmic (NNLL) accuracy by using the resummation formalism of refs. [43, 48]. The H +jet predictions at $\mathcal{O}(\alpha_s^3)$ and $\mathcal{O}(\alpha_s^4)$ are implemented in the **MCFM** program [86], as encoded already in **HRes** and **HNNLO**, for the full kinematic dependence of the decaying photons. Software profiling was employed to achieve code optimization.

The **HTurbo** software is based on modular C++ structure, with a few Fortran functions wrapped in and interfaced to C++. The most successful optimization strategies, leading to significant improvements in performance, were hoisting loop-invariant expressions out to loops, removing conditional statements from loops to allow the compiler perform automatic loop vectorization, and manual loop unrolling. Multi-threading is implemented within OpenMP, and through the Cuba library [87] by means of fork/wait system calls. A flexible user interface allows setting parameters of the calculation through input files and command line options, and the results are provided in the form of `.txt` files and ROOT histograms.

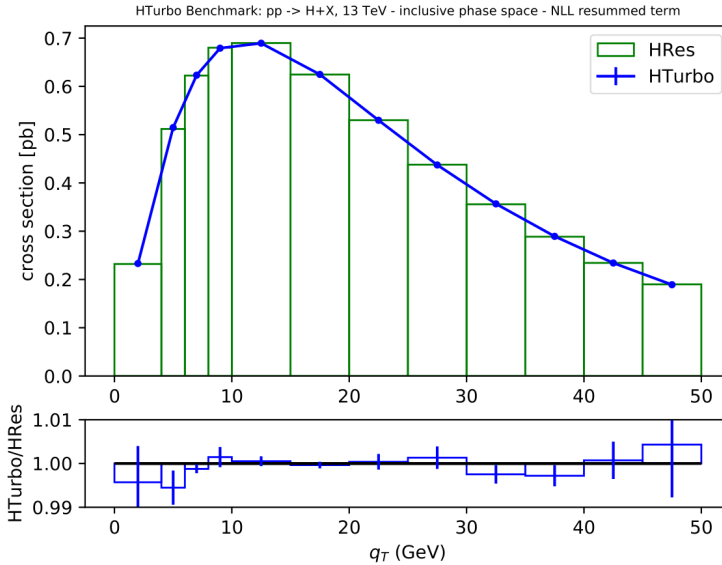


Figure 6.1: Comparison of the NLL resummed component computed with **HRes** and **HTurbo** at $\sqrt{s} = 13$ TeV as a function of the Higgs boson transverse momentum. The phase space is here totally inclusive, and the bottom panel shows ratio of **HTurbo** to **HRes** results. The comparison is performed with the NNPDF31_nlo_as_0118 PDF set.

6.2 Predictions with HTurbo

Upon integration of final-state QCD radiation, the fully-differential Higgs boson cross section is described by six kinematic variables, corresponding to the momenta of the two photons. Given the spin-0 nature of the SM Higgs boson, the fully differential cross section factorizes in two independent factors for the production and decay subprocesses of the Higgs boson. The cross section is therefore expressed as a function of the transverse momentum q_T , the rapidity y and the invariant mass m of the photon pair, and three angular variables corresponding to the polar angle θ and azimuth ϕ of the photon decay in the given boson rest frame, and to the azimuth ϕ_H of the boson in the laboratory frame. The Higgs boson is treated in the narrow-width approximation (NWA) and therefore we have $m = M_H$. Moreover, the cross section does not depend on ϕ_H , since in unpolarized hadron collisions the initial state hadrons - i.e. the incoming beams - exhibit to very good approximation azimuthal symmetry. At NLL+NLO and NNLL+NNLO, the q_T -resummed cross section for the Higgs boson production can be written as

$$d\sigma_{(N)NLL+(N)LO}^H = d\sigma_{(N)NLL}^{(\text{res})} - d\sigma_{(N)LO}^{(\text{asy})} + d\sigma_{(N)LO}^{(\text{f.o.})}, \quad (6.1)$$

where $d\sigma^{(\text{res})}$ is the resummed component of the cross section, $d\sigma^{(\text{asy})}$ is the asymptotic term - or counterterm - that represents the fixed-order expansion of $d\sigma^{(\text{res})}$, and $d\sigma^{(\text{f.o.})}$ is the H +jet finite-order cross section integrated over final-state QCD radiation. All the cross sections are differentiated with respect to q_T^2 . The resummed component $d\sigma^{(\text{res})}$ gives the dominant contribution at small q_T while the finite-order component $d\sigma^{(\text{f.o.})}$ dominates at large q_T . A consistent matching between resummed and finite compo-

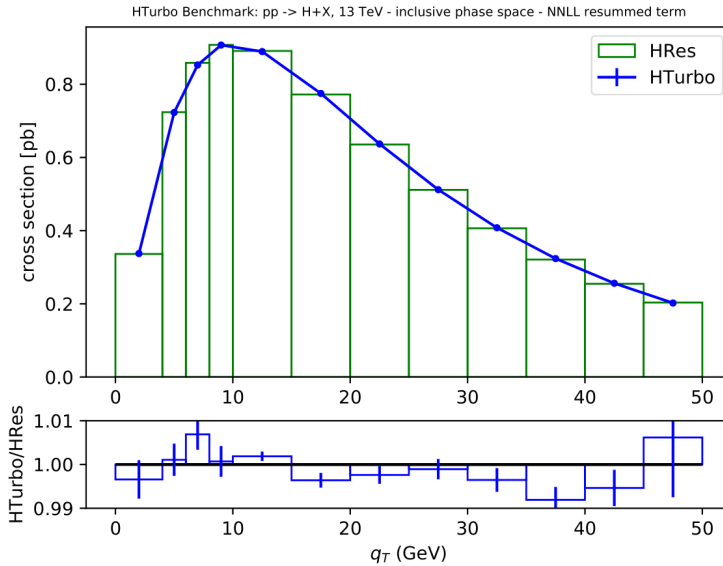


Figure 6.2: Comparison of the NNLL resummed component computed with **HRes** and **HTurbo** at $\sqrt{s} = 13$ TeV as a function of the Higgs boson transverse momentum. The phase space is here totally inclusive, and the bottom panel shows ratio of **HTurbo** to **HRes** results. The comparison is performed with the NNPDF31_nnlo_as_0118 PDF set.

nents is essential to have an accurate description of the whole q_T range. The fixed-order expansion of the resummed component, $d\sigma^{(\text{asy})}$, embodies the singular behavior of the finite-order term, providing a smooth behavior in eq. 6.1 as q_T approaches zero. The resummed component and its fixed-order expansion are given by¹

$$d\sigma_{(\text{N})\text{NLL}}^{(\text{res})} = d\hat{\sigma}_{\text{LO}}^{\text{H}} \times \mathcal{H}_{(\text{N})\text{NLO}}^{\text{H}} \times \exp\{\mathcal{G}_{(\text{N})\text{NLL}}\}, \quad (6.2)$$

$$d\sigma_{(\text{N})\text{LO}}^{(\text{asy})} = d\hat{\sigma}_{\text{LO}}^{\text{H}} \times \Sigma^{\text{H}}(q_T/Q)_{(\text{N})\text{LO}}, \quad (6.3)$$

where Q denotes the auxiliary resummation scale that is introduced in $d\sigma^{(\text{res})}$ and, consistently, in $d\sigma^{(\text{asy})}$.

The term $d\hat{\sigma}_{\text{LO}}^{\text{H}}$ is the leading-order (LO) cross section evaluated for non-vanishing values of q_T . The factor \mathcal{H}^{H} is the hard-collinear coefficient function and \mathcal{G} is the exponent of the Sudakov form factor, originally expressed in terms of the impact parameter b , the Fourier conjugate of q_T . As discussed in Chapter 4, this term embodies the resummation of the logarithmically enhanced contributions at LL, NLL, NNLL accuracy in b space. In order to parametrize non-perturbative QCD effects, the Sudakov form factor includes a non-perturbative contribution, whose simplest form is a Gaussian form factor. The b space expression of the Sudakov form factor is then evaluated in q_T space by numerically performing the inverse two-dimensional Fourier transformation (Hankel

¹The convolution with PDFs and the sum over different initial-state partonic contributions are implied in the short-hand notation of 6.2 and 6.3. Analogously, the inverse Fourier transformation from b space to q_T space is implied in 6.2.

transformation ²⁾ with respect to b . The function $\Sigma^H(q_T/Q)$ arises from the finite-order expansion of $\mathcal{H}^H \times \exp\{\mathcal{G}\}$, and it matches the singular behavior of $d\sigma^{(f.o)}$ in the region $q_T \rightarrow 0$.

An additional feature of the **HTurbo** program is the possibility of computing finite-order cross sections at LO, NLO and NNLO (without the resummation of the logarithmically enhanced contributions). At NLO and NNLO, the finite-order cross section of the Higgs boson production is computed by using the q_T -subtraction formalism [32, 33, 36], and it is expressed as the sum of three components:

$$d\sigma_{(N)NLO}^H = \mathcal{H}_{(N)NLO}^H \times d\sigma_{LO}^H + \left[d\sigma_{(N)LO}^{H+jet} - d\sigma_{(N)LO}^{CT} \right], \quad (6.4)$$

with $d\sigma_{(N)LO}^{CT}$ given by

$$d\sigma_{(N)LO}^{CT} = d\sigma_{LO}^H \times \int_0^\infty d^2q_T \Sigma_H(q_T/m)_{(N)LO}. \quad (6.5)$$

The LO cross section term $d\sigma_{LO}^H = d\hat{\sigma}_{LO}^H \delta(q_T^2)$ is evaluated at $q_T = 0$, and $d\sigma^{H+jet}$ is the H +jet cross section. ³

A unitarity constraint was needed in the resummation formalism to recover exactly the finite-order result upon integration over q_T of the full phase space matched cross section, and it leads to the following relation:

$$\int_0^\infty dq_T^2 d\sigma_{(N)NLL+(N)NLO}^{(res)} = \mathcal{H}_{(N)NLO}^H \times d\sigma_{LO}^{(res)}(0). \quad (6.6)$$

The terms $d\sigma_{(N)NLL}^{(res)}$ and $d\sigma_{(N)LO}^{(asy)}$ can be, in general, multiplied by a switching function $w(q_T, m)$ above a given q_T threshold, to the purpose of reducing the contribution of the resummed calculation in the large- q_T region, where small- q_T resummation can not improve the accuracy of the finite-order calculation. The switching function can spoil the unitarity constrain in eq. 6.6, by an amount which is smaller when the chosen q_T threshold is larger. The default choice in **HTurbo** is a Gaussian switching function. The predictions for the Higgs boson cross section are obtained by integrating over the kinematic variables of the two photons, and over additional variables related to QCD radiation, convolutions and integral transforms, as we summarize in the following sections. The integral transformations are evaluated by means of one-dimensional quadrature rules based on interpolating functions. The numerical integration over the other variables is performed with two different methods. The first one is based on the Vegas algorithm [88] as implemented in the Cuba library, and the second one employs a combination of one-dimensional and multi-dimensional numerical integrations based on interpolating functions.

The Vegas integration method is available for all terms in the resummed and fixed-order calculations, and it allows evaluating predictions for any arbitrary observable,

²For details about the integral transforms, see the Appendix A.

³More precisely, the term $d\sigma_{(N)LO}^{H+jet}$ in equation 6.4 has to be evaluated with $q_T > q_T^{cut}$, the lower integration limit in equation 6.5 has to be understood to be q_T^{cut} and the square bracket in equation 6.5 is also evaluated in the limit $q_T^{cut} \rightarrow 0$.

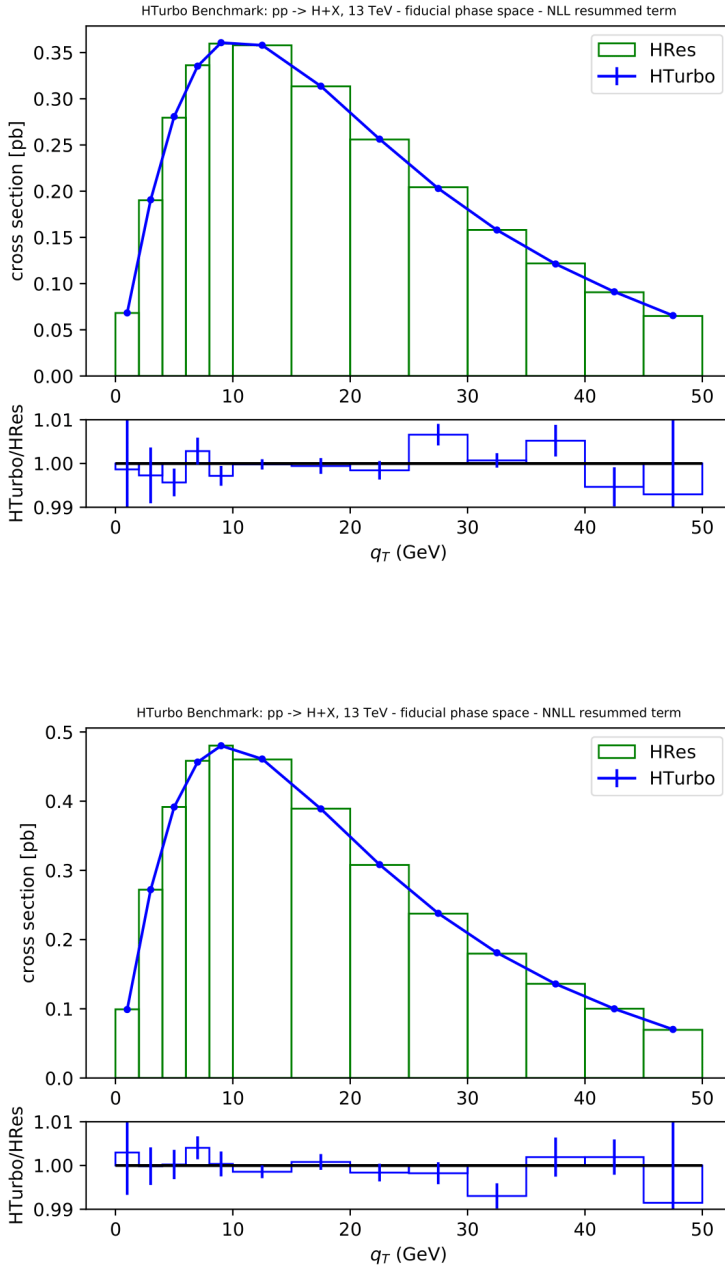


Figure 6.3: Comparison of the NLL (upper figure) and NNLL (lower figure) resummed components computed with **HRes** and **HTurbo** at $\sqrt{s} = 8$ TeV as a function of the Higgs boson transverse momentum. The Higgs boson fiducial phase space is defined by the photon transverse momentum $q_T > 20$ GeV and the lepton pseudorapidity $|\eta| < 2.4$, and the bottom panels show ratios of **HTurbo** to **HRes** results. The comparison is performed with the NNPDF31_nlo_as_0118 PDF set in the case of the NLO figure, and with the NNPDF31_nnlo_as_0118 PDF set for the NNLO figure.

for total and fiducial cross sections. The numerical integration based on interpolating functions is available for all the terms in the case of total cross sections, and for all the terms except the finite-order $\mathcal{O}(\alpha_s^2)$ in the case of fiducial cross sections. This integration method allows calculating only the cross sections as functions of q_T and y . Of these two methods, the second is more versatile, whereas the latter allows reaching relative uncertainties in the predicted cross sections below 10^{-3} in a time frame that is significantly shorter than that required by the **HRes** and **HNNLO** programs. The default values of the renormalization (μ_R), factorization (μ_F) and resummation (Q) scales are fixed to $\mu_R = \mu_F = 2Q = M_H$. The prescriptions necessary to obtain the resummed results (i.e. the switching function $w(q_T, m)$ and the prescription to avoid the Landau singularity) have been chosen following ref. [89].

6.2.1 Resummed component

The resummed component of the q_T resummed cross section in eq. 6.1 can be factorized as the product of the LO cross section $d\hat{\sigma}_{\text{LO}}^{\text{H}}$ and the term $\mathcal{W} = \mathcal{H}^{\text{H}} \times \exp\{\mathcal{G}\}$. In these two terms, only the LO cross section depends on the photon angular variables θ_l and ϕ_l . In the general case of fiducial cross sections, the integrals describing the angular dependence involve a factor Θ_k , known as the acceptance function of the kinematic requirements.

The \mathcal{W} term in 6.2 is expressed through the Sudakov form factor $\exp\{\mathcal{G}\}$ in b space, and the q_T -dependent cross section is obtained by means of a two-dimensional inverse Fourier transformation, which is expressed as a zeroth-order inverse Hankel transformation by exploiting the azimuthal symmetry of the \mathcal{W} function in the transverse plane:

$$\mathcal{W}(q_T, m, y) = \frac{m^2}{s} \int_0^\infty db \frac{b}{2} J_0(bq_T) \tilde{\mathcal{W}}(b, m, y), \quad (6.7)$$

where $\tilde{\mathcal{W}}$ is the expression of \mathcal{W} in b space, $J_0(x)$ is the zeroth-order Bessel function and s stands for the centre-of-mass energy. The integral transformation is computed by means of a double-exponential formula for numerical integration [90, 91]. The convolution with PDFs is more efficiently performed by considering double Mellin moments of the partonic functions $\hat{\mathcal{W}}_{ab}$, defined as

$$\hat{\mathcal{W}}_{ab}^{N_1, N_2} = \int_0^1 dz_1 z_1^{N_1-1} \int_0^1 dz_2 z_2^{N_2-1} \hat{\mathcal{W}}_{ab}(z_1, z_2), \quad (6.8)$$

where we have defined

$$\begin{aligned} z_{1,2} &= m/\sqrt{\hat{s}} e^{\pm\hat{y}}, \\ \hat{y} &= y - 1/2 \ln(x_1/x_2), \\ \hat{s} &= x_1 x_2 s, \end{aligned} \quad (6.9)$$

and a, b denote the initial state partonic indices. The function $\tilde{\mathcal{W}}$ is then obtained by means of a double inverse Mellin transformation

$$\tilde{\mathcal{W}}(b, m, y) = \left(\frac{1}{2\pi i} \right)^2 \int_{c-i\infty}^{c+i\infty} dN_1 x_1^{-N_1} \int_{c-i\infty}^{c+i\infty} dN_2 x_2^{-N_2} F_a^{N_1} F_b^{N_2} \hat{\mathcal{W}}_{ab}^{N_1, N_2}, \quad (6.10)$$

where $x_{1,2} = m/\sqrt{s} e^{\pm y}$, c is a real number which lies at the right of all poles of the integrand, and F_i^N , with $i = a, b$ are Mellin moments of PDFs $f_i(x)$ defined as

$$F_i(N) = \int_0^1 dx x^{N-1} f_i(x). \quad (6.11)$$

The integral transformation in 6.11 is computed by means of Gauss-Legendre quadrature, and the PDFs are evolved from the factorization scale μ_F to the scale b_0/b ⁴ using the Pegasus QCD program for the evolution of the PDFs in Mellin space [92]. To perform the Mellin inversion, it is necessary to calculate the Mellin moments $F_i(N)$ at values N along the contour of integration in the complex plane. Parametrizing the PDFs in a simple form as

$$f(x) = x^\alpha (1-x)^\beta P(x), \quad (6.12)$$

where α, β are constants and $P(x)$ is a polynomial function, Mellin moments for an arbitrary complex N can be calculated through a simple formula involving the Γ function

$$\int_0^1 dx x^\alpha (1-x)^\beta \frac{\Gamma(\alpha+1)\Gamma(\beta+1)}{\Gamma(\alpha+\beta+2)}. \quad (6.13)$$

Thanks to the analytic continuation of eq. 6.13 in the region of the complex plane with $\text{Re}(N) < 0$, when PDFs are expressed with this form the integration contour in 6.10 can be optimized by bending towards negative values of $\text{Re}(N)$, allowing for faster convergence of the inverse Mellin integral. Such a strategy is adopted in **HRes**. As a drawback, PDFs need to be parametrized as in eq. 6.12, otherwise they require an approximation which can be significantly time consuming. In **HTurbo**, the Mellin moments of the PDFs are evaluated numerically, by using Gauss-Legendre quadrature to calculate the integrals in 6.11. However these integrals can be evaluated numerically only for $\text{Re}(N) > 0$. As a consequence the integration contour of the inverse Mellin transform cannot be bent towards negative values of $\text{Re}(N)$, and a standard contour along the straight line $[c - i\infty, c + i\infty]$ is used. This procedure results in a slower convergence of the integration, but it has the great advantage of allowing usage of PDFs with arbitrary parametrization, without requiring further time consuming evaluation.

The integration over the Higgs boson rapidity, y , is factorized as follows. In the case of the total cross sections, the values of the angular integrals do not depend on y . The only dependence on the rapidity in eq. 6.10 is in the expression

$$x_1^{N_1} x_2^{N_2} = e^{-\ln(m\sqrt{s})(N_1+N_2)} e^{-y(N_1-N_2)}, \quad (6.14)$$

and the integrals of eq. 6.14 are evaluated analytically using the following relation

$$\int_{y_0}^{y_1} dy e^{-y(N_1-N_2)} = \frac{e^{-y_1(N_1-N_2)} - e^{-y_0(N_1-N_2)}}{N_1 - N_2}, \quad (6.15)$$

where y_0 and y_1 are the lower and upper y -bin boundaries. In the case $N_1 = N_2$, eq. 6.15 further simplifies to $y_1 - y_0$. When the y -bin boundaries are larger than the allowed kinematic range $|y| \leq y_{\max}$, with $y_{\max} = \ln(\sqrt{s}/m)$, eq. 6.15 simplifies to $2\pi i \delta(N_1 - N_2)$, and the double Mellin inversion is reduced to a single Mellin inversion [43, 48] by setting $N_1 = N_2 = N$. The integration over the Higgs boson transverse momentum q_T , can be

⁴Here $b_0 = 2e^{-\gamma_E}$ and $\gamma_E = 0.5772\dots$ is the Euler-Mascheroni constant.

performed analytically in the case of full-photon phase space cross sections, since the integrals over the angular variables of the photon pair do not depend on q_T , and the only term that depends on q_T is $J_0(bq_T)$ of 6.7. By using the relation

$$\int dx x J_0(x) = x J_1(x) , \quad (6.16)$$

the integration over q_T in a bin of boundaries q_T^0 and q_T^1 can be evaluated as

$$\int_{q_T^0}^{q_T^1} dq_T 2q_T \mathcal{W}(q_T, m) = \frac{m^2}{s} \int_0^\infty db [q_T^1 J_1(bq_T^1) - q_T^0 J_1(bq_T^0)] \tilde{\mathcal{W}}(b, m) . \quad (6.17)$$

Similarly to eq. 6.7, the integral of eq. 6.17 is computed by means of a double-exponential formula for numerical integration, and by performing two separate integrations corresponding to the terms $J_1(bq_T^1)$ and $J_1(bq_T^0)$. The information of the one-loop and two loop virtual corrections to the LO subprocess is contained in the \mathcal{H}^H function. In the computation of the fixed-order cross section of eq. 6.4, the \mathcal{H}^H function is evaluated in x -space, i.e. without performing a Mellin transformation, and the convolution with PDFs is performed by integrating over the variables $z_{1,2} = e^{\pm\hat{y}} m / \sqrt{\hat{s}}$. The corresponding integrals are calculated with Gauss-Legendre quadrature.

We present in figures. 6.1, 6.2 and 6.3 the results for the resummed component in a q_T range from $q_T = 0$ to $q_T = 50$ GeV, where the implemented next-to-leading and next-to-next-to-leading log calculations of **HTurbo** shows excellent numerical agreement with **HqT** and **HRes**.

6.2.2 Asymptotic term and counter-term

The asymptotic term of eq. 6.3 and the counter-term of eq. 6.5 are computed using the function $\Sigma_{\text{H}}(q_T/Q)$, which embodies the singular behavior of $d\sigma^{(\text{f.o.})}$ in the limit $q_T \rightarrow 0$. In the finite-order case the counter-term contributes at $q_T = 0$. Accordingly, the LO cross section is evaluated at $q_T = 0$, and the function $\Sigma_{\text{H}}(q'_T/Q)$ is integrated over the auxiliary variable q'_T . Meanwhile in the resummed case the asymptotic term is a function of q_T , and the LO cross section is evaluated for nonzero values of q_T . The integration over the angular variables is performed as for the resummed term, factorizing the LO cross section using the acceptance function Θ_k in the fiducial case. The function $\Sigma_{\text{H}}(q_T/Q)$ is evaluated in x -space, i.e. without performing the Mellin transformation, and the convolution with PDFs is performed by integrating over the variables $z_{1,2}$ with Gauss-Legendre quadrature. In the case of full-photon phase space cross sections, the q_T dependence of the asymptotic term and of the function $\Sigma_{\text{H}}(q_T/Q)$ is fully embodied in a set of four functions $\tilde{I}_n(q_T/Q)$ as described in Chapter 4, which are integrated with Gauss-Legendre quadrature. The integrals over the angular variables of the photon pair also depend on q_T , and the integrals

$$\int_{q_T^0}^{q_T^1} dq_T \, 2q_T \, \tilde{I}_n(q_T/Q) \, \theta_i(q_T), \quad i = 0, 1, \quad (6.18)$$

where q_T^0 and q_T^1 are the lower and upper q_T -bin boundaries, which are evaluated numerically by means of Gauss-Legendre quadrature. We present in figures. 6.4 and 6.5 results for the counterterm in a q_T range from $q_T = 0$ to $q_T = 120$ GeV.

6.2.3 Finite-order term

The real-emission corrections are embodied in the (N)NLO finite-order term of eq. 6.1 and in the H +jet term of eq. 6.4 for the resummed predictions, respectively. Since **HTurbo** provides results that are inclusive over final-state QCD radiation, the two terms are fully equivalent⁵. Two independent calculations for this term are implemented. The first calculation, based on the **HRes** and **HNNLO** codes, is fully differential with respect to the photon angular variables and the final-state QCD radiation. The second calculation, which is inclusive over the photon angles and the QCD radiation, implements the analytic result as in the **HqT** implementation. The **MCFM** implementation of the lowest-order term $d\sigma^{\text{H+jet}}$ is the most complex part of the calculation, and it can be evaluated only with the Vegas algorithm. The reason is that this NNLO calculation is based on the Catani-Seymour dipole subtraction scheme [32, 33], in which for each point in the phase space where the real radiation is evaluated, a set of counter-term dipoles is computed corresponding to various different phase-space points. As in any local subtraction procedure, the resulting integral presents discontinuities and it cannot be efficiently approximated by interpolating functions. The implementation of the analytic calculation of refs [36, 48, 76] yields to double-differential production cross sections as a function of q_T and y of the photon pair, and it is used only for cross sections inclusive over the photon decay, evaluated with numerical integration based on interpolating functions. We present in figures. 6.6 and 6.7 results for the fixed-order cross section in a q_T range from $q_T = 0$ to $q_T = 120$ GeV, where the NLO and NNLO implementations of **HTurbo** show excellent numerical agreement with **HqT** and **HRes**.

⁵Resummed predictions can be computed only inclusively with respect to the final-state QCD radiation, whereas fixed-order predictions could be evaluated differentially.

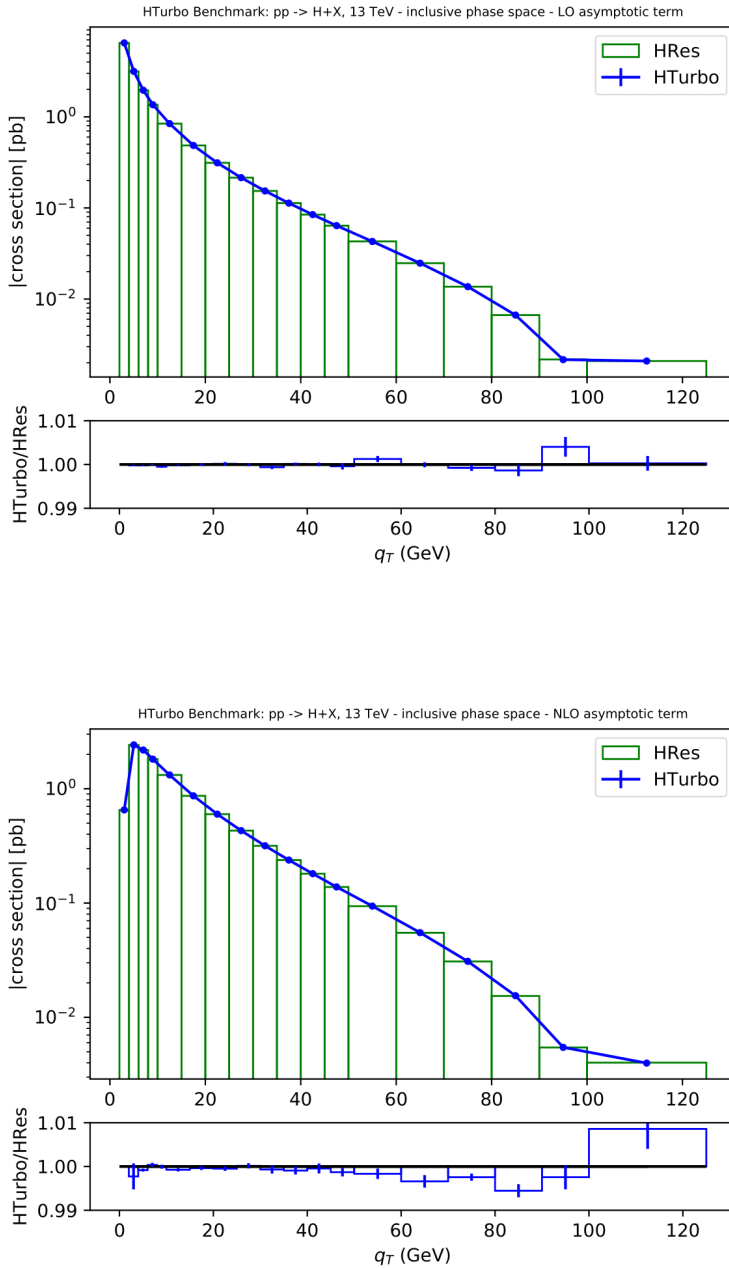


Figure 6.4: Comparison of the LO (upper figure) and NLO (lower figure) asymptotic term computed with **HRes** and **HTurbo** at $\sqrt{s} = 13$ TeV as a function of the Higgs boson transverse momentum. The phase space is here totally inclusive, and the bottom panels show ratios of **HTurbo** to **HRes** results. The comparison is performed with the `NNPDF31_nlo_as_0118` PDF set in the case of the NLO figure, and with the `NNPDF31_nnlo_as_0118` PDF set for the NNLO figure.

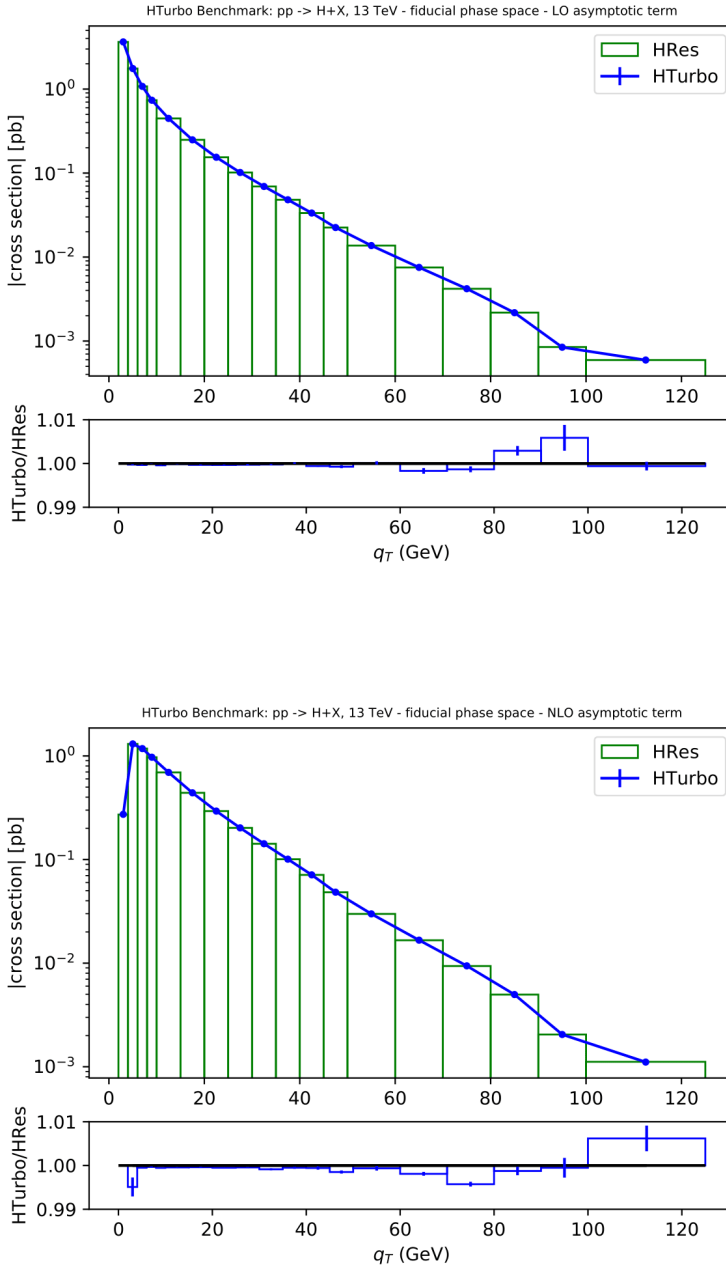


Figure 6.5: Comparison of the LO (upper figure) and NLO (lower figure) asymptotic term computed with **HRes** and **HTurbo** at $\sqrt{s} = 13$ TeV as a function of the Higgs boson transverse momentum. The Higgs boson fiducial phase space is defined by the photon transverse momentum $q_T > 20$ GeV and the lepton pseudorapidity $|\eta| < 2.4$, and the bottom panels show ratios of **HTurbo** to **HRes** results. The comparison is performed with the NNPDF31_nlo_as_0118 PDF set in the case of the NLO figure, and with the NNPDF31_nnlo_as_0118 PDF set for the NNLO figure.

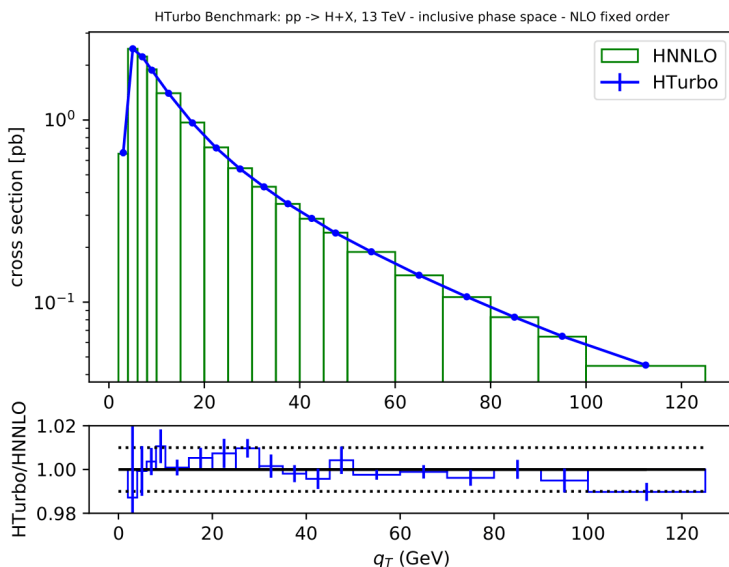
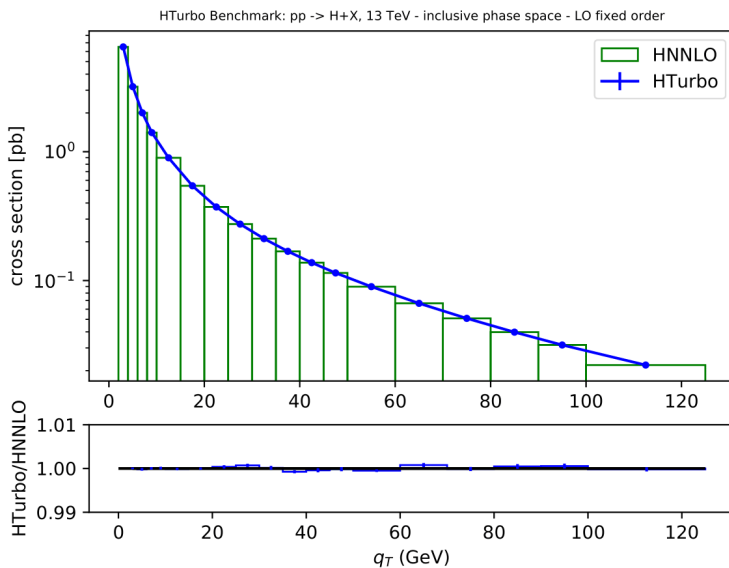


Figure 6.6: Comparison of fixed-order LO (upper figure) and NLO (lower figure) H +jet cross sections computed with **HNNLO** and **HTurbo** at $\sqrt{s} = 13$ TeV as a function of the Higgs boson transverse momentum. The phase space is here totally inclusive, and the bottom panels show ratios of **HTurbo** to **HNNLO** results. The comparison is performed with the `NNPDF31_nlo_as_0118` PDF set in the case of the NLO figure, and with the `NNPDF31_nnlo_as_0118` PDF set for the NNLO figure.

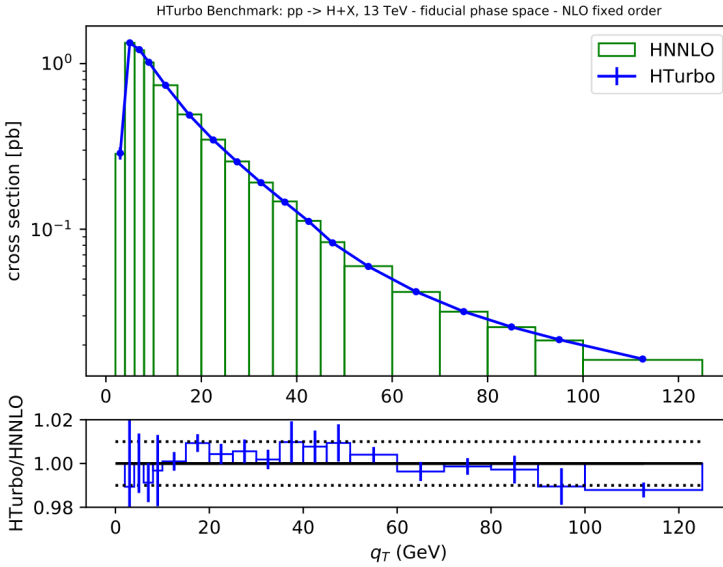
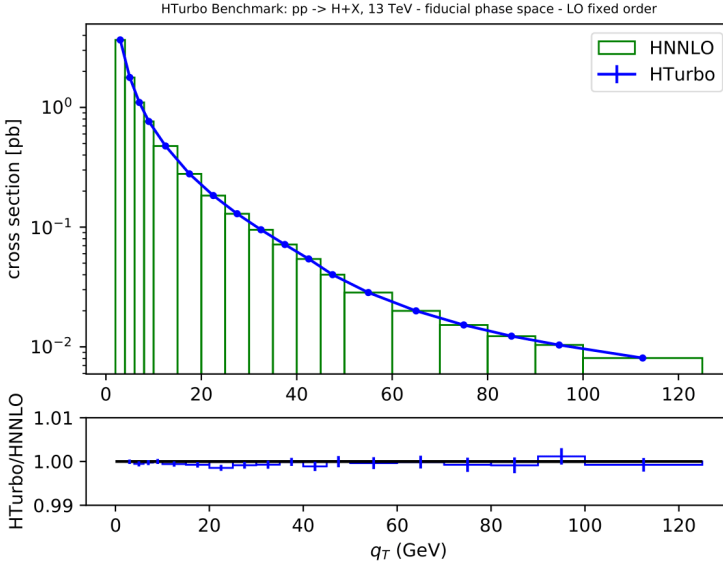


Figure 6.7: Comparison of fixed-order LO (upper figure) and NLO (lower figure) H +jet cross sections computed with **HNNLO** and **HTurbo** at $\sqrt{s} = 13$ TeV as a function of the Higgs boson transverse momentum. The Higgs boson fiducial phase space is defined by the photon transverse momentum $q_T > 20$ GeV and the lepton pseudorapidity $|\eta| < 2.4$, and the bottom panels show ratios of **HTurbo** to **HNNLO** results. The comparison is performed with the NNPDF31_nlo.as.0118 PDF set in the case of the NLO figure, and with the NNPDF31_nnlo.as.0118 PDF set for the NNLO figure.

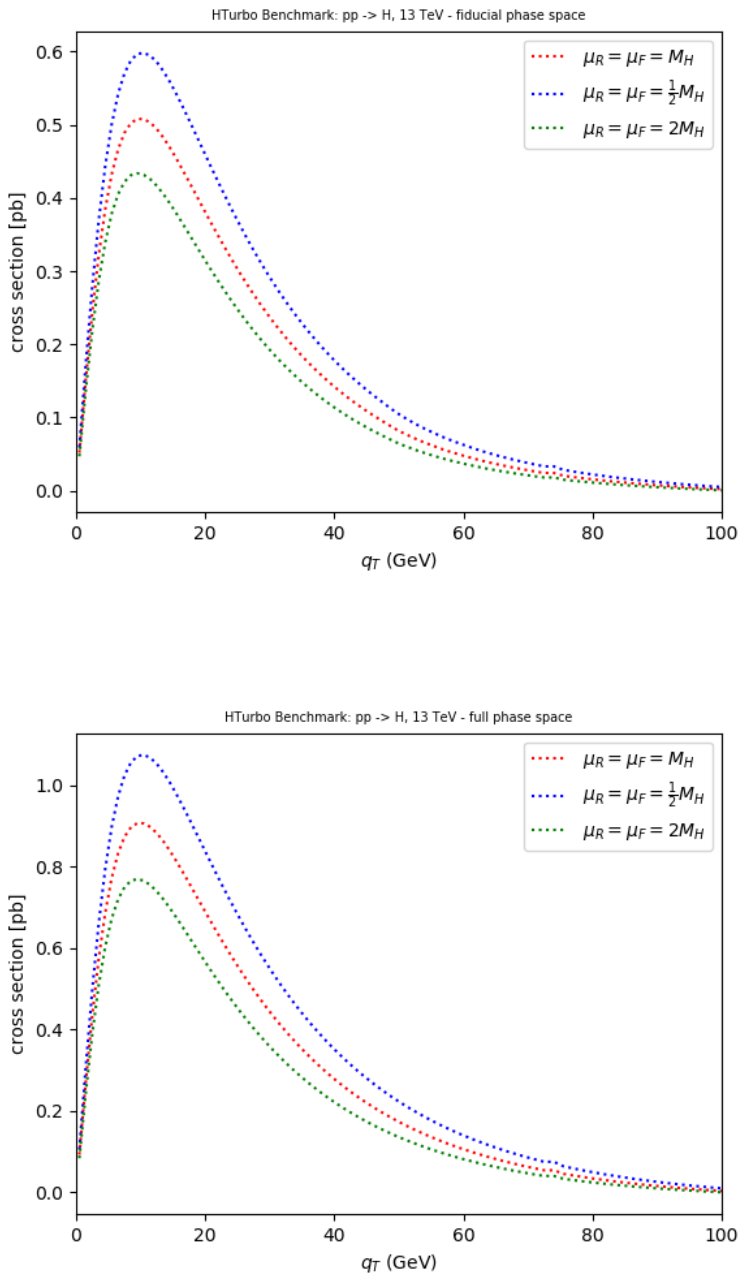


Figure 6.8: Resummed predictions with different values of the scale variations, setting μ_R and μ_F to be equal to the central value M_H , $2M_H$ and $\frac{1}{2}M_H$. In the upper figure, the Higgs boson fiducial phase space is defined by the photon transverse momentum $q_T > 20$ GeV and the lepton pseudorapidity $|\eta| < 2.4$, for a 125 GeV Higgs boson and in the NWA approximation. The comparison in the lower figure is performed in full phase space, for a 125 GeV Higgs boson and in the NWA approximation. The calculation is performed with the MSTW2008nn1o PDF set.

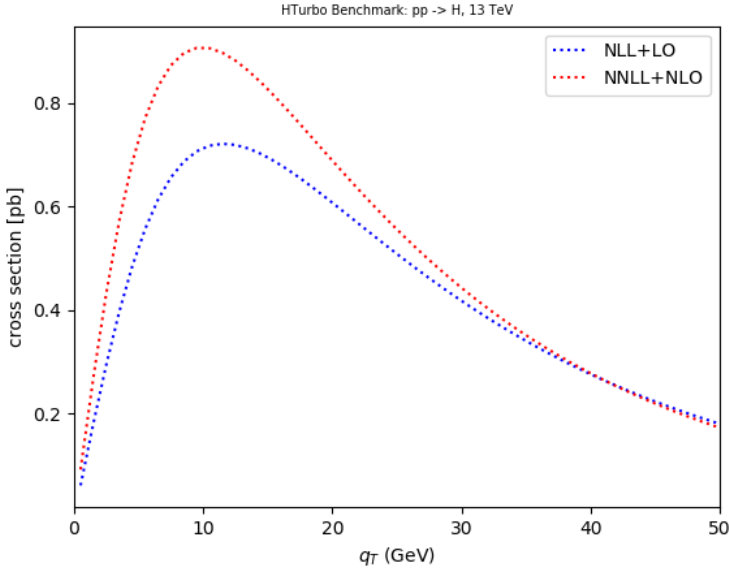


Figure 6.9: Resummed predictions for the Higgs boson q_T distribution at NLL and NNLL accuracy at $\sqrt{s} = 13$ TeV, using in both cases the `MSTW2008nnlo` PDF set. The phase space is here totally inclusive, for a 125 GeV Higgs boson and in the NWA approximation.

6.3 Tests of numerical precision

In order to validate the numerical precision of the resummed calculation, three closure tests are performed: the comparison of the fixed-order expansion of the resummed component (asymptotic term) and the finite-order term at small q_T , the comparison of the term $\mathcal{H}^H \times d\sigma_{\text{LO}}$ and the resummed upon q_T integration, and comparisons of the integration methods available in **HTurbo**, namely the Vegas algorithm and the multi-dimensional numerical integration based on interpolating functions, referred to as Gauss-Legendre quadrature integration in the plots. The numerical tests of this section are performed in full-photon phase space, using the `MSTW2008nlo` and `MSTW2008nnlo` sets for parton density functions and with default values of the QCD scales and EW parameters. As discussed on section 6.2 of this chapter, the function $d\sigma^{(\text{asy})}$ embodies the singular behavior of $d\sigma^{(\text{f.o.})}$ when $q_T \rightarrow 0$, yielding the relation

$$\lim_{Q_T \rightarrow 0} \int_0^{Q_T} (d\sigma^{(\text{f.o.})} - d\sigma^{(\text{asy})}) = 0. \quad (6.19)$$

Computing such a relation at small values of Q_T provides a stringent test of the numerical precision of the asymptotic and finite-order predictions. The double-differential cross sections $d\sigma^{(\text{asy})}$ and $d\sigma^{(\text{f.o.})}$, as functions of q_T and y , are evaluated at the fixed value $y = 0$ for proton-proton as $\sqrt{s} = 13$ TeV.

The figures below provide some benchmark results with **HRes** at NNLL+NNLO, and with **HqT** and **HNNLO** for the fixed-order at NLO and NNLO. Figure 6.8 displays the NNLL distribution for different values of the μ_R and μ_F scales.

```

/-----\
|               Fixed born |               TOTAL |
|-----+-----|
| 13.0052 +- 0.0039 e+03 (52.9ms) | 13.0052 +- 0.0039 e+03 ( 53ms) |
|-----+-----|
| 13.0052 +- 0.0039 e+03 (52.9ms) | 13.0052 +- 0.0039 e+03 ( 53ms) |
\-----/

===== Summary =====
Total cross section          13.0052 +- 0.0039 pb
Calculation time              53 milliseconds
Output file                   hturbo3_LO_BORN.dat
Result in text file           hturbo3_LO_BORN.txt
=====

```

```

***** Integration by Vegas (iteration 20) *****
*
* integral = 13006.253          accum. integral = 12994.784
* std. dev. = 36.050841       accum. std. dev = 2.9804857
* max. wt. = 0.00000
*
*****
***** chi**2/iteration = 1.399 *****

Cross section is 12994.784 +/- 2.980 fb

```

Figure 6.10: Benchmark results for the total cross section $gg \rightarrow H$ at Born level. The upper image shows the **HTurbo** output for the fixed-order only computation, which can be done by means of the quadrature integration or the Vegas algorithm, leading to a more precise predictions but with slower convergence. The lower image shows the **HNNLO** output, done by means of the quadrature integration. The phase space is here totally inclusive, for a 125 GeV Higgs boson and in the NWA approximation. The calculation is performed with the `MSTW2008nn1o` PDF set.

```

/-----\
|               Fixed born |               TOTAL |
|-----+-----|
| 22.35 +- 0.0067 e+03 (67.6ms) | 22.35 +- 0.0067 e+03 (67.7ms) |
|-----+-----|
| 22.35 +- 0.0067 e+03 (67.6ms) | 22.35 +- 0.0067 e+03 (67.7ms) |
|-----\

===== Summary =====
Total cross section          22.35 +- 0.0067          pb
Calculation time              67.7 milliseconds
Output file                   hturbo3_NLO_BORN.dat
Result in text file           hturbo3_NLO_BORN.txt
=====

***** Integration by Vegas (iteration 20) *****
*
*  integral = 22495.096          accum. integral = 22474.840
*  std. dev. = 61.480874        accum. std. dev = 5.1184296
*  max. wt. = 0.00000
*
*****
*
*          chi**2/iteration = 1.377          *****
*
Cross section is 22474.840 +/- 5.118 fb

```

Figure 6.11: Benchmark results for the total cross section $gg \rightarrow H$ at next-to-leading order corrections in α_s , meaning with one loop correction to the Born-level cross section. The upper image shows the **HTurbo** output for the fixed-order only computation, which can be done by means of the quadrature integration or the Vegas algorithm, leading to a more precise predictions but with slower convergence. The lower image shows the **HNNLO** output, done by means of the quadrature integration. The phase space is here totally inclusive, for a 125 GeV Higgs boson and in the NWA approximation. The calculation is performed with the `MSTW2008nn1o` PDF set.


```

/-----\
|               Fixed born |               TOTAL |
|-----+-----|
| 26.2003 +- 0.0076 e+03 ( 396ms) | 26.2003 +- 0.0076 e+03 ( 396ms) |
|-----+-----|
| 26.2003 +- 0.0076 e+03 ( 396ms) | 26.2003 +- 0.0076 e+03 ( 396ms) |
|-----\

===== Summary =====
Total cross section          26.2003 +- 0.0076          pb
Calculation time              396 milliseconds
Output file                   hturbo3_NNLO_BORN.dat
Result in text file           hturbo3_NNLO_BORN.txt
=====

***** Integration by Vegas (iteration 20) *****
*
*  integral   = 26283.799          accum. integral = 26253.147   *
*  std. dev.  = 71.639475         accum. std. dev = 6.0233167   *
*  max. wt.   = 0.00000          *
*
*****
chi**2/iteration = 1.323          *****

Cross section is 26253.147 +/- 6.023 fb

```

Figure 6.12: Benchmark results for the total cross section $gg \rightarrow H$ at next-to-next-to-leading order corrections in α_s , meaning with two loop corrections to the Born-level cross section. The upper image shows the **HTurbo** output for the fixed-order only computation, which can be done by means of the quadrature integration or the Vegas algorithm, leading to a more precise predictions but with slower convergence. The lower image shows the **HNNLO** output, done by means of the quadrature integration. The phase space is here totally inclusive, for a 125 GeV Higgs boson and in the NWA approximation. The calculation is performed with the `MSTW2008nnl0` PDF set.

```

-----
                Fixed born |                V+J |                TOTAL
-----+-----+-----+-----+-----+-----+-----+-----+-----
22.35 +- 0.0067 e+03 (91.5ms) | 27.139 +- 0.014 e+03 ( 13s) | 49.489 +- 0.015 e+03 ( 13.1s)
-----+-----+-----+-----+-----+-----+-----+-----+-----
22.35 +- 0.0067 e+03 (91.5ms) | 27.139 +- 0.014 e+03 ( 13s) | 49.489 +- 0.015 e+03 ( 13.1s)
-----+-----+-----+-----+-----+-----+-----+-----+-----
===== Summary =====
Total cross section          49.489 +- 0.015          pb
Calculation time              13.1              seconds
Output file                   hturbo3_NLO_VJ_qtcut_5GeV.dat
Result in text file           hturbo3_NLO_VJ_qtcut_5GeV.txt
=====

```

```

***** Integration by Vegas (iteration 20) *****
*
* integral = 27118.766          accum. integral = 27129.916
* std. dev. = 46.332364        accum. std. dev = 8.5955652
* max. wt. = 39.8112
*
***** chi**2/iteration = 1.332 *****
Cross section is 49610.653 +/- 10.017 fb

```

Figure 6.13: Benchmark results for the total cross section $gg \rightarrow H + \text{jet}$ at leading order corrections in α_s , meaning with one real (radiative) correction to the Born-level cross section. The upper image shows the **HTurbo** output for the fixed-order only computation, which can be done by means of the quadrature integration or the Vegas algorithm, leading to a more precise predictions but with slower convergence. The lower image shows the **HNNLO** output, done by means of the quadrature integration. The phase space here has a cut in $q_T = 5$ GeV for the radiated parton, for a 125 GeV Higgs boson and in NWA approximation. The radiative correction is added to the Born-level cross section to produce the total result. In the **HNNLO** code, the result of the `accumulated integral` shows the contributions of the radiative corrections, to be compared with the V+J column of **HTurbo**, while the final result `Cross section` must be compared against the `total` column of **HTurbo**. Comparing with 6.14, a larger value of the q_T^{text} leads to a smaller acceptance and hence to a smaller cross section. The calculation is performed with the `MSTW2008nnl0` PDF set.

```

-----\
Fixed born | V+J | TOTAL |
-----+-----+-----
22.35 +- 0.0067 e+03 (62.7ms) | 58.831 +- 0.033 e+03 ( 12.9s) | 81.181 +- 0.033 e+03 ( 13s) |
22.35 +- 0.0067 e+03 (62.7ms) | 58.831 +- 0.033 e+03 ( 12.9s) | 81.181 +- 0.033 e+03 ( 13s) |
-----/

===== Summary =====
Total cross section      81.181 +- 0.033      pb
Calculation time        13      seconds
Output file              hturbo3_NLO_VJ_qtcut_1GeV.dat
Result in text file      hturbo3_NLO_VJ_qtcut_1GeV.txt
=====
    
```

```

***** Integration by Vegas (iteration 20) *****
*
* integral = 58927.300      accum. integral = 58829.174      *
* std. dev. = 97.902589    accum. std. dev = 18.616272      *
* max. wt. = 383.757
*
***** chi**2/iteration = 1.160 *****
Cross section is 81309.911 +/- 19.314 fb
    
```

Figure 6.14: Benchmark results for the total cross section $gg \rightarrow H + \text{jet}$ at leading order corrections in α_s , meaning with one real (radiative) correction to the Born-level cross section. The upper image shows the **HTurbo** output for the fixed-order only computation, which can be done by means of the quadrature integration or the Vegas algorithm, leading to a more precise predictions but with slower convergence. The lower image shows the **HNNLO** output, done by means of the quadrature integration. The phase space here has a cut in $q_T = 1$ GeV for the radiated parton, for a 125 GeV Higgs boson and in NWA approximation. The radiative correction is added to the Born-level cross section to produce the total result. In the **HNNLO** code, the result of the accumulated integral shows the contributions of the radiative corrections, to be compared with the V+J column of **HTurbo**, while the final result Cross section must be compared against the total column of **HTurbo**. Comparing with 6.13, a larger value of the q_T^{text} leads to a smaller acceptance and hence to a smaller cross section. The calculation is performed with the MSTW2008nnlo PDF set.

6.4 HTurbo N³LL implementation

We will now discuss the N³LL implementation within **HTurbo**. As already stated in chapters 2 and 4, reducing the theoretical uncertainties of the SM cross sections remains one of the main motivations for the extension beyond NNLO accuracy. Extending the perturbative accuracy of QCD calculations to higher orders implies developing new methods and techniques to achieve the cancellation of infrared (IR) divergences that appear at intermediate steps of the calculations. The past few years have witnessed a great development in both NNLL accuracy for resummed predictions and NNLO subtraction prescriptions. The q_T subtraction method [36, 48, 93], the residue subtraction [94, 95], and the antenna subtraction method [96] or sector decomposition among others, have all been successfully applied for LHC phenomenology. However, in view of the impressive and continuously improving quality of the measurements performed at the LHC, even NNLO accuracy is in some cases not sufficient to match the precision of the LHC data.

This motivates the current theoretical effort to go beyond NNLO and include the next perturbative order: the next-to-next-to-next-to-leading order (N³LO). Sum rules, branching fractions [97] and deep inelastic structure functions [98] have been known to this order for quite some time. At present, the Drell-Yan and the Higgs boson production are some of the few processes for which N³LO QCD corrections have been calculated. For the Drell-Yan production, rapidity and q_T distributions at third order of the strong coupling can be found at [99, 100, 101]. In the Higgs boson case, the total production cross section in gluon fusion [102, 103] and in vector boson fusion [104] have been already computed. First steps have been taken towards more differential observables by computing several N³LO threshold expansion terms to the Higgs boson rapidity distribution in gluon fusion [105, 106]. The N³LO fixed order calculation for the Higgs boson is computed in ref. [107]

The current version of **HTurbo**, as presented in this chapter, contains the perturbative QCD expansion up to next-to-next-to-leading order combined with resummation of the large logarithmic corrections at small transverse momenta up to next-to-next-to-next-to logarithmic accuracy. The first ingredient used for building a N³LO prediction for the q_T distribution of the SM Higgs boson starts with the resummed contribution at N³LL. Recalling the discussion of Chapter 4, the resummed cross section at an arbitrary order of logarithmic accuracy is written as

$$d\sigma_{(n)\text{NLL}}^{(\text{res})} = d\hat{\sigma}_{\text{LO}}^{\text{H}} \times \mathcal{H}_{(n)\text{NLO}}^{\text{H}} \times \exp\{\mathcal{G}_{(n)\text{NLL}}\}, \quad (6.20)$$

where both Sudakov factor \mathcal{G} and hard coefficient \mathcal{H} , usually written in Mellin space as \mathcal{G}_N \mathcal{H}_N , can be expanded as perturbative series in α_s

$$\mathcal{G}_N(\alpha_s, L) = L g^{(1)}(\alpha_s L) + g^{(2)}(\alpha_s L) + \frac{\alpha_s}{\pi} g^{(3)}(\alpha_s L) + \left(\frac{\alpha_s}{\pi}\right)^2 g^{(4)}(\alpha_s L) + \dots, \quad (6.21)$$

$$\mathcal{H}_N(\alpha_s) = 1 + \alpha_s \mathcal{H}^{(1)} + \alpha_s^2 \mathcal{H}^{(2)} + \alpha_s^3 \mathcal{H}^{(3)} + \dots \quad (6.22)$$

Written in this way, from the computation side the implementation becomes quite straightforward. For each new order of logarithmic accuracy, one needs to implement higher

order contribution of \mathcal{G}_N and \mathcal{H}_N as follows:

$$\begin{aligned} \text{LL}(\sim \alpha_s^n L^{n+1}) &: g^{(1)}, \hat{\sigma}^{(0)}, \\ \text{NLL}(\sim \alpha_s^n L^n) &: g^{(2)}, \mathcal{H}^{(1)}, \\ \text{NNLL}(\sim \alpha_s^n L^{n-1}) &: g^{(3)}, \mathcal{H}^{(2)}, \\ \text{N}^3\text{LL}(\sim \alpha_s^n L^{n-1}) &: g^{(4)}, \mathcal{H}^{(3)}. \end{aligned}$$

For the computation of the $g^{(4)}$ function of the Sudakov factor, two ingredients are needed, as it can be already seen in the integral representation 4.44. Four-loop calculations are involved within the $g^{(4)}$, for which the so-called cusp and collinear anomalous dimensions are required.⁶ While the beta function of QCD determines the running of the coupling due to ultraviolet divergences, the cusp anomalous dimensions of the quark and gluon determine the leading infrared singularities of massless scattering amplitudes [108].

The phenomenological relevance of the cusp anomalous dimensions to the resummation of prominent QCD observables is well-established, considered in some cases at the next-to-next-to-next-to-leading (four-loop) logarithm level a decade ago [109, 110], but their calculation to higher orders in QCD perturbation theory is a challenging task. After the completion of the two-loop calculations, roughly twenty years elapsed before the appearance of a first analytic calculation of the three-loop cusp anomalous dimensions [111, 112] from the three-loop DGLAP splitting functions. Over the last few years, a number of approximate numerical [113, 114] and partial analytic [115, 116, 117, 118, 119] results have appeared at the four-loop level; just as for the beta function of massless QCD, now known to five-loop order after years of intensive investigation [120, 121, 122], a high degree of automation and significant computer resources enabled this progress. Up to three loops, the cusp anomalous dimensions of the quark and gluon are related to each other by the quadratic Casimir scaling principle [123, 124, 125, 126]. As discussed in [114] this no longer holds at the four-loop level, but is rather generalized to accommodate novel color structures built out of quartic Casimir operators. This generalized Casimir scaling proposal was recently contrasted by two independent theoretical studies [127, 128]. An analytic form of the four-loop QCD cusp anomalous dimensions can be found in a very recent computation [129].

The calculation of the four-loop quark and gluon cusp anomalous dimensions can be found at [74]. While no independent results of γ_4^g are immediately available, [130] provides the $\mathcal{O}(n_f^3)$ part of the four-loop virtual anomalous dimension, relating it to the so-called *eikonal* four-loop anomalous dimension, B_4^r , allowing for an alternative extraction of the first two terms of γ_4^g . In the general case,

$$\gamma_4^r = 2B_4^r + f_4^r, \quad (6.23)$$

where f_4^r represents the four-loop eikonal anomalous dimension of massless QCD. Relating f_4^g and f_4^r by Casimir scaling, one can obtain the relevant terms for γ_4^g and γ_4^r and find agreement with the relevant calculation. Indeed, the computation of the γ_4^g coefficient can be extracted from the quark one by applying the Casimir scaling [114, 127, 128] at the four-loop level. Again, for further details about the explicit calculation we refer

⁶The computations required for these contributions can be quite specific and beyond the scope of this thesis, so we provide a brief discussion and refer the reader to the recently published calculations for further details.

the reader to [74].

For the computation of the second contribution to $g^{(4)}$, recent works have applied Soft-Collinear Effective Theory (SCET) [131, 132, 133, 134, 135] to resum large logarithms in perturbative QCD using renormalization group (RG) method. For q_T resummation this has been done by a number of authors [136, 137, 138, 139, 140, 141]. For transverse-momentum observables, the relevant momentum modes in light-cone coordinate for fields in the effective theory are soft $p_s \sim Q(\lambda, \lambda, \lambda)$, collinear $p_c \sim Q(\lambda^2, 1, \lambda)$ and anti-collinear $p_{\bar{c}} \sim Q(1, \lambda^2, \lambda)$, where $\lambda \sim q_T/Q$ is a power counting parameter. The corresponding effective theory is SCET_{II}. An important feature of SCET_{II} is that soft and collinear modes live on the same hyperbola of virtuality⁷, $p_s^2 \sim p_c^2 \sim p_{\bar{c}}^2 \sim \lambda^2 Q^2$. Besides the usual large logarithms of ratio between hard scale Q and soft scale λQ , there are also large rapidity separations between soft, collinear, and anti-collinear modes which need to be resummed. In the CSS formalism, the resummation of large q_T logarithms is controlled by two anomalous dimension

$$A[\alpha_s(\mu)] = \sum_{i=1}^{\infty} a_s^i A_i, \quad (6.24)$$

$$B[\alpha_s(\mu)] = \sum_{i=1}^{\infty} a_s^i B_i. \quad (6.25)$$

It is straightforward to express these anomalous dimension in terms of the anomalous dimension in SCET_{II}, see e.g. ref. [142, 143]. In particular, we obtain the B_i anomalous dimensions in the original CSS scheme through to three-loops

$$B_1 = \gamma_0^v - \gamma_0^r, \quad (6.26)$$

$$B_2 = \gamma_1^v - \gamma_1^r + \beta_0 c_1^v, \quad (6.27)$$

$$B_3 = \gamma_2^v - \gamma_2^r + \beta_1 c_1^v + 2\beta_0 \left(c_2^v - \frac{1}{2} (c_1^v)^2 \right), \quad (6.28)$$

where the γ^v is the anomalous dimension of hard function results matching QCD onto SCET_{II}, and the c^v factor stands for the scale-dependent terms of the hard matching. For the Drell-Yan they can be extracted from the quark and gluon form factors [144, 145, 146], and for the Higgs case they can also be extracted from the effective coupling of the Higgs boson to gluons [147]. The exact numbers for the Drell-Yan and Higgs boson production, as they can be found in the **HTurbo** implementation of the Sudakov $g^{(4)}$, can be found in ref. [73], where the formalism of [139] and [140] is used.

The Hard coefficients up to NNLO can be found in [148] and [149], respectively for the vector boson and Higgs boson cases. The implementation of such coefficients at N³LO is still work in progress in the current version of **HTurbo**, and it will be needed towards the full N³LL+N³LO prediction. We present in fig. 6.16 a comparison of the resummed predictions for the Higgs boson q_T distribution at NLL, NNLL and N³LL accuracy, with the Sudakov form factor now computed up to N³LL accuracy, including the $g^{(4)}$ function. The smaller difference between the NNLL and N³LL curves suggest a good convergence of the perturbative expansion.

⁷Again, for the details of the calculation we refer the reader to [73].

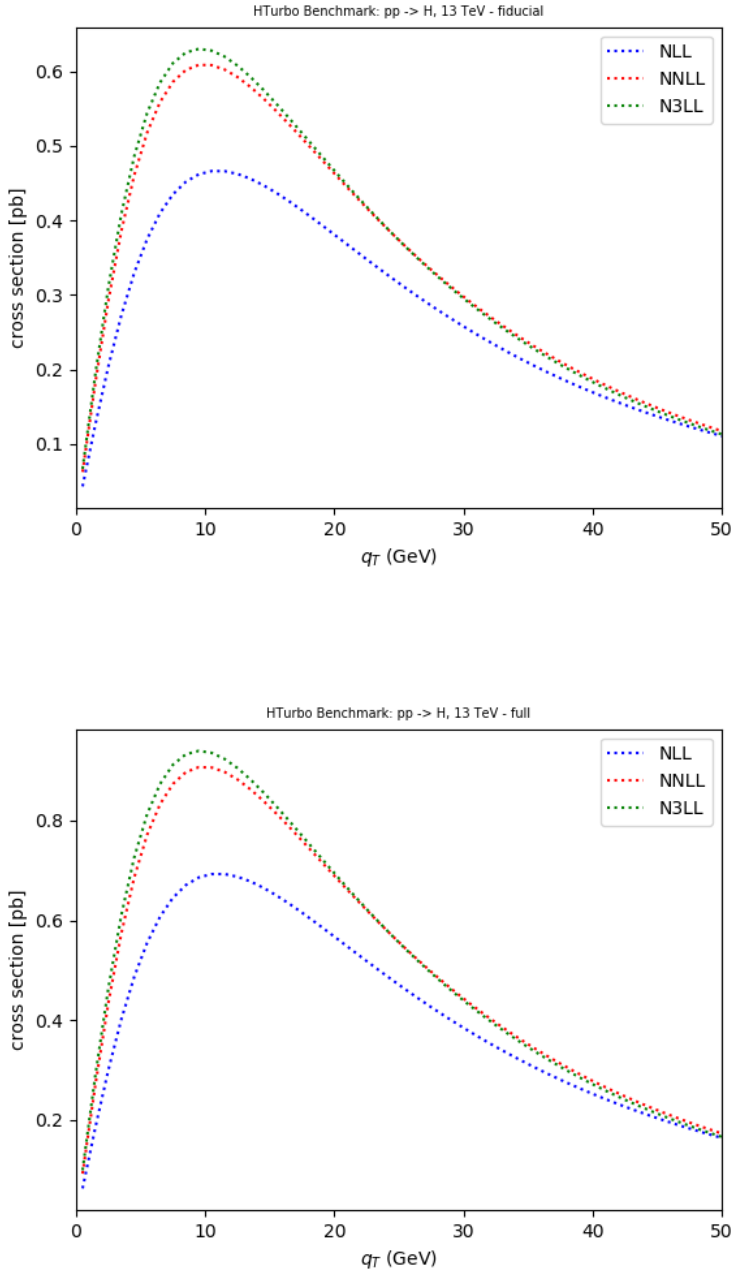


Figure 6.16: Comparison of the resummed predictions for the Higgs boson q_T distribution at NLL, NNLL and N^3LL accuracy, using in all cases the `MSTW2008nn1o` PDF set. The upper image shows the computation with the Higgs boson fiducial phase space defined by the photon transverse momentum $q_T > 20$ GeV and the lepton pseudorapidity $|\eta| < 2.4$, and for the lower image it is totally inclusive. The Sudakov form factor is now computed including the $g^{(4)}$ function, by following [73] and [74]. The computation of the hard coefficients at N^3LO is still to be implemented, while the calculation is already available at [107]. The smaller difference between the NNLL and N^3LL curves suggest a good convergence of the perturbative expansion.

Conclusions

As mentioned at the very beginning of this thesis, the main goal of theoretical high energy physics could just be phrased as trying to accurately describe the fundamental interactions among the elementary particles. An attempt to reduce all natural phenomena to a set of basic rules and laws which, at least in principle, can quantitatively reproduce and predict experimental observations. The main argument of this thesis is Quantum Chromodynamics (QCD), the sector of the Standard Model (SM) describing the strong interactions, meaning the interactions between quarks and gluons. Finally heading towards the precision era of the Large Hadron Collider (LHC), it is crucial to have very accurate theoretical predictions of what is expected by the SM, at least as accurate as precise the detection and measurement techniques, in order to be able to distinguish possible deviation from the expectations with the maximal significance.

Cross-sections in high energy physics are typically computed using perturbation theory, which provides a very powerful set of tools to predict observable quantities from a Quantum Field Theory (QFT). However, there are situations in which a truncation of the series is of no meaning, and then only a resummed result is reliable. This is a situation that quite often appears in QCD, and hence one of the main problems addressed in this thesis. A cross-section generally depends on many energy scales, and the dependence is typically in the form of logarithmic ratios of energies. In some kinematical regimes, when two of such scales become very different to each other, these logs become large and the coefficients of the perturbative series are significantly enhanced, making the standard perturbative approach unreliable. Then, the entire series of these enhanced terms has to be resummed in order to have an accurate prediction for the observable.

Hence, as described through chapters 2 and 4, resummation of the large logarithmic contributions originating from incomplete cancellation of soft and collinear divergences between real and virtual diagrams is crucial for QCD. The transverse-momentum distribution of generic high-mass color-neutral systems (Drell-Yan lepton pair, Higgs boson, etc.) produced in hadron collisions is of great interest since the early days of QCD, and it requires both precise predictions at higher orders, together with fast numerical implementations to reach the required accuracy within short computation times.

We present a novel numerical code, **HTurbo**, which provides fast and numerically precise predictions for Higgs boson production through gluon fusion, the dominant production channel at the LHC. Arbitrary kinematical cuts can be applied in order to obtain

fiducial cross sections and associated kinematical distributions. The present version of the code, available at

github.com/JesusUrtasun/HTurbo3,

contains the resummation of the large logarithmic corrections up to next-to-next-to-next-to-leading logarithmic (N^3LL) accuracy combined with the perturbative QCD expansion up to next-to-next-to-next-to leading order (NNLO). It also includes the decay of the Higgs boson in a photon pair with full dependence on the final-state kinematics.

The predictions produced by **HTurbo** combine the resummation formalism for logarithmically enhanced contributions at small q_T with fixed-order perturbative results at different levels of theoretical accuracy. The implementation of resummation up to N^3LL follows the techniques of Bozzi et al. [43, 48], and for the computation of the fixed-order cross sections we apply the q_T -subtraction formalism [32, 33, 36], as discussed through chapters 2 and 4 of this thesis.

HTurbo is implemented following the structure of the numerical code **DYTurbo** [75], developed by S. Camarda for the calculation of the QCD transverse-momentum resummation of the Drell-Yan cross sections up to NNLL accuracy combined with the fixed-order results at NNLO, and later extended to contain the N^3LL+N^3LO contribution [101].

We present a benchmark comparison with the predictions obtained by the numerical programs **HqT** [48], **HRes** [36], and **HNNLO** [76], all of them available at [77], for which **HTurbo** represents an improved and optimized implementation. The current architecture of **HTurbo** is built such that it allows for a straightforward implementation of the N^3LL , and it sets the first implementation of the resummation of refs [73, 74] at N^3LL for Higgs boson production. A detailed description of the code performance and benchmark results is presented in Chapter 6, while the architecture and usage of **HTurbo** can be found in Appendix C

The enhancement in performance over previous programs is achieved by code optimization, by factorizing the cross section into production and decay variables, and with the usage of numerical integration based on interpolating functions. The benchmark comparison with the predictions obtained by the **HqT**, **HRes** and **HNNLO** shows excellent numerical agreement. The great reduction of computing time for performing cross-section calculations opens new possibilities for Higgs processes at the LHC, and also opens the possibility of searches for physics beyond the SM.

The N^3LL prediction as depicted in figure 6.16 of the last chapter of this thesis sets the first implementation of the resummation of refs [73, 74] at N^3LL for Higgs boson production.

List of Publications

As of Jesús Urtasun Elizari,

Publications in preparation

Higgs boson production at the LHC: fast and precise predictions in QCD at higher orders
Jesús Urtasun, Giancarlo Ferrera, Stefano Camarda, Leandro Cieri, 2022

Higgs boson production at the LHC: q_T resummation at N^3LL and fiducial cross section at N^3LO
Jesús Urtasun, Giancarlo Ferrera, Stefano Camarda, Leandro Cieri, 2022

Publications in conference proceedings

Towards hardware acceleration for parton densities estimation
arxiv.org/abs/1909.10547 [150]

Machine Learning for the determination of Parton Distribution Functions
indico.ifae.es/event/645/

Gaussian processes for the estimation of theory uncertainties
agenda.infn.it/event/23656/contributions/120309/

Appendices

Integral transformations

A.1 Fourier-Bessel transformation

The multidimensional Fourier transformation of a generic function $g(\mathbf{x})$ is defined as

$$g(\mathbf{b}) \equiv \mathcal{F}[g(\mathbf{x})] \equiv \frac{1}{(2\pi)^{n/2}} \int_{\mathbb{R}^n} d^n \mathbf{x} g(\mathbf{x}) e^{-i\mathbf{b}\cdot\mathbf{x}}, \quad (\text{A.1})$$

where we distinguish between the function in direct and Fourier space just by the name of the argument¹.

The inverse Fourier transformation is given by

$$g(\mathbf{x}) \equiv \mathcal{F}^{-1}[g(\mathbf{b})] \equiv \frac{1}{(2\pi)^{n/2}} \int_{\mathbb{R}^n} d^n \mathbf{b} g(\mathbf{b}) e^{i\mathbf{b}\cdot\mathbf{x}}. \quad (\text{A.2})$$

Given the the symmetry that usually appears in collider phenomenology, usually one has to deal with central functions in \mathbb{R}^n . Therefore it is very convenient to express such integral transformations with respect to the radial variable \mathbf{r}

$$g(x_1, \dots, x_n) \equiv g(\mathbf{r}).$$

In such cases, the Fourier transform in eq. A.1 can be simplified

$$g(\mathbf{b}) \equiv \mathcal{F}[g(\mathbf{r})] = \frac{1}{(2\pi)^{n/2}} \int_{\mathbb{R}^n} d^n \mathbf{x} g(\mathbf{r}) e^{-i\mathbf{b}\cdot\mathbf{x}} \quad (\text{A.3})$$

$$= b^{1-\frac{n}{2}} \int_{\mathbb{R}^n} dr r r^{\frac{n}{2}-1} f(r) J_{\frac{n}{2}-1}(br), \quad (\text{A.4})$$

where $J_{\frac{n}{2}-1}(rb)$ is Bessel function of order $\frac{n}{2} - 1$, and b and r stand for the modulus of \mathbf{b} and \mathbf{r} . Due to angular symmetry, the inverse transformation can be obtained simply by switching b with r .

The case $n = 2$ is particularly important in literature, and it is usually referred to as the *Hankel* transformation

$$g(\mathbf{b}) \equiv \mathcal{H}[g(\mathbf{r})] = \int_0^\infty dr r J_0(br) g(r), \quad (\text{A.5})$$

$$g(\mathbf{r}) \equiv \mathcal{H}^{-1}[g(\mathbf{b})] = \int_0^\infty db b J_0(br) g(b), \quad (\text{A.6})$$

¹For the purpose of this thesis, we can identify the direct space \mathbf{x} with the \mathbf{q}_T of a given physical state. Then, the Fourier conjugate variable \mathbf{b} will be no other than the impact parameter.

A.2 Laplace transformation

The Laplace transformation of a generic function $g(t)$ is given by

$$g(s) \equiv \mathcal{L}[g(t)] = \int_0^{\infty} dt g(t) e^{-st}, \quad (\text{A.1})$$

where, again, we distinguish the Laplace transformed function from the original one just by the conjugate argument s .

If the function $g(s)$ is well defined, then it is free of singularities for $\text{Re}(s) > c$, being c some numerical value depending on $g(t)$. Indeed, in order for the Laplace transform to converge, the function $g(t)$ can grow at most as e^{ct} as $t \rightarrow \infty$, case in which the transformed function $g(s)$ is free of singularities for $\text{Re}(s) > c$.

The inverse transformation is given by

$$g(t) \equiv \mathcal{L}^{-1}[g(s)] = \frac{1}{2\pi i} \int_{c_0-i\infty}^{c_0+i\infty} ds g(s) e^{st}, \quad (\text{A.2})$$

for some contour c_0 such that $c_0 > c$ and $\text{Re}s > c$. The proof is quite trivial:

$$\begin{aligned} \frac{1}{2\pi i} \int_{c_0-i\infty}^{c_0+i\infty} ds g(s) e^{st} &= \int_0^{\infty} dt' g(t') \frac{1}{2\pi i} \int_{c_0-i\infty}^{c_0+i\infty} ds e^{s(t-t')} \\ &= \int_0^{\infty} dt' g(t') \delta(t-t') \\ &= \begin{cases} g(t) & \text{if } t \geq 0 \\ 0 & \text{if } t < 0. \end{cases} \end{aligned} \quad (\text{A.3})$$

Note that, if we had taken a bilateral transformation, i.e. with lower limit $-\infty$, the inverse transform A.2 would have reproduced $g(t)$ in the whole range $-\infty < t < \infty$. Hence, the Laplace transformation in A.1 should be referred to as *unilateral* Laplace transformation, and it is suitable for functions defined only in $t > 0$, while the bilateral one works for functions defined everywhere.

If $g(t)$ is real, then $g(s)$ is a real function, i.e. it satisfies

$$g(s^*) = (g(s))^* \quad (\text{A.4})$$

for the complex conjugated variable s^* . This rule can immediately verified from the definition of the Laplace transform in A.1.

A.3 Mellin transformation

When a function $g(z)$ is defined in the range $0 < z < 1$, which is actually quite common in QCD and collider phenomenology, and fits most of the cases discussed in this thesis, we can decide to take a Laplace transformation with respect to the variable $z = e^{-t}$. The resulting transform is the so-called *Mellin transformation*;

$$g(N) \equiv \mathcal{M}[g(z)] \equiv \int_0^1 dz z^{N-1} g(z), \quad (\text{A.1})$$

And its inverse transformation is given by

$$g(z) \equiv \mathcal{M}^{-1}[g(N)] \equiv \frac{1}{2\pi i} \int_{N_0-i\infty}^{N_0+i\infty} dN z^{-N} g(N), \quad (\text{A.2})$$

where N_0 must be greater than the real part of the rightmost singularity (which must exist, because again $g(N)$ has a convergent abscissa). The integration contour can be deformed at will, provided that it does not cross any singularity. In other words, all singularities must be at the left of the contour. Being $z < 1$, a typical deformation scheme consists in giving a phase to the upper and lower parts of the integration path in such a way that the real part of N is negative, and increasing as its absolute value goes to infinity. As a particular example, when $g(N)$ is a real function we can perform the following manipulations

$$\begin{aligned} g(z) &= \frac{1}{2\pi i} \int_{N_0-i\infty}^{N_0+i\infty} dN z^{-N} g(N) \\ &= \frac{1}{\pi} \text{Im} \int_{N_0}^{N_0+i\infty} dN z^{-N} g(N) \\ &= \frac{1}{\pi} \int_0^\infty dt \text{Im}[(i-\varepsilon)z^{-N_0-(i-\varepsilon)t} g(N_0+(i-\varepsilon)t)] \\ &= \frac{x^{-N_0}}{\pi} \int_0^\infty du \text{Im} \left[\frac{\varepsilon-i}{\log z} e^{(i-\varepsilon)u} g \left(N_0 - (i-\varepsilon) \frac{u}{\log z} \right) \right] \end{aligned} \quad (\text{A.3})$$

where in the last two steps we have deformed the integration contour according to $N = N_0 + (i-\varepsilon)t$, $\varepsilon > 0$, to guarantee numerical convergence.

We write here some properties of the Mellin transformation

$$\begin{aligned} \text{Shift operation} \quad & \mathcal{M}[z^c g(z)] = g(N+c) \\ \text{Scale change} \quad & \mathcal{M}[g(az)\Theta(a-z)] = \int_0^a dz z^{N-1} g(az) = a^N \int_0^1 dt t^{N-1} g(t) = a^N g(N) \\ \text{Logarithmic derivative} \quad & \mathcal{M}[\ln^k(g(N))] = \frac{\partial^k}{\partial \varepsilon^k} \mathcal{M}[(g(N))^\varepsilon] = \frac{\partial^k}{\partial \varepsilon^k} \mathcal{G}(N, \varepsilon) \end{aligned} \quad (\text{A.4})$$

with usually \mathcal{G} called *generating function* of $g(z)$.

B.1 Euler Gamma and related functions

The base function of this group is the Euler Gamma function $\Gamma(z)$, which arises as an extension of the factorial function to complex numbers. It is defined for all complex numbers except the non-positive integers. Derived by Daniel Bernoulli, for any complex number with positive real part $\text{Re}(z) > 0$, the Euler Gamma is defined by

$$\Gamma(z) \equiv \int_0^{\infty} dt e^{-t} t^{z-1} . \quad (\text{B.1})$$

It is a real function, meaning that it satisfies

$$\Gamma(z^*) = (\Gamma(z))^* , \quad (\text{B.2})$$

and in particular

$$\text{Im } \Gamma(z) = 0 \text{ for } z \in \mathbb{R} . \quad (\text{B.3})$$

Integrating by parts, it is easy to show that $\Gamma(z)$ satisfies the following recursive relation;

$$\Gamma(z+1) = z\Gamma(z) . \quad (\text{B.4})$$

Then, knowing that $\Gamma(1) = 1$, we have for $z \in \mathbb{N}$ that

$$\Gamma(n+1) = n! , \quad (\text{B.5})$$

extending the factorial to complex values.

Note that equation B.4 in reverse allows to analytically extend the Gamma function to the whole complex plane, apart from singular points. Indeed, the Gamma function has poles in the negative integers. More precisely, for $n \in \mathbb{N}$, $\Gamma(-n)$ has a simple pole with residue

$$\text{Res}_{z=-n}\Gamma(z) = \frac{(-1)^n}{n!} , \quad (\text{B.6})$$

and around such poles the Gamma function satisfies the expansion

$$\Gamma(z-n) = \frac{(-1)^n}{n!} \left[\frac{1}{z} + \psi(n+1) + \mathcal{O}(z) \right] , \quad (\text{B.7})$$

where ψ stands for the PolyGamma function ψ_0 .

An important property satisfied by the Gamma function is the so-called Euler *reflection formula*

$$\Gamma(z)\Gamma(1-z) = \frac{\pi}{\sin(\pi z)}, \quad (\text{B.8})$$

which is useful to relate the region of convergence of the integral in eq. B.1 with the region $\text{Re}(z) < 0$.

At large $|z|$, for $|\arg z| < \pi$, the Gamma function has the asymptotic expansion

$$\Gamma(z) = e^{-z} z^{z-\frac{1}{2}} \sqrt{2\pi} \left[1 + \frac{1}{12z} + \frac{1}{288z^2} + \dots \right], \quad (\text{B.9})$$

which reduces to the well known Stirling approximation keeping only the first term. One should keep in mind that the Stirling approximation is very precise also for small values of z . For instance, in the Stirling approximation we have

$$\Gamma(2) = 0.96\dots \quad (\text{B.10})$$

which is very close to the exact value $\Gamma(2) = 2$.

Logarithmic derivatives of the Gamma function lead to another species of very important functions, the so-called PolyGamma functions of order k

$$\psi_k(z) \equiv \frac{d^{(k+1)}}{dz^{(k+1)}} \ln \Gamma(z), \quad (\text{B.11})$$

with the first order derivative

$$\psi_0(z) \equiv \frac{d}{dz} \ln \Gamma(z), \quad (\text{B.12})$$

is commonly identified as the *original* PolyGamma function, or DiGamma function. From the recursion property of the Euler Gamma B.4 it follows that

$$\psi_0(z+1) = \psi_0(1) + 1 + \frac{1}{2} + \frac{1}{3} + \dots + \frac{1}{n}. \quad (\text{B.13})$$

The value of $\psi_0(-1)$ is called the Euler-Mascheroni constant, and its numerical value is given by

$$\gamma_E \equiv -\psi_1 = 0.577216\dots \quad (\text{B.14})$$

For the case of higher order derivatives, From the recursion property of the Euler Gamma B.4 one can derive the recursion formula for a k -th order PolyGamma,

$$\psi_n(z+1) \equiv \psi_n(z) + n!(-1)^n \frac{1}{z^{n+1}}. \quad (\text{B.15})$$

As a last note, let's comment the behavior of the PolyGamma functions at large $|z|$. At large values of $|z|$ with $\arg z < \pi$, only $\psi_0(z)$ is divergent

$$\psi(z+1) \sim \ln z + \mathcal{O}\left(\frac{1}{z}\right). \quad (\text{B.16})$$

while all the PolyGammas coming from higher order derivatives, ψ_n with $n > 1$, vanish as $1/z^n$.

B.2 Riemann zeta function

A commonly appearing function in the context of resummation is the so-called Riemann zeta function. Being first studied by Euler in the context of real numbers, it was Riemann who extended the definition to complex analysis, and established the famous relation between its zeros and the distribution of prime numbers.

The Riemann zeta function is defined by the series

$$\zeta(s) = \sum_{n=1}^{\infty} n^{-s} = \frac{1}{1^s} + \frac{1}{2^s} + \frac{1}{3^s} + \dots, \quad \text{if } \operatorname{Re}(s) > 1. \quad (\text{B.1})$$

The series converges for $\operatorname{Re}(s) > 1$, but the function can be analytically extended to the whole complex plane, apart from $s = 1$, where it reduces to the divergent harmonic series. The analytic continuation is based of the reflection formula

$$\zeta(1-s) = 2(2\pi)^{-s} \cos\left(\frac{\pi s}{2}\right) \Gamma(s) \zeta(s). \quad (\text{B.2})$$

In particular, one can relate the zeta function for values of its argument less than 1 to the zeta function at values when the series B.1 converges.

For positive integers $s = n > 0$, one finds two cases: when $n = 2j + 1$ is odd, the cosine vanishes and we get

$$\zeta(-2j) = 0, \quad j \in \mathbb{N}, j > 0, \quad (\text{B.3})$$

while when $n = 2j$ is even, we have

$$\zeta(1-2j) = \frac{2(2j-1)!}{(2\pi)^{2j}} \zeta(2j), \quad j \in \mathbb{N}, j > 0, \quad (\text{B.4})$$

The Riemann zeta function has the following integral representation

$$\zeta(s) = \frac{1}{\Gamma(s)} \int_0^{\infty} dt \frac{t^{s-1}}{e^t - 1}. \quad (\text{B.5})$$

By expanding the denominator as a geometric series and exchanging the integral and the sum we get back the series definition B.1.

Special values of $\zeta(s)$ are

$$\begin{aligned} \zeta(-1) &= -\frac{1}{12} \\ \zeta(0) &= \frac{1}{2} \\ \zeta(1/2) &= \frac{1}{2} \\ \zeta(2) &= \frac{\pi^2}{6} \\ \zeta(4) &= \frac{\pi^4}{90} \end{aligned}$$

And they are usually labeled as

$$\zeta_k \equiv \zeta(k). \quad (\text{B.6})$$

B.3 Bessel function

Bessel functions, first defined by the mathematician Daniel Bernoulli and then generalized by Friedrich Bessel, arise as canonical solutions $y(x)$ of the Bessel's differential equation

$$x \frac{d^2 y}{dx^2} + x \frac{dy}{dx} + (x^2 - \alpha^2)y = 0, \quad (\text{B.1})$$

for an arbitrary complex number α , which is usually denoted as the *order* of the Bessel function.

Since B.1 is a second-order differential equation, there must be two linearly independent solutions, respectively known as the Bessel functions of first kind and second kind. Real values of the order α define Bessel functions of the first kind J_{α_s} , and Bessel functions of the second kind $Y_{\alpha}(x)$. The difference between them is that $J_{\alpha}(x)$ always vanishes for $x = 0$ and it is a single-valued function, while $Y_{\alpha}(x)$ diverges at the origin and it is a multi-valued function.

Bessel functions of the first kind, labeled as $J_{\alpha}(x)$, are solutions of the Bessel's differential equation with an integer α . For a positive integer α , Bessel functions of the first kind are finite at the origin $x = 0$, while for negative integers they diverge as x approaches zero. It is possible to express them as a series expansion around $x = 0$, which can be found by applying the Frobenius method;

$$J_{\alpha}(x) = \sum_{m=0}^{\infty} \frac{(-1)^m}{m! \Gamma(m + \alpha + 1)} \left(\frac{x}{2}\right)^{2m+\alpha}, \quad (\text{B.2})$$

where Γ is the Euler gamma function as defined in B.1. For non-integer values of α , the functions J_{α} and $J_{-\alpha}$ are linearly independent, and hence they are the two solutions for the Bessel equation.

The Bessel functions of second kind¹, denoted by $Y_{\alpha}(x)$, are multivalued functions that have a singularity at the origin $x = 0$. For non-integer α , $Y_{\alpha}(x)$ is related to $J_{\alpha}(x)$ by

$$Y_{\alpha}(x) = \frac{J_{\alpha}(x) \cos(\alpha\pi) - J_{-\alpha}(x)}{\sin(\alpha\pi)}. \quad (\text{B.3})$$

In the case of integer order n , the function is defined by taking the limit as the non-integer α tends to n

$$Y_n(x) = \lim_{\alpha \rightarrow n} Y_{\alpha}(x) \quad (\text{B.4})$$

Both Bessel functions are commonly given in the form of the integral representation

$$J_{\alpha}(x) = \frac{1}{\pi} \int_0^{\pi} d\tau \cos(\alpha\tau - x \sin(\tau)) - \frac{\sin(\alpha x)}{\pi} \int_0^{\infty} dt e^{-x \sinh(t) - \alpha t}, \quad (\text{B.5})$$

$$Y_{\alpha}(x) = \frac{1}{\pi} \int_0^{\pi} d\tau \sin(x \sin(\tau) - \alpha\tau) - \frac{1}{\pi} \int_0^{\infty} dt e^{-x \sinh(t)} (e^{-\alpha t} \cos(\alpha\pi) + e^{\alpha t}), \quad (\text{B.6})$$

¹The second kind functions are sometimes also called Weber functions, as they were introduced by H.M. Weber, and also Neumann functions after Carl Neumann.

B.4 Plus distribution

The plus distributions arise in the context of cancellation of soft and collinear divergences, and they are defined as

$$\int_0^1 dz [f(z)]_+ g(z) = \int_0^1 dz f(z) [g(z) - g(1)]. \quad (\text{B.1})$$

Formally, the plus distribution $[f(z)]_+$ following from the definition above is given by

$$[f(z)]_+ = f(z) - \delta(1-z) \int_0^\infty dz f(z), \quad (\text{B.2})$$

but, if $f(z)$ diverges as $z \rightarrow 1$, this expression needs to be written in a regularized form

$$[f(z)]_+ = \lim_{\eta \rightarrow 0^+} \left[\Theta(1-\eta-z) f(z) - \delta(1-z) \int_0^{1-\eta} dz f(z) \right], \quad (\text{B.3})$$

where the limit $\eta \rightarrow 0^+$ is intended to be performed *after* the integration over the test function $g(z)$.

The plus distribution as defined in B.1 regularizes functions which diverge as $z \rightarrow 1$, in the sense that the integral over any test function $g(z)$ remains finite. In particular, the usual logarithms

$$\frac{\log^k(1-z)}{1-z} \quad (\text{B.4})$$

are properly regularized.

Some useful relations can be derived from the definition. For instance, if $g(z)$ is a regular function as $z \rightarrow 1$, then

$$[g(z)f(z)]_+ = g(z)[f(z)]_+ - \delta(1-z) \int_0^y dy g(y)[f(y)]_+, \quad (\text{B.5})$$

$$g(z)[f(z)]_+ = g(1)[f(z)]_+ - [g(z) - g(1)]f(z), \quad (\text{B.6})$$

where in the last term of the second line the plus distribution is no longer needed since $g(z) - g(1)$ regularizes $f(z)$.

In our particular case, we are resumming the logarithmic the logarithmic contributions contained in $d\hat{\sigma}_{F_{ab}}^{(\text{res.})}$, which are plus distributions of the type

$$\left[\frac{\alpha_s^n}{q_T^2} \ln^m \left(\frac{M^2}{q_T^2} \right) \right]_+, \quad (\text{B.7})$$

being M the hard scale of a given process and q_T the transverse momentum of the particle produced. It is natural hence to require that these resummed terms give a vanishing contribution to the total cross section, leading to a finite result upon integration over q_T .

HTurbo architecture and usage

C.1 The structure of HTurbo

Since the **HTurbo** code can seem over complicated at first sight, inheriting routines and subprocesses from **HqT**, **HRes** and **HNNLO**, together with the **MCFM** code and all the ones already implemented for the Drell-Yan computation within **DYTurbo**¹, we present here the main parts that implement the resummed, counterterm and finite-order contributions for the Higgs boson production. We will describe first the architecture of **HTurbo** from the computational side, then a small section dedicated to the repository from which the results can be obtained and benchmarked with **HRes**, **HqT** and **HNNLO**.

1. The `src` directory implements the integration rules for the different components, together with the most fundamental parts of the code such as reading the parameters from the input card, and the storing/linking instructions from the different codes implemented
 - The `src/settings.C` file stores the information from the runcard and sets the active terms for the different contributions (resummed, counterterm, finite), the phase space generation, and the integration rules (quadrature, Vegas, etc).
 - The `src/resintegr.C` file performs the integration of the resummed contribution.
 - The `src/ctintegr.C` file performs the integration of the counterterm.
 - The `src/finintegr.C` file performs the integration of the fixed-order.
2. The `input` directory contains all the runcards. In the runcard one can set the active contributions for the calculation (`doBorn = True/False`, `doCT = True/False`, `doVJ = True/False`), the phase space cuts as well as the histogram for the output file, as well as the integration algorithm, accuracy settings or parallelization for faster performance. The runcards
 - `input/process_RES.01.in`, `input/process_RES.02.in`
 - `input/process_CT.01.in` `input/process_CT.02.in`
 - `input/process_FO.01.in` `input/process_FO.02.in`

¹**HTurbo** follows the architecture of the **DYTurbo**, written by S. Camarda for the purpose of computing the Drell-Yan cross sections. **HTurbo** represents an optimized implementation of **HRes**, **HqT** and **HNNLO** in the same way **DYTurbo** implemented the optimized version of **DYRes** and **DYqT** and **DYNNLO**, and it is contained now within the same framework.

- are already set to reproduce the benchmark results for the resummed component, counterterm and fixed-order expansion. There are already some default input cards labeled as `default.in` for the user to try various computations.
3. The `born` directory implements the leading order integration for computing the Born-level cross section. The calculation is done in `born/loint.C` file, while coefficients for the higher order corrections are taken from the `resum`, `dyres` and `src` directories.
 4. The `resum` directory includes all files needed for the resummed calculation, while the integration running on top are in the `src` directory.
 - The `resum/mesq.C` implements the LO amplitude section for the Higgs production via gluon fusion.
 - The `resum/mellint.C` is where the collinear hard coefficients, the exponentiation of the C'_{ab} coefficients and the Sudakov form factor are joined to produce the resummed integrand.
 - The `resum/sudakovff.C` contains the implementation of the Sudakov form factor.
 - The `resum/hcoeff.C` and `resum/hcoefficients.C` contain the implementation of the hard collinear coefficients.
 - The `resum/expc.C` contains the exponentiation of the C_{ab} coefficients.
 5. The `counterterm` directory includes all files needed for the counterterm calculation, while the integrations running on top are in the `src` directory.
 - The `counterterm/ctint.C` implements the C++ version of the fixed-order expansion of the resummed cross section, producing the Σ functions together with the leading, next-to-leading and next-to-next-to-leading contributions.
 - The `counterterm/countint.C` implements the Fortran fixed-order expansion of the resummed cross section, producing the Σ function together with the leading, next-to-leading and next-to-next-to-leading contributions.
 - The `counterterm/qtint.C` implements the integration of the counterterm and the leading logarithmic contributions.
 6. The `vjet` directory includes all files needed for the leading-order finite-order calculation, while the next-to-leading require the virtual and real contributions with are inherited from `integrand`s. The integrations running on top are in the `src` directory.
 - The `vjet/vjoint.C` implements the LO integration for the H +jet cross section, by means of the Gauss-Legendre quadrature and with the Vegas algorithm.
 - The `vjet/virtint.f` implements the virtual+real contribution to the NLO H +jet cross section, by means of the Vegas algorithm.
 - The `vjet/realint.f` implements the double real contribution to the NLO H +jet cross section, by means of the Vegas algorithm.
 7. The `mcfm` directory includes all matrix amplitudes needed for the resummed and finite-order calculations.

A flexible user interface allows setting parameters of the calculation through input files and command line options. Arbitrary kinematical cuts, modifications of the SM parameters or setting the rapidity and transverse distribution ranges can be done directly in the input card. The results are provided in the form of `.txt` files and `ROOT` histograms.

Here we write the basic steps for downloading, compiling and running the working version of the code. For the purpose of performing calculations the user just need to compile using the instructions that can already be found in the original version of **DYTurbo**

<https://dyturbo.hepforge.org/>

forge page. The runcards needed for performing a computation are already set with default values inside the `input` directory implements the integration directory.

```
autoreconf -i;
./configure --enable-root --enable-Ofast
make -j 4
make install
```

Run with the default input card

```
cp input/default.in input/process.in;
./bin/dyturbo input/process.in
```

C.2 Benchmark results

For the purpose of producing benchmark results and comparing the predictions done by **HTurbo** with other codes, the following repository is available

[github/JesusUrtasun/HTurbo3.check_codes](https://github.com/JesusUrtasun/HTurbo3.check_codes),

where we store the output files produced by **HTurbo**, **HqT**, **HRes**, and **HNNLO**, together with the `Python` scripts for the benchmark and comparison plots.

1. The `check_codes` directory contains the `Python` scripts that reproduce all benchmark plots.
 - The `check_codes/check_hturbo_qt_all_orders.py` performs the comparison of the resummed distribution **HTurbo** and **HqT** at LL, NLL and NNLL accuracy.
 - The `check_codes/check_hturbo3.py` performs the comparison of the counterterm and fixed-order distribution of **HTurbo**, **HqT**, **HRes** and **HNNLO**.
 - The `check_codes/check_hturbo_figures.py` is devoted to reproduce the figures used for this thesis.
2. The `input` directory contains all output data files from **HTurbo**, **HqT**, **HRes**, and **HNNLO**, which are used directly as input for the `Python` plotter scripts. `input/hturbo3` directory, `input/hqt`, `input/hres` directory, `input/hnnlo` directory, are the only ones used for the figures of this thesis.

List of Figures

1.1	Title and part of the abstract of the 1951 paper [10] (published in 1952) in which the existence of the Δ^{++} baryon was deduced, based on data from Sachs and Steinberger at Columbia [11] and from Anderson, Fermi, Nagle et al. at Chicago [12, 13]. See also memoir by Nagle [14].	5
1.2	Illustration of the three crossings of the interaction of a lepton current (black) with a quark current (red) via an intermediate photon or Z boson, with the corresponding colour factors.	6
1.3	Illustration of a qqg vertex in QCD, before summing/averaging over colours: a gluon in a state represented by λ^1 interacts with quarks in the states ψ_{qR} and ψ_{qG} .	8
1.4	Illustration of a ggg vertex in QCD, before summing/averaging over colours: interaction between gluons in states $\lambda^2, \lambda^4, \lambda^6$ represented by the structure constant f^{246} .	8
1.5	Trace relations for t matrices (convention-independent). Other useful relations of the QCD generators and Casimir operators can be found in [1] [3]	8
1.6	Structure constants of SU(3)	9
1.7	Vacuum polarization loops in photon propagator at higher orders.	10
1.8	Vacuum polarization loops in photon propagator, expressed as geometric series.	10
1.9	Result of the photon propagator after summing the geometric series.	11
1.10	Extract of the prize announcement for D.Gross, H.Politzer, F.Wilczek in 2004.	12
1.11	QCD running coupling at different energy scales, taken from [17, 18].	13
2.1	Representation of the partonic fluctuations inside a hadron.	16
2.2	Representation of the parton distributions for the different quark flavours and the gluon, as a function of the momentum fraction x , probed at a given transfer momentum Q^2 . On the right-hand side, the PDFs are scaled at a higher value of $Q^2 = 10^4$ GeV, and hence the dependence with x differs from the one probed at $Q^2 = 10$ GeV. Extracted from and MSTW 2008 PDF dataset.	19

- 2.3 Coefficients of the perturbative series in LO calculations. On the left, F production at LO. On the right, $F + 2$ jet at LO, with half-shaded boxes illustrating the restriction to the region of phase space with exactly 2 resolved jets. The total power of α_s for each coefficient is given by $n = k + l$. 20
- 2.4 Coefficients of the perturbative series in NLO calculations. On the left, F production at NLO. On the right, $F + 1$ jet at NLO, with half-shaded boxes illustrating the restriction to the region of phase space with exactly 1 resolved jet. The total power of α_s for each coefficient is given by $n = k + l$. 21
- 2.5 Coefficients of the perturbative series in NNLO calculations. The total power of α_s for each coefficient is given by $n = k + l$. Green shading represents the full perturbative coefficient at the respective $k + l$. 22
- 2.6 Representation of the first order real correction to the $\gamma \rightarrow q\bar{q}$. Now the phase space differs from the one in the process $\sigma(e^+e^- \rightarrow q\bar{q})$, due to the extra parton in the final state. This process $\sigma(e^+e^- \rightarrow q\bar{q}g)$ will reduce to the $\sigma(e^+e^- \rightarrow q\bar{q})$ in the IR limit, when the radiated gluon is either infinitely soft or collinear. 23
- 2.7 Representation of the first order virtual corrections to the $\gamma \rightarrow q\bar{q}$. The kinematics are the same than $\sigma(e^+e^- \rightarrow q\bar{q})$ Born level, given the loop nature of the radiated gluon. 24
- 2.8 Single real gluon emission from a general process. A parton with momentum p splits into a gluon with fraction $(1 - z)p$, and the scaled parton remains with zp . On the left-hand side, radiation comes from the final state, as we dealt with in the example of α_s corrections to e^+e^- annihilation. On the right-hand side, the same radiation takes place before the hard interactions, and hence it will be described by initial state parton showers or directly by PDF evolution. 26
- 3.1 Representation of a collision at the LHC. From the two proton beams, partons with fraction of energy x_1 and x_2 interact at a partonic center of mass energy $\sqrt{\hat{s}} = (x_1p_1 + x_2p_2)^2$ 30
- 3.2 Cross sections for different processes at the LHC. As expected, processes for which more data is available have smaller statistical uncertainty, while the theory error remains even for such cases. Therefore, producing accurate predictions becomes a main task for theoreticians specially towards the high precision era of the LHC. 31
- 3.3 Representation of a Deep Inelastic Scattering (DIS) process, where a lepton with momentum k scatters with a hadron of momentum p . The hard interaction, represented by the green blob, takes place between a highly virtual photon of momentum q , and the partons inside the hadron. Perturbative QCD is here applied to calculate higher corrections such and virtual and real emissions. 33
- 3.4 Representation of a Drell-Yan lepton pair production process. Two partons scatter from the hadrons h_1 and h_2 with respective momenta z_1p_1 and z_2p_2 , and undergo the hard interaction to produce a virtual vector boson. The product of the interaction will eventually decay in a lepton pair with energies k_1 and k_2 , that will be measured in the detector. 36
- 3.5 Feynman diagram representation of the dominant production channels for the Higgs boson at the LHC. The kinematics are the same as in the Drell-Yan process depicted in Figure 3.4. 39

- 3.6 Higgs boson couplings to fermions and gauge bosons and the Higgs self-couplings in the Standard Model. The normalization factors of the Feynman rules are also displayed. 40
- 4.1 Representation of a hadronic collision as the one described by formula 4.1. Two hadrons h_1 and h_2 with momenta p_1 and p_2 produce some final-state system F , accompanied by an arbitrary and undetected final state X . 46
- 4.2 Representation of a hard interaction where the final state F is produced with some transverse momentum with respect to the beam axis. Unbalanced cancellation when dealing with such exclusive final states will lead to logarithmic enhancements dominating the cross section. 47
- 4.3 Table representing logarithmic enhancements of the type $L = \ln M^2 b^2$ appearing at different orders. All these contributions will be absorbed inside the Sudakov form factor $\exp\{\mathcal{G}\}$. 48
- 5.1 Higgs boson q_T distribution computed at NLL+NLO accuracy, together with the fixed order prediction at NLO. Both curves are computed with **HTurbo**, with full phase for a 125 Higgs boson and in the NWA approximation. By looking at this comparison we can observe how the fixed order prediction diverges at $q_T \rightarrow 0$, reason for which only a resummed result is physically reliable in the low q_T regime. 63
- 6.1 Comparison of the NLL resummed component computed with **HRes** and **HTurbo** at $\sqrt{s} = 13$ TeV as a function of the Higgs boson transverse momentum. The phase space is here totally inclusive, and the bottom panel shows ratio of **HTurbo** to **HRes** results. The comparison is performed with the NNPDF31_nlo_as_0118 PDF set. 69
- 6.2 Comparison of the NNLL resummed component computed with **HRes** and **HTurbo** at $\sqrt{s} = 13$ TeV as a function of the Higgs boson transverse momentum. The phase space is here totally inclusive, and the bottom panel shows ratio of **HTurbo** to **HRes** results. The comparison is performed with the NNPDF31_nnlo_as_0118 PDF set. 70
- 6.3 Comparison of the NLL (upper figure) and NNLL (lower figure) resummed components computed with **HRes** and **HTurbo** at $\sqrt{s} = 8$ TeV as a function of the Higgs boson transverse momentum. The Higgs boson fiducial phase space is defined by the photon transverse momentum $q_T > 20$ GeV and the lepton pseudorapidity $|\eta| < 2.4$, and the bottom panels show ratios of **HTurbo** to **HRes** results. The comparison is performed with the NNPDF31_nlo_as_0118 PDF set in the case of the NLO figure, and with the NNPDF31_nnlo_as_0118 PDF set for the NNLO figure. 72
- 6.4 Comparison of the LO (upper figure) and NLO (lower figure) asymptotic term computed with **HRes** and **HTurbo** at $\sqrt{s} = 13$ TeV as a function of the Higgs boson transverse momentum. The phase space is here totally inclusive, and the bottom panels show ratios of **HTurbo** to **HRes** results. The comparison is performed with the NNPDF31_nlo_as_0118 PDF set in the case of the NLO figure, and with the NNPDF31_nnlo_as_0118 PDF set for the NNLO figure. 77

- 6.5 Comparison of the LO (upper figure) and NLO (lower figure) asymptotic term computed with **HRes** and **HTurbo** at $\sqrt{s} = 13$ TeV as a function of the Higgs boson transverse momentum. The Higgs boson fiducial phase space is defined by the photon transverse momentum $q_T > 20$ GeV and the lepton pseudorapidity $|\eta| < 2.4$, and the bottom panels show ratios of **HTurbo** to **HRes** results. The comparison is performed with the `NNPDF31_nlo_as_0118` PDF set in the case of the NLO figure, and with the `NNPDF31_nnlo_as_0118` PDF set for the NNLO figure. 78
- 6.6 Comparison of fixed-order LO (upper figure) and NLO (lower figure) H +jet cross sections computed with **HNNLO** and **HTurbo** at $\sqrt{s} = 13$ TeV as a function of the Higgs boson transverse momentum. The phase space is here totally inclusive, and the bottom panels show ratios of **HTurbo** to **HNNLO** results. The comparison is performed with the `NNPDF31_nlo_as_0118` PDF set in the case of the NLO figure, and with the `NNPDF31_nnlo_as_0118` PDF set for the NNLO figure. 79
- 6.7 Comparison of fixed-order LO (upper figure) and NLO (lower figure) H +jet cross sections computed with **HNNLO** and **HTurbo** at $\sqrt{s} = 13$ TeV as a function of the Higgs boson transverse momentum. The Higgs boson fiducial phase space is defined by the photon transverse momentum $q_T > 20$ GeV and the lepton pseudorapidity $|\eta| < 2.4$, and the bottom panels show ratios of **HTurbo** to **HNNLO** results. The comparison is performed with the `NNPDF31_nlo_as_0118` PDF set in the case of the NLO figure, and with the `NNPDF31_nnlo_as_0118` PDF set for the NNLO figure. 80
- 6.8 Resummed predictions with different values of the scale variations, setting μ_R and μ_F to be equal to the central value M_H , $2M_H$ and $\frac{1}{2}M_H$. In the upper figure, the Higgs boson fiducial phase space is defined by the photon transverse momentum $q_T > 20$ GeV and the lepton pseudorapidity $|\eta| < 2.4$, for a 125 GeV Higgs boson and in the NWA approximation. The comparison in the lower figure is performed in full phase space, for a 125 GeV Higgs boson and in the NWA approximation. The calculation is performed with the `MSTW2008nnlo` PDF set. 81
- 6.9 Resummed predictions for the Higgs boson q_T distribution at NLL and NNLL accuracy at $\sqrt{s} = 13$ TeV, using in both cases the `MSTW2008nnlo` PDF set. The phase space is here totally inclusive, for a 125 GeV Higgs boson and in the NWA approximation. 82
- 6.10 Benchmark results for the total cross section $gg \rightarrow H$ at Born level. The upper image shows the **HTurbo** output for the fixed-order only computation, which can be done by means of the quadrature integration or the Vegas algorithm, leading to a more precise predictions but with slower convergence. The lower image shows the **HNNLO** output, done by means of the quadrature integration. The phase space is here totally inclusive, for a 125 GeV Higgs boson and in the NWA approximation. The calculation is performed with the `MSTW2008nnlo` PDF set. 83

6.11 Benchmark results for the total cross section $gg \rightarrow H$ at next-to-leading order corrections in α_s , meaning with one loop correction to the Born-level cross section. The upper image shows the **HTurbo** output for the fixed-order only computation, which can be done by means of the quadrature integration or the Vegas algorithm, leading to a more precise predictions but with slower convergence. The lower image shows the **HNNLO** output, done by means of the quadrature integration. The phase space is here totally inclusive, for a 125 GeV Higgs boson and in the NWA approximation. The calculation is performed with the `MSTW2008nnlo` PDF set.

84

6.12 Benchmark results for the total cross section $gg \rightarrow H$ at next-to-next-to-leading order corrections in α_s , meaning with two loop corrections to the Born-level cross section. The upper image shows the **HTurbo** output for the fixed-order only computation, which can be done by means of the quadrature integration or the Vegas algorithm, leading to a more precise predictions but with slower convergence. The lower image shows the **HNNLO** output, done by means of the quadrature integration. The phase space is here totally inclusive, for a 125 GeV Higgs boson and in the NWA approximation. The calculation is performed with the `MSTW2008nnlo` PDF set.

85

6.13 Benchmark results for the total cross section $gg \rightarrow H+\text{jet}$ at leading order corrections in α_s , meaning with one real (radiative) correction to the Born-level cross section. The upper image shows the **HTurbo** output for the fixed-order only computation, which can be done by means of the quadrature integration or the Vegas algorithm, leading to a more precise predictions but with slower convergence. The lower image shows the **HNNLO** output, done by means of the quadrature integration. The phase space here has a cut in $q_T = 5$ GeV for the radiated parton, for a 125 GeV Higgs boson and in NWA approximation. The radiative correction is added to the Born-level cross section to produce the total result. In the **HNNLO** code, the result of the accumulated integral shows the contributions of the radiative corrections, to be compared with the `V+J` column of **HTurbo**, while the final result `Cross section` must be compared against the `total` column of **HTurbo**. Comparing with 6.14, a larger value of the q_T^{ext} leads to a smaller acceptance and hence to a smaller cross section. The calculation is performed with the `MSTW2008nnlo` PDF set.

86

- 6.14 Benchmark results for the total cross section $gg \rightarrow H + \text{jet}$ at leading order corrections in α_s , meaning with one real (radiative) correction to the Born-level cross section. The upper image shows the **HTurbo** output for the fixed-order only computation, which can be done by means of the quadrature integration or the Vegas algorithm, leading to a more precise predictions but with slower convergence. The lower image shows the **HNNLO** output, done by means of the quadrature integration. The phase space here has a cut in $q_T = 1$ GeV for the radiated parton, for a 125 GeV Higgs boson and in NWA approximation. The radiative correction is added to the Born-level cross section to produce the total result. In the **HNNLO** code, the result of the `accumulated integral` shows the contributions of the radiative corrections, to be compared with the `V+J` column of **HTurbo**, while the final result `Cross section` must be compared against the `total` column of **HTurbo**. Comparing with 6.13, a larger value of the q_T^{ext} leads to a smaller acceptance and hence to a smaller cross section. The calculation is performed with the `MSTW2008nnlo` PDF set. 87
- 6.15 Benchmark results for the total cross section $gg \rightarrow H + \text{jet}$ at next-to-leading order corrections in α_s , meaning with one real (radiative) correction and one virtual (loop) to the Born-level cross section. The upper image shows the **HTurbo** output for the fixed-order only computation, which can be done by means of the quadrature integration or the Vegas algorithm, leading to a more precise predictions but with slower convergence. The lower image shows the **HNNLO** output, done by means of the quadrature integration. The phase space here has a cut in $q_T = 5$ GeV for the radiated parton, for a 125 GeV Higgs boson and in NWA approximation. The virtual correction is added to the LO $H \rightarrow gg + \text{jet}$ cross section to produce the total result. In the **HNNLO** code, the result of the `accumulated integral` shows the contributions of the radiative corrections, to be compared with the `V+J` column of **HTurbo**, while the final result `Cross section` must be compared against the `total` column of **HTurbo**. The calculation is performed with the `MSTW2008nnlo` PDF set. 88
- 6.16 Comparison of the resummed predictions for the Higgs boson q_T distribution at NLL, NNLL and N³LL accuracy, using in all cases the `MSTW2008nnlo` PDF set. The upper image shows the computation with the Higgs boson fiducial phase space defined by the photon transverse momentum $q_T > 20$ GeV and the lepton pseudorapidity $|\eta| < 2.4$, and for the lower image it is totally inclusive. The Sudakov form factor is now computed including the $g^{(4)}$ function, by following [73] and [74]. The computation of the hard coefficients at N³LO is still to be implemented, while the calculation is already available at [107]. The smaller difference between the NNLL and N³LL curves suggest a good convergence of the perturbative expansion. 92

Bibliography

- [1] Michael E. Peskin and Daniel V. Schroeder. *An Introduction to quantum field theory*. Addison-Wesley, Reading, USA, 1995.
- [2] Chris Quigg. *Gauge Theories of the Strong, Weak, and Electromagnetic Interactions: Second Edition*. Princeton University Press, USA, 9 2013.
- [3] R. Keith Ellis, W. James Stirling, and B. R. Webber. *QCD and collider physics*, volume 8. Cambridge University Press, 2 2011.
- [4] Peter W. Higgs. Spontaneous symmetry breakdown without massless bosons. *Phys. Rev.*, 145:1156–1163, May 1966.
- [5] F. Englert and R. Brout. Broken symmetry and the mass of gauge vector mesons. *Phys. Rev. Lett.*, 13:321–323, Aug 1964.
- [6] G. S. Guralnik, C. R. Hagen, and T. W. B. Kibble. Global conservation laws and massless particles. *Phys. Rev. Lett.*, 13:585–587, Nov 1964.
- [7] G. Aad, T. Abajyan, B. Abbott, J. Abdallah, S. Abdel Khalek, A.A. Abdelalim, O. Abdinov, R. Aben, B. Abi, M. Abolins, and et al. Observation of a new particle in the search for the standard model higgs boson with the atlas detector at the lhc. *Physics Letters B*, 716(1):1–29, Sep 2012.
- [8] S. Chatrchyan, V. Khachatryan, A.M. Sirunyan, A. Tumasyan, W. Adam, E. Aguilo, T. Bergauer, M. Dragicevic, J. Erö, C. Fabjan, and et al. Observation of a new boson at a mass of 125 gev with the cms experiment at the lhc. *Physics Letters B*, 716(1):30–61, Sep 2012.
- [9] F. Halzen and Alan D. Martin. *QUARKS AND LEPTONS: AN INTRODUCTORY COURSE IN MODERN PARTICLE PHYSICS*. 1984.
- [10] Keith A. Brueckner. Meson-nucleon scattering and nucleon isobars. *Phys. Rev.*, 86:106–109, Apr 1952.
- [11] C. Chedester, P. Isaacs, A. Sachs, and J. Steinberger. Total cross sections of pimesons on protons and several other nuclei. *Phys. Rev.*, 82:958–959, 1951.
- [12] E. Fermi, H. L. Anderson, A. Lundby, D. E. Nagle, and G. B. Yodh. Ordinary and exchange scattering of negative pions by hydrogen. *Phys. Rev.*, 85:935–936, Mar 1952.
- [13] H. L. Anderson, E. Fermi, E. A. Long, and D. E. Nagle. Total Cross-sections of Positive Pions in Hydrogen. *Phys. Rev.*, 85:936, 1952.
- [14] Darragh E. Nagle. THE DELTA: THE FIRST PION NUCLEON RESONANCE, ITS DISCOVERY AND APPLICATIONS. 7 1984.
- [15] O. W. Greenberg. Spin and unitary-spin independence in a paraquark model of baryons and mesons. *Phys. Rev. Lett.*, 13:598–602, Nov 1964.

- [16] M. Y. Han and Y. Nambu. Three-triplet model with double SU(3) symmetry. *Phys. Rev.*, 139:B1006–B1010, Aug 1965.
- [17] Particle Data Group (PDG). Review of particle physics. *Phys. Rev. D*, 86:010001, Jul 2012.
- [18] Siegfried Bethke. World summary of α_s . *Nuclear Physics B - Proceedings Supplements*, 234:229–234, Jan 2013.
- [19] J. D. Bjorken and E. A. Paschos. Inelastic electron-proton and γ -proton scattering and the structure of the nucleon. *Phys. Rev.*, 185:1975–1982, Sep 1969.
- [20] Richard P. Feynman. Very high-energy collisions of hadrons. *Phys. Rev. Lett.*, 23:1415–1417, Dec 1969.
- [21] John C. Collins and Davison E. Soper. Parton Distribution and Decay Functions. *Nucl. Phys. B*, 194:445–492, 1982.
- [22] Yuri L. Dokshitzer. Calculation of the Structure Functions for Deep Inelastic Scattering and e^+e^- Annihilation by Perturbation Theory in Quantum Chromodynamics. *Sov. Phys. JETP*, 46:641–653, 1977.
- [23] V. N. Gribov and L. N. Lipatov. Deep inelastic $e p$ scattering in perturbation theory. *Sov. J. Nucl. Phys.*, 15:438–450, 1972.
- [24] G. Altarelli and G. Parisi. Asymptotic freedom in parton language. *Nuclear Physics B*, 126(2):298–318, 1977.
- [25] S. D. Drell and Tung-Mow Yan. Partons and their Applications at High-Energies. *Annals Phys.*, 66:578, 1971.
- [26] Tung-Mow Yan and Sidney D. Drell. The parton model and its applications. *International Journal of Modern Physics A*, 29(30):1430071, Dec 2014.
- [27] Amanda Cooper-Sarkar. What did hermes teach us about the structure of the proton? *Journal of Physics G: Nuclear and Particle Physics*, 39(9):093001, Jul 2012.
- [28] Sergey Alekhin, Kirill Melnikov, and Frank Petriello. Fixed target drell-yan data and nnlo qcd fits of parton distribution functions. *Physical Review D*, 74(5), Sep 2006.
- [29] E. G. de Oliveira, A. D. Martin, and M. G. Ryskin. Drell-Yan as a probe of small x partons at the LHC. *Eur. Phys. J. C*, 72:2069, 2012.
- [30] T. Kinoshita. Mass singularities of Feynman amplitudes. *J. Math. Phys.*, 3:650–677, 1962.
- [31] T. D. Lee and M. Nauenberg. Degenerate Systems and Mass Singularities. *Phys. Rev.*, 133:B1549–B1562, 1964.
- [32] S. Catani and M.H. Seymour. The dipole formalism for the calculation of qcd jet cross sections at next-to-leading order. *Physics Letters B*, 378(1-4):287–301, Jun 1996.
- [33] S. Catani and M.H. Seymour. A general algorithm for calculating jet cross sections in nlo qcd. *Nuclear Physics B*, 485(1-2):291–419, Feb 1997.
- [34] David A. Kosower. Antenna factorization of gauge-theory amplitudes. *Phys. Rev. D*, 57:5410–5416, May 1998.
- [35] David A. Kosower. Antenna factorization in strongly ordered limits. *Physical Review D*, 71(4), Feb 2005.
- [36] Stefano Catani and Massimiliano Grazzini. Next-to-next-to-leading-order subtraction formalism in hadron collisions and its application to higgs-boson production at the large hadron collider. *Physical Review Letters*, 98(22), May 2007.
- [37] GUDRUN HEINRICH. Sector decomposition. *International Journal of Modern Physics A*, 23(10):1457–1486, Apr 2008.
- [38] Dimitri V. Nanopoulos and Graham G. Ross. Asymptotic Freedom and the Callan-

- Gross Relation. *Phys. Lett. B*, 58:105–110, 1975.
- [39] Stephen L. Adler and Wu-Ki Tung. Bjorken limit in perturbation theory. *Phys. Rev. D*, 1:2846–2859, 1970. [Erratum: *Phys.Rev.D* 2, 2514–2514 (1970)].
- [40] R. Hamberg, W. L. van Neerven, and T. Matsuura. A complete calculation of the order $\alpha - s^2$ correction to the Drell-Yan K factor. *Nucl. Phys. B*, 359:343–405, 1991. [Erratum: *Nucl.Phys.B* 644, 403–404 (2002)].
- [41] Charalampos Anastasiou, Lance Dixon, Kirill Melnikov, and Frank Petriello. High-precision qcd at hadron colliders: Electroweak gauge boson rapidity distributions at next-to-next-to leading order. *Physical Review D*, 69(9), May 2004.
- [42] Stefano Catani, Giancarlo Ferrera, and Massimiliano Grazzini. W boson production at hadron colliders: the lepton charge asymmetry in nnlo qcd. *Journal of High Energy Physics*, 2010(5), May 2010.
- [43] G. Bozzi, S. Catani, D. de Florian, and M. Grazzini. The qt spectrum of the higgs boson at the lhc in qcd perturbation theory. *Physics Letters B*, 564(1-2):65–72, Jul 2003.
- [44] Abdelhak Djouadi. The anatomy of electroweak symmetry breaking tome i: The higgs boson in the standard model. *Physics Reports*, 457(1-4):1–216, Feb 2008.
- [45] M. et al Aaboud. Measurements of higgs boson properties in the diphoton decay channel with 36 fb^{-1} of pp collision data at $\sqrt{s} = 13 \text{ TeV}$ with the atlas detector.
- [46] Christopher J Glosser and Carl R Schmidt. Next-to-leading corrections to the higgs boson transverse momentum spectrum in gluon fusion. *Journal of High Energy Physics*, 2002(12):016–016, Dec 2002.
- [47] D. Graudenz, M. Spira, and P. M. Zerwas. Qcd corrections to higgs-boson production at proton-proton colliders. *Phys. Rev. Lett.*, 70:1372–1375, Mar 1993.
- [48] Giuseppe Bozzi, Stefano Catani, Daniel de Florian, and Massimiliano Grazzini. Transverse-momentum resummation and the spectrum of the higgs boson at the lhc. *Nuclear Physics B*, 737(1-2):73–120, Mar 2006.
- [49] Michael Krämer, Eric Laenen, and Michael Spira. Soft gluon radiation in higgs boson production at the lhc. *Nuclear Physics B*, 511(3):523–549, Feb 1998.
- [50] J.C. Collins, Davison E. Soper, and George Sterman. Transverse momentum distribution in drell-yan pair and w and z boson production. *Nuclear Physics B*, 250(1):199–224, 1985.
- [51] Ian Hinchliffe and S. F. Novaes. Transverse-momentum distribution of higgs bosons at the superconducting super collider. *Phys. Rev. D*, 38:3475–3480, Dec 1988.
- [52] Massimiliano Grazzini. The Transverse momentum distribution of the Higgs boson at the LHC. In *39th Rencontres de Moriond on QCD and High-Energy Hadronic Interactions*, pages 265–268, 6 2004.
- [53] D. de Florian, M. Grazzini, and Z. Kunszt. Higgs production with large transverse momentum in hadronic collisions at next-to-leading order. *Physical Review Letters*, 82(26):5209–5212, Jun 1999.
- [54] V. Ravindran, J. Smith, and W.L. van Neerven. Next-to-leading order qcd corrections to differential distributions of higgs boson production in hadron–hadron collisions. *Nuclear Physics B*, 634(1-2):247–290, Jul 2002.
- [55] V. Ravindran, J. Smith, and W.L. van Neerven. Nnlo corrections to the total cross section for higgs boson production in hadron–hadron collisions. *Nuclear Physics B*, 665:325–366, Aug 2003.
- [56] G. Parisi and R. Petronzio. Small Transverse Momentum Distributions in Hard Processes. *Nucl. Phys. B*, 154:427–440, 1979.

- [57] R.K. Ellis and Siniša Veseli. W and z transverse momentum distributions: resummation in q_t -space. *Nuclear Physics B*, 511(3):649–669, 1998.
- [58] Stefano Catani, Daniel de Florian, and Massimiliano Grazzini. Universality of non-leading logarithmic contributions in transverse-momentum distributions. *Nuclear Physics B*, 596(1-2):299–312, Feb 2001.
- [59] S. Catani, L. Trentadue, G. Turnock, and B.R. Webber. Resummation of large logarithms in ee event shape distributions. *Nuclear Physics B*, 407(1):3–42, 1993.
- [60] M. Dasgupta and G.P. Salam. Resummation of the jet broadening in dis . *The European Physical Journal C*, 24(2):213–236, Jun 2002.
- [61] Anna Kulesza, George F. Sterman, and Werner Vogelsang. Joint resummation in electroweak boson production. *Phys. Rev. D*, 66:014011, 2002.
- [62] John C. Collins, Davison E. Soper, and George F. Sterman. Transverse Momentum Distribution in Drell-Yan Pair and W and Z Boson Production. *Nucl. Phys. B*, 250:199–224, 1985.
- [63] Anna Kulesza, George Sterman, and Werner Vogelsang. Joint resummation for higgs boson production. *Phys. Rev. D*, 69:014012, Jan 2004.
- [64] Anna Kulesza and W. James Stirling. Non-perturbative effects and the resummed higgs transverse momentum distribution at the lhc . *Journal of High Energy Physics*, 2003(12):056–056, Dec 2003.
- [65] A. V. Lipatov and N. P. Zotov. Higgs boson production at hadron colliders in the kt -factorization approach. *The European Physical Journal C*, 44(4):559–566, Dec 2005.
- [66] C. Balazs and C. P. Yuan. Higgs boson production at the LHC with soft gluon effects. *Phys. Lett. B*, 478:192–198, 2000.
- [67] Stefano Catani, Daniel de Florian, Massimiliano Grazzini, and Paolo Nason. Soft-gluon resummation for higgs boson production at hadron colliders. *Journal of High Energy Physics*, 2003(07):028–028, Jul 2003.
- [68] John C. Collins and Davison E. Soper. Back-To-Back Jets in QCD. *Nucl. Phys. B*, 193:381, 1981. [Erratum: *Nucl.Phys.B* 213, 545 (1983)].
- [69] John C. Collins and Davison E. Soper. Back-to-back jets: Fourier transform from b to kt . *Nuclear Physics B*, 197(3):446–476, 1982.
- [70] John C. Collins, Davison E. Soper, and George Sterman. Factorization for short distance hadron-hadron scattering. *Nuclear Physics B*, 261:104–142, 1985.
- [71] V. Ravindran, J. Smith, and W.L. van Neerven. Nnlo corrections to the higgs production cross section. *Nuclear Physics B - Proceedings Supplements*, 135:35–40, 2004. Loops and Legs in Quantum Field Theory. Proceedings of the 7th DESY Workshop on Elementary Particle Theory.
- [72] K. G. Chetyrkin, B. A. Kniehl, and M. Steinhauser. Hadronic higgs boson decay to order α_s^4 . *Phys. Rev. Lett.*, 79:353–356, Jul 1997.
- [73] Ye Li and Hua Xing Zhu. Bootstrapping rapidity anomalous dimensions for transverse-momentum resummation. *Physical Review Letters*, 118(2), Jan 2017.
- [74] Andreas von Manteuffel, Erik Panzer, and Robert M. Schabinger. Cusp and collinear anomalous dimensions in four-loop qcd from form factors. *Physical Review Letters*, 124(16), Apr 2020.
- [75] Stefano Camarda, Maarten Boonekamp, Giuseppe Bozzi, Stefano Catani, Leandro Cieri, Jakub Cuth, Giancarlo Ferrera, Daniel de Florian, Alexandre Glazov, Massimiliano Grazzini, and et al. Dyturbo: fast predictions for drell-yan processes. *The European Physical Journal C*, 80(3), Mar 2020.
- [76] Daniel de Florian, Giancarlo Ferrera, Massimiliano Grazzini, and Damiano Tom-

- masini. Higgs boson production at the lhc: transverse momentum resummation effects in the $h \rightarrow \gamma\gamma, h \rightarrow ww \rightarrow \nu\nu$ and $h \rightarrow zz \rightarrow 4l$ decay modes. *Journal of High Energy Physics*, 2012(6), Jun 2012.
- [77] M.Grazzini. Higgs production at hadron colliders:tools <http://theory.fi.infn.it/grazzini/codes.html>.
- [78] LHC Machine. *JINST*, 3:S08001, 2008.
- [79] S. Dawson. Radiative corrections to Higgs boson production. *Nucl. Phys. B*, 359:283–300, 1991.
- [80] M. Spira, A. Djouadi, D. Graudenz, and R.M. Zerwas. Higgs boson production at the lhc. *Nuclear Physics B*, 453(1):17–82, 1995.
- [81] Robert V. Harlander and William B. Kilgore. Soft and virtual corrections to $p \rightarrow h + x$ at next-to-next-to-leading order. *Phys. Rev. D*, 64:013015, Jun 2001.
- [82] Leandro Cieri. Transverse-momentum resummation and the structure of hard factors at the NNLO. *PoS*, LL2014:062, 2014.
- [83] Alexei Prokudin, Peng Sun, and Feng Yuan. Scheme dependence and transverse momentum distribution interpretation of collins–soper–sterman resummation. *Physics Letters B*, 750:533–538, Nov 2015.
- [84] John Collins. *Foundations of perturbative QCD*, volume 32. Cambridge University Press, 11 2013.
- [85] John Collins and Ted Rogers. Understanding the large-distance behavior of transverse-momentum-dependent parton densities and the collins-soper evolution kernel. *Physical Review D*, 91(7), Apr 2015.
- [86] John M. Campbell and R.K. Ellis. Mcfm for the tevatron and the lhc. *Nuclear Physics B - Proceedings Supplements*, 205-206:10–15, Aug 2010.
- [87] T. Hahn. Concurrent cuba, 2014.
- [88] G Peter Lepage. A new algorithm for adaptive multidimensional integration. *Journal of Computational Physics*, 27(2):192–203, 1978.
- [89] Stefano Catani, Daniel de Florian, Giancarlo Ferrera, and Massimiliano Grazzini. Vector boson production at hadron colliders: transverse-momentum resummation and leptonic decay. *Journal of High Energy Physics*, 2015(12):1–47, Dec 2015.
- [90] Takuya Ooura and Masatake Mori. A robust double exponential formula for fourier-type integrals. *Journal of Computational and Applied Mathematics*, 112(1):229–241, 1999.
- [91] Takuya Ooura and Masatake Mori. The double exponential formula for oscillatory functions over the half infinite interval. *Journal of Computational and Applied Mathematics*, 38(1):353–360, 1991.
- [92] A. Vogt. Efficient evolution of unpolarized and polarized parton distributions with QCD-PEGASUS. *Comput. Phys. Commun.*, 170:65–92, 2005.
- [93] Roberto Bonciani, Stefano Catani, Massimiliano Grazzini, Hayk Sargsyan, and Alessandro Torre. The q_t subtraction method for top-quark production at hadron colliders. *The European Physical Journal C*, 75(12), Dec 2015.
- [94] M. Czakon. Double-real radiation in hadronic top quark pair production as a proof of a certain concept. *Nuclear Physics B*, 849(2):250–295, Aug 2011.
- [95] Radja Boughezal, Kirill Melnikov, and Frank Petriello. Subtraction scheme for next-to-next-to-leading order computations. *Physical Review D*, 85(3), Feb 2012.
- [96] James Currie, E. W. N. Glover, and Steven Wells. Infrared structure at nnlo using antenna subtraction. *Journal of High Energy Physics*, 2013(4), Apr 2013.
- [97] K.G. Chetyrkin, J.H. Kuhn, and A. Kwiatkowski. Qcd corrections to the e^+e^-

- cross-section and the z boson decay rate: concepts and results. *Physics Reports*, 277(4):189–281, Dec 1996.
- [98] J.A.M. Vermaseren, A. Vogt, and S. Moch. The third-order qcd corrections to deep-inelastic scattering by photon exchange. *Nuclear Physics B*, 724(1-2):3–182, Sep 2005.
- [99] Claude Duhr, Falko Dulat, and Bernhard Mistlberger. Drell-yan cross section to third order in the strong coupling constant. *Physical Review Letters*, 125(17), Oct 2020.
- [100] Xuan Chen, Thomas Gehrmann, Nigel Glover, Alexander Huss, Tong-Zhi Yang, and Hua Xing Zhu. Di-lepton rapidity distribution in drell-yan production to third order in qcd, 2021.
- [101] Stefano Camarda, Leandro Cieri, and Giancarlo Ferrera. Drell-yan lepton-pair production: q_t resummation at n^3 ll accuracy and fiducial cross sections at n^3 lo, 2021.
- [102] Charalampos Anastasiou, Claude Duhr, Falko Dulat, Franz Herzog, and Bernhard Mistlberger. Higgs boson gluon-fusion production in qcd at three loops. *Physical Review Letters*, 114(21), May 2015.
- [103] Bernhard Mistlberger. Higgs boson production at hadron colliders at n^3 lo in qcd. *Journal of High Energy Physics*, 2018(5), May 2018.
- [104] Frédéric A. Dreyer and Alexander Karlberg. Vector-boson fusion higgs production at three loops in qcd. *Physical Review Letters*, 117(7), Aug 2016.
- [105] Falko Dulat, Bernhard Mistlberger, and Andrea Pelloni. Differential higgs production at n^3 lo beyond threshold. *Journal of High Energy Physics*, 2018(1), Jan 2018.
- [106] Falko Dulat, Bernhard Mistlberger, and Andrea Pelloni. Precision predictions at n^3 lo for the higgs boson rapidity distribution at the lhc. *Physical Review D*, 99(3), Feb 2019.
- [107] Leandro Cieri, Xuan Chen, Thomas Gehrmann, E. W. N. Glover, and Alexander Huss. Higgs boson production at the lhc using the q_T subtraction formalism at n^3 lo qcd. *Journal of High Energy Physics*, 2019(2), Feb 2019.
- [108] G. P. Korchemsky and A. V. Radyushkin. Loop Space Formalism and Renormalization Group for the Infrared Asymptotics of QCD. *Phys. Lett. B*, 171:459–467, 1986.
- [109] Thomas Becher and Matthew D Schwartz. A precise determination of α_s from lep thrust data using effective field theory. *Journal of High Energy Physics*, 2008(07):034–034, Jul 2008.
- [110] Riccardo Abbate, Michael Fickinger, André H. Hoang, Vicent Mateu, and Iain W. Stewart. Thrust at n^3 ll with power corrections and a precision global fit for $\alpha_s(m_Z)$. *Physical Review D*, 83(7), Apr 2011.
- [111] S. Moch, J.A.M. Vermaseren, and A. Vogt. The three-loop splitting functions in qcd: the non-singlet case. *Nuclear Physics B*, 688(1-2):101–134, Jun 2004.
- [112] A. Vogt, S. Moch, and J.A.M. Vermaseren. The three-loop splitting functions in qcd: the singlet case. *Nuclear Physics B*, 691(1-2):129–181, Jul 2004.
- [113] S. Moch, B. Ruijl, T. Ueda, J. A. M. Vermaseren, and A. Vogt. Four-loop non-singlet splitting functions in the planar limit and beyond. *Journal of High Energy Physics*, 2017(10), Oct 2017.
- [114] S. Moch, B. Ruijl, T. Ueda, J.A.M. Vermaseren, and A. Vogt. On quartic colour factors in splitting functions and the gluon cusp anomalous dimension. *Physics Letters B*, 782:627–632, Jul 2018.
- [115] Andrey G. Grozin, Johannes M. Henn, Gregory P. Korchemsky, and Peter Mar-

- quard. The three-loop cusp anomalous dimension in qcd and its supersymmetric extensions. *Journal of High Energy Physics*, 2016(1), Jan 2016.
- [116] Johannes M. Henn, Alexander V. Smirnov, Vladimir A. Smirnov, and Matthias Steinhauser. A planar four-loop form factor and cusp anomalous dimension in qcd, 2016.
- [117] Andreas von Manteuffel and Robert M. Schabinger. Quark and gluon form factors to four-loop order in qcd: The n_f^3 contributions. *Physical Review D*, 95(3), Feb 2017.
- [118] Andrey Grozin. Four-loop cusp anomalous dimension in qed. *Journal of High Energy Physics*, 2018(6), Jun 2018.
- [119] Andreas von Manteuffel and Robert M. Schabinger. Quark and gluon form factors in four loop qcd: The n_f^2 and $n_{q\gamma}n_f$ contributions. *Physical Review D*, 99(9), May 2019.
- [120] F. Herzog, B. Ruijl, T. Ueda, J. A. M. Vermaseren, and A. Vogt. The five-loop beta function of yang-mills theory with fermions. *Journal of High Energy Physics*, 2017(2), Feb 2017.
- [121] Thomas Luthe, Andreas Maier, Peter Marquard, and York Schröder. The five-loop beta function for a general gauge group and anomalous dimensions beyond feynman gauge. *Journal of High Energy Physics*, 2017(10), Oct 2017.
- [122] K. G. Chetyrkin, G. Falcioni, F. Herzog, and J.A.M. Vermaseren. Five-loop renormalisation of qcd in covariant gauges. *Journal of High Energy Physics*, 2017(10), Oct 2017.
- [123] Thomas Becher and Matthias Neubert. Infrared singularities of scattering amplitudes in perturbative qcd. *Physical Review Letters*, 102(16), Apr 2009.
- [124] Einan Gardi and Lorenzo Magnea. Factorization constraints for soft anomalous dimensions in qcd scattering amplitudes. *Journal of High Energy Physics*, 2009(03):079–079, Mar 2009.
- [125] Thomas Becher and Matthias Neubert. On the structure of infrared singularities of gauge-theory amplitudes. *Journal of High Energy Physics*, 2009(06):081–081, Jun 2009.
- [126] Lance J. Dixon. Matter dependence of the three-loop soft-anomalous-dimension matrix. *Physical Review D*, 79(9), May 2009.
- [127] Stefano Catani, Daniel de Florian, and Massimiliano Grazzini. Soft-gluon effective coupling and cusp anomalous dimension. *The European Physical Journal C*, 79(8), Aug 2019.
- [128] Thomas Becher and Matthias Neubert. Infrared singularities of scattering amplitudes and n^3 resummation for n -jet processes. *Journal of High Energy Physics*, 2020(1), Jan 2020.
- [129] Johannes M. Henn, Gregory P. Korchemsky, and Bernhard Mistlberger. The full four-loop cusp anomalous dimension in $\mathcal{N} = 4$ super yang-mills and qcd, 2019.
- [130] J. Davies, A. Vogt, B. Ruijl, T. Ueda, and J.A.M. Vermaseren. Large- n_f contributions to the four-loop splitting functions in qcd. *Nuclear Physics B*, 915:335–362, Feb 2017.
- [131] Christian W. Bauer, Sean Fleming, and Michael Luke. Summing sudakov logarithms in $b \rightarrow x_s + \gamma$ in effective field theory. *Physical Review D*, 63(1), Dec 2000.
- [132] Christian W. Bauer, Sean Fleming, Dan Pirjol, and Iain W. Stewart. An effective field theory for collinear and soft gluons. *Physical Review D*, 63(11), May 2001.
- [133] Miguel G. Echevarría, Ahmad Idilbi, Andreas Schäfer, and Ignazio Scimemi. Model independent evolution of transverse momentum dependent distribution functions (tmds) at nll. *The European Physical Journal C*, 73(12), Nov 2013.

- [134] Christian W. Bauer, Sean Fleming, Dan Pirjol, Ira Z. Rothstein, and Iain W. Stewart. Hard scattering factorization from effective field theory. *Physical Review D*, 66(1), Jul 2002.
- [135] M. Beneke, A.P. Chapovsky, M. Diehl, and Th. Feldmann. Soft-collinear effective theory and heavy-to-light currents beyond leading power. *Nuclear Physics B*, 643(1-3):431–476, Nov 2002.
- [136] Yang Gao, Chong Sheng Li, and Jian Jun Liu. Transverse momentum resummation in soft collinear effective theory. *Physical Review D*, 72(11), Dec 2005.
- [137] Ahmad Idilbi, Xiangdong Ji, and Feng Yuan. Transverse momentum distribution through soft-gluon resummation in effective field theory. *Physics Letters B*, 625(3-4):253–263, Oct 2005.
- [138] Sonny Mantry and Frank Petriello. Factorization and resummation of higgs boson differential distributions in soft-collinear effective theory. *Physical Review D*, 81(9), May 2010.
- [139] Jui-yu Chiu, Ambar Jain, Duff Neill, and Ira Z. Rothstein. Rapidity renormalization group. *Physical Review Letters*, 108(15), Apr 2012.
- [140] Jui-Yu Chiu, Ambar Jain, Duff Neill, and Ira Z. Rothstein. A formalism for the systematic treatment of rapidity logarithms in quantum field theory. *Journal of High Energy Physics*, 2012(5), May 2012.
- [141] Miguel G. Echevarría, Ahmad Idilbi, and Ignazio Scimemi. Factorization theorem for drell-yan at low q_T and transverse-momentum distributions on-the-light-cone. *Journal of High Energy Physics*, 2012(7), Jul 2012.
- [142] Thomas Becher and Matthias Neubert. Drell-yan production at small q_T , transverse parton distributions and the collinear anomaly. *The European Physical Journal C*, 71(6), Jun 2011.
- [143] Xuan Chen, Thomas Gehrmann, E.W. Nigel Glover, Alexander Huss, Ye Li, Duff Neill, Markus Schulze, Iain W. Stewart, and Hua Xing Zhu. Precise qcd description of the higgs boson transverse momentum spectrum. *Physics Letters B*, 788:425–430, 2019.
- [144] P. A. Baikov, K. G. Chetyrkin, A. V. Smirnov, V. A. Smirnov, and M. Steinhauser. Quark and gluon form factors to three loops. *Physical Review Letters*, 102(21), May 2009.
- [145] R. N. Lee, A. V. Smirnov, and V. A. Smirnov. Analytic results for massless three-loop form factors. *Journal of High Energy Physics*, 2010(4), Apr 2010.
- [146] T. Gehrmann, E. W. N. Glover, T. Huber, N. Ikizlerli, and C. Studerus. Calculation of the quark and gluon form factors to three loops in qcd. *Journal of High Energy Physics*, 2010(6), Jun 2010.
- [147] K Chetyrkin. Decoupling relations to $\mathcal{O}(\alpha_s^3)$ and their connection to low-energy theorems. *Nuclear Physics B*, 510(1-2):61–87, Jan 1998.
- [148] Stefano Catani, Leandro Cieri, Daniel de Florian, Giancarlo Ferrera, and Massimiliano Grazzini. Vector-boson production at hadron colliders: hard-collinear coefficients at the nnlo. *The European Physical Journal C*, 72(11), Nov 2012.
- [149] Stefano Catani and Massimiliano Grazzini. Higgs boson production at hadron colliders: hard-collinear coefficients at the nnlo. *The European Physical Journal C*, 72(5), May 2012.
- [150] Jesús Urtasun-Elizari et al. PHOTON 2019, TIF-UNIMI-2019-16. Towards hardware acceleration for parton densities estimation, 2019.

Acknowledgments

Here I find myself, at the end of my Ph.D. After almost four long years of work, a position from which, suddenly, everything seems so distant. I will use these lines as a last opportunity to informally acknowledge on a formal document all the people around me, who helped me somehow in preparing this work and shared this path in many different ways. It is also the unique part of this thesis where I will use the Spanish language, first not to introduce more grammatical errors, and also to closely address the ones who had followed me from the distance.

I would like to thank first my supervisors, without whom this thesis would not exist at all. I am really grateful to Prof. Stefano Forte and Stefano Carrazza, who gave me the opportunity to endure the academic path in theoretical physics within the N3PDF group and the NNPDF collaboration. What I have learned from them, not only about the specific fields my thesis was headed to, but also about pure research, and how to properly address and describe the fundamental laws of nature, already in my first steps as a professional scientist, became really valuable. Second, and from a more personal side, I would like to thank Prof. Giancarlo Ferrera, who helped me drive this thesis to its end and build what it is written in this manuscript. From you I have learned to think and work in the patient, reflexive and critical way that I know I will still apply in my further steps as a scientist. Also your company, advice and guidance have been close and warm, the kind of human contact one struggles sometimes to find within the academic path.

Thanks Tanjona, Juan and Christopher, for your help and company from the first day I arrived to Milan, and also the ones that arrived later. Thank you also Felix, Alessandro and Roy, as my fellow colleges of the N3PDF group. Even if it was most of the time remote communication via zoom, it has been an absolute pleasure to share these years with you, and I really wish you all the best of luck in your academic and personal paths. Also to Bennedetta and Martina, both as the Ph.D council representatives and good friends. I thank you both from a more personal side, since your help and guidance in the difficult moments of this thesis, where I actually thought I would not complete it at all, was extremely valuable. The kind of help and commitment you provided was not only extremely useful, but also something that I will remember and for which I am today extremely grateful.

I finally have some formal thanks. I thank the NNPDF collaboration, the GGI institute, the CTEQ collaboration and the CERN & Fermilab theory division. Being able to participate in the conferences and education programs you hosted has been extremely

instructive, together with a beautiful personal experience. I also thank the IFAE of Barcelona for inviting me the first year of my Ph.D to expose and discuss the first ideas of my thesis, and in particular to Prof. Rafel Escribano. Without the advice and references you constantly provided I would not have made it so far. And after many years, as I have always done when reaching new steps in my academic path, I thank Prof. Javier Tejada, professor of quantum mechanics and tutor of my bachelor degree final project, back at the University of Barcelona. Your guidance and support, even after these many years, are something I will always remember with a smile.

Y por último, ya en mi idioma, me dirijo a la gente que a pesar de estar en la distancia me ha ofrecido, muchas veces sin saberlo, un apoyo, compañía, incluso guía y consejo, que van mucho más allá de lo meramente académico. Podría estar horas divagando sobre la amistad, la juventud, la calidez de las buenas compañías y el transcurso de los años, y sobre cómo he aprendido a valorar las relaciones que se mantienen a pesar de los vaivenes del tiempo. A mis más viejos amigos, que desde las calles de Pamplona han alegrado mis navidades y mis veranos, brindándome siempre la oportunidad de volver a un lugar donde descansar y al que puedo llamar mi hogar. A los que empiezan a ser viejos amigos también, pasando por la calle Portbou, la Neu de Sant Cugat, el 120 de la calle Rosselló y tantos otros rincones de Barcelona, habéis hecho este camino mucho más fácil, y aún tengo pendiente recordaros en persona lo agradecido que estoy por vuestra amistad. Han sido unos años enormemente complejos y me encuentro algo sensible, tanto que casi me va a salir alguna lágrima escribiendo estas líneas. Gracias de verdad, Neus, por compartir este camino conmigo. Has llenado de color este capítulo de mi vida, no exento de etapas muy grises, y espero que sigas llenando los que están por venir.

Y para concluir, gracias a mis padres, sin los cuales ni esta tesis ni nada de lo que hoy tengo sería posible. Una vez más, los años me dan una perspectiva de aquello que es realmente importante, y me faltan palabras para expresar la gratitud que siento por la educación, disciplina, calidez y comprensión que siempre me habéis brindado. Desde mis primeros recuerdos habéis estado a mi lado siendo la clase de apoyo y referencia que nunca pedí y que ahora empiezo a valorar de verdad. Habéis trabajado tanto, seguramente muchas veces sin saberlo siquiera, para que hoy yo pueda disfrutar de la sana y feliz juventud de que disfruto, y con un horizonte lleno de posibilidades impredecibles, que no puedo más que agradecer cada minuto de vuestro tiempo. Por eso esta tesis está dedicada a vuestros.

Las últimas palabras, como no podía ser de otra forma, son para mi hermano, Dr. Josemari Urtasun, que has compartido todas y cada una de mis alegrías, penas y lamentos durante estos años. La más valiosa de las compañías que tengo, cuyo empuje, sencillez y determinación en todos los aspectos de la vida son la primera y última de las cosas me llevo.

Esta tesis es para todos vosotros.

Gracias de verdad,

Jesús,

London, November 2021